12-2013

Optimization of Scintillator based Radiation Portal Monitors

Matthew J. Urffer
University of Tennessee - Knoxville, murffer@utk.edu

To the Graduate Council:

I am submitting herewith a dissertation written by Matthew J. Urffer entitled "Optimization of Scintillator based Radiation Portal Monitors." I have examined the final electronic copy of this dissertation for form and content and recommend that it be accepted in partial fulfillment of the requirements for the degree of Doctor of Philosophy, with a major in Nuclear Engineering.

Laurence F. Miller, Major Professor

We have read this dissertation and recommend its acceptance:

Lawrence H. Heilbronn, Dayaker Penumadu, Ronald E. Pevey

Accepted for the Council:

Carolyn R. Hodges

Vice Provost and Dean of the Graduate School

(Original signatures are on file with official student records.)

12-2013

Optimization of Scintillator based Radiation Portal Monitors

Matthew John Urffer
murffer@utk.edu

To the Graduate Council:

I am submitting herewith a dissertation written by Matthew John Urffer entitled "Optimization of Scintillator based Radiation Portal Monitors." I have examined the final electronic copy of this dissertation for form and content and recommend that it be accepted in partial fulfillment of the requirements for the degree of Doctor of Philosophy, with a major in .

Laurence F. Miller, Major Professor

We have read this dissertation and recommend its acceptance:

Lawrence H. Heilbronn, Dayaker Penumadu, Ronald E. Pevey

Accepted for the Council:
Carolyn R. Hodges

Vice Provost and Dean of the Graduate School

(Original signatures are on file with official student records.)

Optimization of Scintillator based Radiation Portal Monitors

A Dissertation Presented for the

Doctor of Philosophy

Degree

The University of Tennessee, Knoxville

Matthew J. Urffer

December 2013

To my family and friends

Acknowledgments

This work would not have been possible without the support of various resources. Dr. Miller has been an essential resource for bouncing ideas around while providing valuable insights and encouragement for this work. I would also like to thank my committee members, Dr. Heilbronn, Dr. Penumadu, and Dr. Pevey, for their support and technical expertise that they have provided. The testing of films would not have been possible without the kind folks fabricating the materials, I would like to acknowledge the work of Dr. Mabe, Dr. Auxier II, and Dr. Uppal for their help and numerous conversations.

The academic portion of this would have never succeeded without the support from my friends and family. My mother and father, Lisa and Micheal, deserve special recognition of their support, encouragement and frank advice. Katie, Samuel, David, Isaac, Esther and Eli also deserve recognition for being spectacularly supportive siblings. Finally, I would like to thank the members of Knoxville Ultimate for being supportive and offering many great games.

Financial support from the Domestic Nuclear Detection Office (DNDO) through Award No. 003387891 is gratefully acknowledged. Any opinions, findings, and conclusions or recommendations expressed in this material are those of the presenter and do not necessarily reflect the views of DNDO.

Abstract

Alternative neutron detection technologies are needed to replace the current He-3 based Radiation Portal Monitors (RPM) which are employed to detect special nuclear material that may be entering the United States illicitly. Replacement technologies must fulfill the following criteria established by the Department of Homeland Security (DHS): 1) a neutron detection efficiency, 2) a gamma insensitivity, and 3) the performance of the detector should not suffer in the presence of a strong gamma field. Polymeric films containing Li-6 ranging from 15 to 300 microns have the ability to fulfill these criteria if suitably utilized. For a typical detector material the design involves maximizing the neutron-gamma discrimination, maximizing the physical detector configuration in order to ensure optimal use of the incident neutron spectra, and ensuring that the scintillation light generated can be collected.

A technique for using a pulse height discriminator for rejecting gamma interactions has been developed for polymeric films, and it was determined that films ranging from 15 microns to 300 microns thick will satisfy the DHS criteria. The basis of this technique is attributed to the relative ranges of the secondary electrons of the Compton scattered electrons from the gamma interactions, compared to the ranges of the electrons from the reaction products of a neutron absorption. Detailed Monte Carlo simulations indicate that a desired film thickness is from 50 to 150 microns.

A replacement portal monitor has been designed for layered polymeric films that effectively utilizes enriched Li-6 in the detector material using a genetic algorithm to optimize the spacing between the layers, while cylindrical designs could also be

employed. If two photomultiplier tubes are placed on two fishtail light guides mounted on the top and bottom of the detector cabinet, eight percent of the optical photons generated in a ten percent loaded polystyrene film can be collected, which would be sufficient to create a voltage signal.

Executive Summary

The shortage of ^{3}He has caused the Domestic Nuclear Detection Office (DNDO) within the U.S. Department of Homeland Security (DHS) to sponsor research for alternative radiation portal monitors (RPM). The DNDO/DHS in conjunction with Pacific Northwest National Lab (PNNL) have established performance criteria that replacement technologies must satisfy. Replacement technologies must fulfill three basic criteria: 1) a neutron detection efficiency, 2) a gamma insensitivity, and 3) the performance of the detector should not suffer in the presence of a strong gamma field. Polymeric films containing ^{6}Li ranging from 15 to 300 microns have the ability to fulfill these criteria if suitably utilized. For a typical detector this involves maximizing the neutron-gamma discrimination, maximizing the physical detector configuration in order to ensure optimal use of the incident neutron spectra, and ensuring that the scintillation light generated can be collected.

A pulse height discriminator technique for rejecting gamma interactions has been developed for polymeric films ranging from 15 µm to 300 µm thick. The feasibility of using a pulse height discriminator has been investigated and attributed to the energy deposition in the material by the reaction products of the gammas and neutrons, where the Compton scattered electrons from a photon interaction generally have energies in the hundreds of keV while the ^{6}Li reaction products have energies in the 10 keV range. Detailed GEANT4 simulations indicate that films from 50 µm to 150 µm would be a practical.

A replacement portal monitor has then been designed for layered polymeric films that effectively utilize the ^{6}Li in the detector material. These layered detector designs consist of thin film layers sandwiched between wavelength shifting light guides. A genetic algorithm was employed to optimize the interaction rate above the necessary discriminator level for three different types of detector materials. Two of these materials were composite polymers developed at the University of Tennessee, consisting of a polystyrene based film and a polyethylene naphthalene film. The third material was a commercial scintillator, ^{6}LiF loaded ZnS:Ag (EJ-426HD). An example of the an optimized geometry is shown in Figure 1 in which the films are 100 µm thick placed in a wavelength shifter.

The positions of the films necessary to meet the detector criteria are shown in Table 1. These layered detector designs consist of 100 µm, ^{6}Li fluoride loaded polymers that are encased in 5 mm of a wavelength shifting plastic in addition to a 100 µm ^{6}LiF loaded ZnS:Ag commercial scintillator also encased in a wavelength shifter. The wavelength shifter was assumed to have a material composition similar to that of high density polyethylene, which also served as the moderator. In the case of the polyethylene naphthalene film pulse shape discrimination shows promise as an alternative method of neutron - gamma discrimination in which the entire neutron spectra can be utilized. In this case only two 100 µm, 10% ^{6}LiF loaded detector films spaced at 2.54 cm and 5.08 cm would be sufficient. In addition to layered designs a design in which the ^{6}Li detector layers are wrapped around into concentric cylinders was also explored. A design using four cylinders (each 2 cm in outer diameter) placed equidistant in the RPM8 loaded with 30% ^{6}Li fluoride (using 28 g of ^{6}Li) would have an interaction rate above 3.2 interactions per second per nanogram ^{252}Cf. If two 2 in photomultiplier tubes are placed at the top and bottom of a fishtail light guide mounted on the top and bottom of the detector cabinet, 8% of the optical photons generated in a 10% loaded polystyrene film can be collected. It is assumed for the estimated 5 in PMT photons collected that the light collection efficiency of 5 in

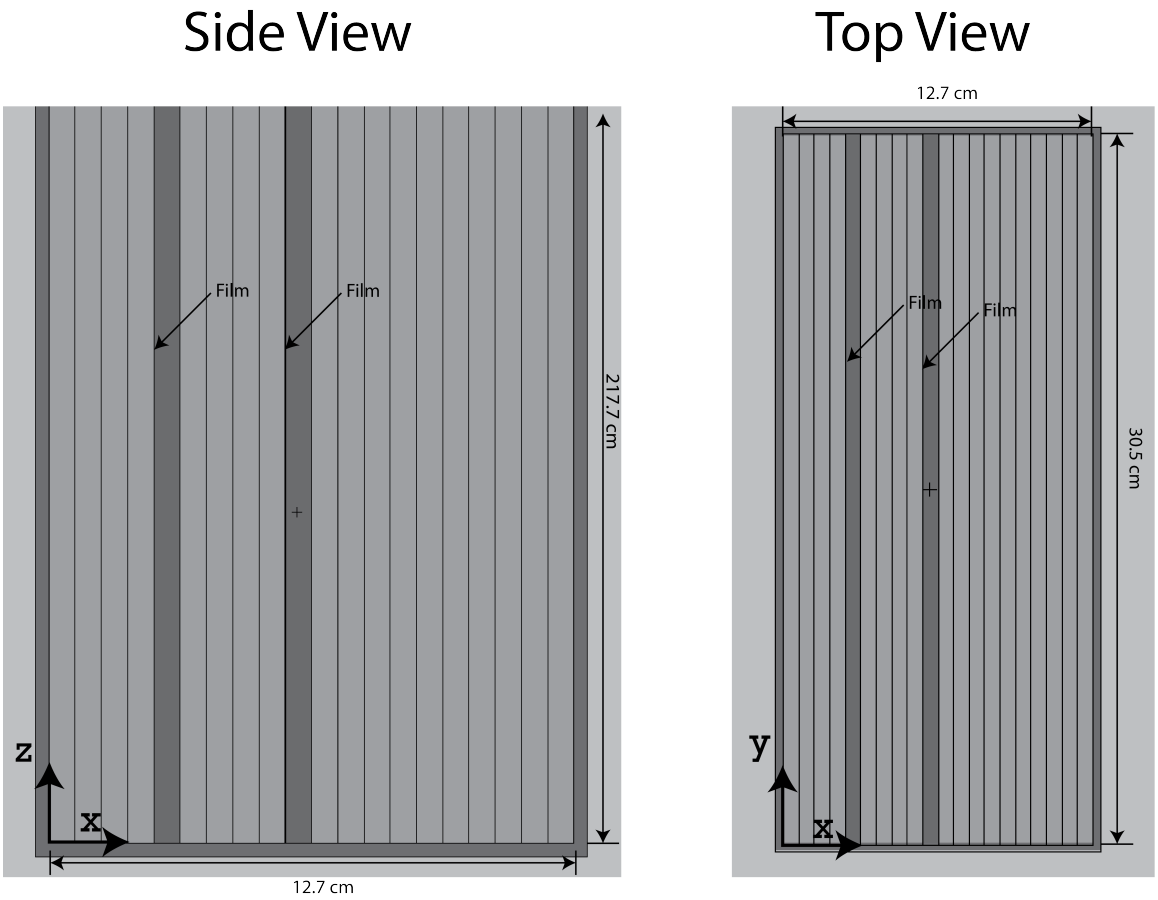

Figure 1: Example geometry of a film inside the radiation portal monitor. The film material is ^{6}LiF loaded ZnS:Ag, which has a high loading of ^{6}Li. The origin is shown in the lower left of each figure, along with the axis.

Table 1: Simulated detector performance in a design capable of meeting the DHS / DNDO criteria.

Detector Composition	Film Positions	Estimated Photons Collected	
		2 in PMT	5 in PMT
10% ^{6}LiF polystyrene	2.54 cm, 3.82 cm, 6.36 cm	160	432
10% ^{6}LiF polyethylene naphthalene	1.90 cm, 3.82 cm, 5.08 cm	240	410
^{6}LiF loaded ZnS:Ag	3.17 cm, 6.35 cm	1,900	5,130

PMT can be estimated from the ratio of the 2 in PMT to 5 in PMT light collection efficiency[Jordan et al., 2003].

Improvements to this design may be found by exploiting the larger fraction of the neutron count rate above the pulse height discriminator for thinner films (at the cost of reduced light output). Future work should be directed into exploring the light collection efficiency for different film thickness and the dependance on the number of films necessary to meet the DHS criteria in planar and cylindrical arrangements.

Table of Contents

List of Tables

List of Figures

List of Notations

ϵ_{int}	intrinsic efficiency	125
$\forall$	Volume of the cell	106
$\frac{dE}{dx}$	linear stopping power	23
Ω	fraction of solid angle detector subtends	125
Φ	i	35
$\phi(E)$	Energy dependent fluence	105
$\Re_m(E)$	Response function operator	105
θ_c	critical angle	30
$\vec{\Omega}$	direction	126
$\vec{J}$	particle current	126
$\vec{r}$	position	126
E	energy	126
I	Interaction rate	105
kB	Birks parameter	23
n_0	index of refraction of the scintillator	30

Chapter 1

Introduction

Radiation Portal Monitors (RPMs) are passive radiation detection systems implemented at over a thousand of border crossings. RPMs are designed to determine if cargo contains any special nuclear material in a safe, nondestructive, and effective manner[Kouzes et al., 2010]. However, the current technology used in RPMs for detecting neutrons emitted from special nuclear material use a rapidly diminishing resource, ^{3}He, that cannot be economically replaced. The Department of Homeland Security (DHS) continues to fund research (through the Domestic Nuclear Detection Office (DNDO)) for the development of detector systems to detect radioactive material that could potentially be used to cause significant economic loss and loss of life. As a result of this research a number of alternative detection systems continue to be investigated with the most viable including: boron trifluoride filled proportional detectors, boron-lined proportional detectors, ^{6}Li loaded scintillation glass fiber detectors, and ^{6}Li plus scintillator-coated wavelength-shifting fiber detectors[Van Ginhoven et al., 1999, Kouzes et al., 2010].

Neutron detectors often utilize a material with a large thermal cross section for absorption, such as ^{6}Li (940 b) or ^{10}B (3.800 b). When these materials absorb a neutron, they usually disintegrate to produce ionized reaction products that in turn transfer their kinetic energy to electrons. In the case of the $^{6}\mathrm{Li}\,(n, {}^{3}\mathrm{H})\,\alpha$ reaction,

the fission energy is distributed between a triton of energy 2.73 MeV and an alpha of energy 2.05 MeV. In a proportional counter such as the ^{3}He based detectors,the energy from the charged particles would ionize a gas, creating a voltage signal. Scintillator detectors, on which this work is based, utilize the charged particle energy depositions to create electron excitations in the scintillating material which are then transferred by fluors and produce visible light, which is detected with a photomultiplier tube.

1.1 Replacement Detector Criteria

Pacific Northwest National Lab (PNNL) and DNDO have developed a set of specifications that replacement RPMs must meet [Kouzes et al., 2010, RT et al., 1999]. In particular 1) an absolute neutron detection efficiency greater than 2.5 count/s/ng^{252}Cf at 2 m for a defined moderated source, 2) an intrinsic gamma-neutron detection efficiency of one in a million, and 3) a gamma absolute rejection ratio for neutrons stating that the performance of the detector should not change by more than 10% in a 10 mR h^{-1} gamma field. These parameters are summarized in Table 1.1.

The absolute neutron detection efficiency ($\epsilon_{abs,n}$) is defined as the number of neutron pulses recorded by the detector normalized by the number of neutrons emitted by the source as shown in Equation 1.1

$$\epsilon_{abs,n} = \frac{N_{nc}}{N_{ns}} \tag{1.1}$$

Table 1.1: Replacement Portal Monitor Criteria

Parameter	Specification
Absolute neutron detection efficiency	2.5 cps/ng of ^{252}Cf (in specified test configuration)
Intrinsic gamma-neutron detection efficiency	$\epsilon_{int,\gamma n} \leq 10^{-6}$
Gamma absolute rejection ratio for neutrons (GARRn)	$0.9 \leq$ GARRn ≤ 1.1 at 10 mR/h exposure
Cost	\$ 30,000 per system

where N_{nc} is the neutron count rate and N_{ns} is the neutron emission rate from the source. DNDO guidelines state that a ^{252}Cf source placed 2 m from the midpoint of the detector is to be used for the determination of the absolute neutron detection efficiency[Van Ginhoven et al., 1999]. To reduce the gamma ray flux of ^{252}Cf upon a candidate detector the source is shielded by at least 0.5 cm of lead, and the neutron spectrum is then moderated by 2.5 cm of polyethylene[Van Ginhoven et al., 1999]. The intrinsic efficiency, which provides a measure of how sensitive the detector is to incoming radiation, is defined in (1.2).

$$\epsilon_{int} = \frac{\text{Number Counts Observed}}{\text{Number Quanta for Radiation Crossing Detector}} \tag{1.2}$$

The formulation presented in (1.2) is then adapted to photons, with the requirement that only one count per a million photons passing through the detector may be registered. To account for this the subscript γn is added to the intrinsic efficiency (1.3)

$$\epsilon_{int,\gamma n} = \frac{P_{pc}}{P_{p\Phi}} \tag{1.3}$$

where P_{pc} is the photon count rate and $P_{p\Phi}$ is the photons crossing the detector. The intrinsic gamma-neutron detection efficiency is to be measured using either a ^{192}Ir, ^{137}Cs, or ^{60}Co source placed at an appropriate distance so as to produce an exposure rate of 10 mR h^{-1} at the detector[RT et al., 1999]. The final detector parameter, the gamma absolute rejection ratio (GARRn), characterizes the detector response in the presence of both a large gamma ray source (10 mR h^{-1}) and a ^{252}Cf neutron source (configured as it would be for an absolute neutron detection efficiency measurement). This criteria, shown in (1.4), implies that the performance of the detector should not change by more than 10% in a strong gamma field[RT et al., 1999].

$$GARRn = \frac{\epsilon_{abs,\gamma n}}{\epsilon_{abs,n}} \tag{1.4}$$

1.2 Current Technologies

Currently, several alternative technologies are being developed, but two of the most promising detector technologies are boron loaded straw fibers being developed by Proportional Technologies Inc. (Houston, TX) and LiF loaded ZnS(Ag) scintillator paddles being developed by Innovative American Technology (Coconut Creek, FL). The boron straw tubes meet the count rate criteria with a gamma rejection rate estimated at 4×10^{-9} while passing the GARRn [Kouzes et al., 2012]. LiF/ZnS(Ag) is a commercial inorganic scintillator that utilizes the alpha from the ^{6}Li neutron capture to activate the ZnS doped with silver (ZnS(Ag)). LiF/ZnS(Ag) has a high light output per neutron (1.6×10^{5} photons per neutron) with a decay time of approximately 100 µs and the maximum emission at 450 nm [Carel W.E, 2001]. However, this material is opaque and therefore care needs to be taken with the light collection of a large area detector. Innovative American Technology (IAT) has developed a design of a replacement RPM that utilizes LiF/ZnS(Ag), as shown schematically in Figure 1.1 and in Figure 1.2. Current testing indicates that this detector design will meet the DHS criteria[Kouzes and Ely, 2010].

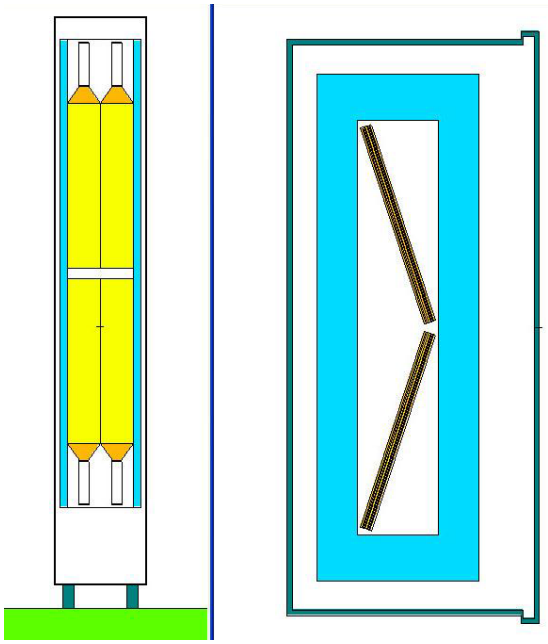

Figure 1.1: Modeled IAT detector that consist of four paddles. The paddles are angled to expose a larger surface to the neutron flux[Ely et al., 2013].

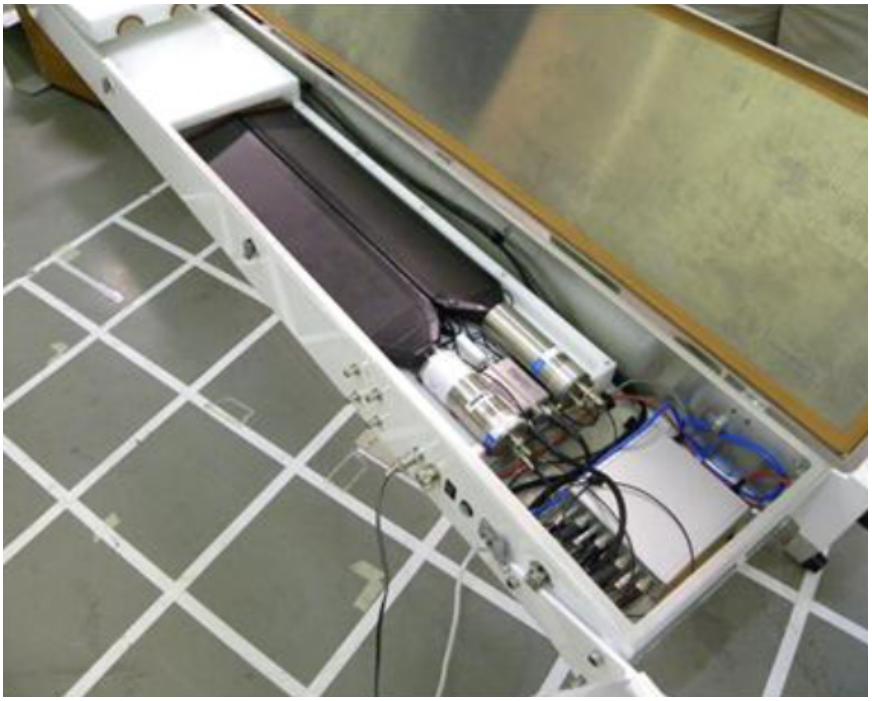

Figure 1.2: Photograph of the developed IAT detector[Ely et al., 2013].

1.3 Thin Film Scintillators

In addition to the inorganic scintillator LiF/ZnS(Ag), work is being completed at the University of Tennessee to construct thin film polymeric scintillators to be utilized in a layered detector design for replacement RPMs. These films, either based on polystyrene (PS) or polyethylene naphthalene (PEN), are ^{6}LiF containing polymers projected to be low cost, have high mechanical durability, and meet the detector criteria [Sen et al., 2012, Mabe et al., 2013]. These new materials have been characterized for their neutron performance and gamma discrimination abilities, a summary of which (as of May 2013) may be found in Appendix E.

1.4 Optimization Opportunities

There exists a need to build predictive modeling capabilities of these detectors in order to optimize the detector performance. For a particular material and neutron absorber the detector geometry can be optimized to maximize the energy deposited in scintillation material by charged particles relative to the energy deposited by photon interactions. This in turn permits one to maximize the recorded neutron interaction rate relative to recorded photon interaction rates by setting a lower level discriminator (LLD) above a threshold associated with energy deposited in the detector by photons. As the LLD is increased, the efficiency for detecting neutrons is diminished; however, the intrinsic efficiency for detecting neutrons relative to photons is dramatically increased. In addition, as the neutron flux is being moderated and absorbed by the RPM material there exist the opportunity to position the neutron absorber films to maximize the neutron count rate while minimizing the amount of material being used. Finally, it is essential to ensure that the scintillation light can be collected efficiently.

1.5 Original Contribution

The design of effective radiation portal monitors is a critical component in detecting and subsequent interdiction of special nuclear material. Most researchers assume that adequate neutron-gamma discrimination can be achieved by the relatively low mass attenuation coefficient for polymers and taking advantage of the thinness of a detector, but for a common plastic based scintillator, the detector would have to be less than 160 nm in order to have an interaction rate less than one in a million. This work is unique in that the fundamental physics basis of the neutron-gamma discrimination is not attributed to the mass attenuation coefficient but rather to the ranges of the secondary electrons from photon interactions in the material depositing less energy than their neutron counterparts. Current modeling work in large area neutron detectors focuses either with monolithic plastic slab geometries or with neutronic calculations that do not account for light collection and transport. A layered detector design, while not unique, has not been optimized using a genetic algorithm for which the formulation or the problem is quite natural. In addition, little modeling work has been completed on the performance of a radiation portal monitor including light transport, which is a large majority of this work. This work seeks to develop a strategy for the optimization of thin film layered detector designs utilizing a genetic algorithm and determining the expected number of scintillation photons that can be collected on a PMT through simulation.

1.6 Organization of Dissertation

The layout of this document follows the optimization of the design from the detector material to the optimal placement of the material. The physical basis for the detector is described in chapter 2 where a brief introduction of nuclear interactions is considered along with charged particle interactions, scintillations, and optics. Specific methods used in this work are then discussed in chapter 3. These methods include the GEANT4

modeling, MCNPX and XSDRN modeling, and the optimization technique employed. The application of these methods is presented in chapter 4. Finally, chapter 5 serves to summarize the various lessons of the detector design.

Chapter 2

Theory

Detecting radiation utilizing a scintillation detector involves several physical processes, which can be elucidated by imagining a typical interaction in a scintillator. A neutron incident upon a detector interacts by mostly elastic scattering with the nuclei in the RPM material, slowing down to thermal energies. Once thermal, the neutron then has a large probability of interaction with a neutron absorber in the RPM, which releases fission products into the material. These charged fission products then interact with the material by mostly electrostatic attractions, ionizing the matter they pass through, depositing their energy by transferring energy to the kinetic energy of electrons. In the case of a gamma interaction, an energetic gamma may scatter elastically off of an electron through Compton scattering, producing electrons large kinetic energies. For both cases the energetic electrons ionize the matter, producing a cascade of electrons. The material converts the energetic electrons into excited molecules, which can de-excite through the process of scintillation, producing light. The photons produced by scintillation can then be collected with a PMT and transformed into an electrical signal.

Effective design of a radiation portal monitor should then be guided by the physics guiding the processes of interest. The process of the thermalization of the neutrons and nuclear absorptions are discussed in section 2.1. Next, the charged particle interactions

and ranges are discussed in section 2.2. The scintillation processes is discussed in section 2.3, and is followed by a brief discussion of optics in section 2.4.

2.1 Nuclear Interaction Mechanisms

Generally neutrons are born at energies on the order of a few MeV, which is several orders of magnitude above thermal energies. These neutrons than interact with other nuclei in the material, governed by the probability of a particular reaction occurring. The probability of a nuclear reaction can be expressed as probable reaction rate for n neutrons traveling with velocity v a distance x in a material with an atomic density of N. This quantity is defined as the microscopic cross section, σ, and is expressed in (2.1) . This also gives rise to the macroscopic cross section, $\Sigma = N\sigma$, where the interpretation is the probability per unit path length of the process described by the microscopic cross section [Stacey, 2001].

$$\sigma \equiv \frac{\text{reaction rate}}{nvNx} \tag{2.1}$$

If the total cross section is known, the mean free path of the neutron can be calculated as $1/\Sigma_{\text{tot}}$. In polyethylene, a common neutron moderator, the mean free path of a thermal neutron is about 3.7 mm, and decreases with the addition of strongly absorbing material. The collisions in the material causes a neutron to lose energy until they thermalized and their energies are on the scale of the temperature of their environment. For a neutron in thermal equilibrium at 20 °C its energy is 0.025 eV and speed is $2000\,\mathrm{m\,s^{-1}}$. In pure hydrogen it takes 27 elastic collisions for a 2 MeV neutron to slow down to 0.025 eV, and 119 collisions in carbon.

In addition to scattering, there are several other reactions that a neutron may undergo in a detector, the most important of these being absorption. In an absorption reaction the nuclei absorbs the neutron creating a compound nuclei, which is energetically unstable and may release the excess energy by emitting photons or

Table 2.1: Typically isotopes used in neutron radiation detectors

Reaction	Q-Value (MeV)	Thermal Cross Section	Application
$^{3}He + n \rightarrow p + {}^{3}H$	0.756	5,330	Proportional counter gas
$^{6}Li + n \rightarrow {}^{3}H + \alpha$	4.78	940	Lithium glass scintillators
$^{10}B + n \rightarrow \alpha + {}^{7}Li$	2.31	3,840	Plastic scintillators
$^{157}Gd + n \rightarrow \gamma$	various	259,000	various

by fissioning. If the compound nuclei fissions the energy emitted in the reaction (Q-value) is released as the kinetic energy of the fission products. Several nuclear interactions that are of interest for radiation portal monitors are presented in Table 2.1. The dependance of the cross section on the energy of the neutron is shown in Figure 2.1. The desire to thermalize the neutron flux (decreasing the average energy of the neutrons) is evident due to the dramatic increases of the cross sections for lower energies.

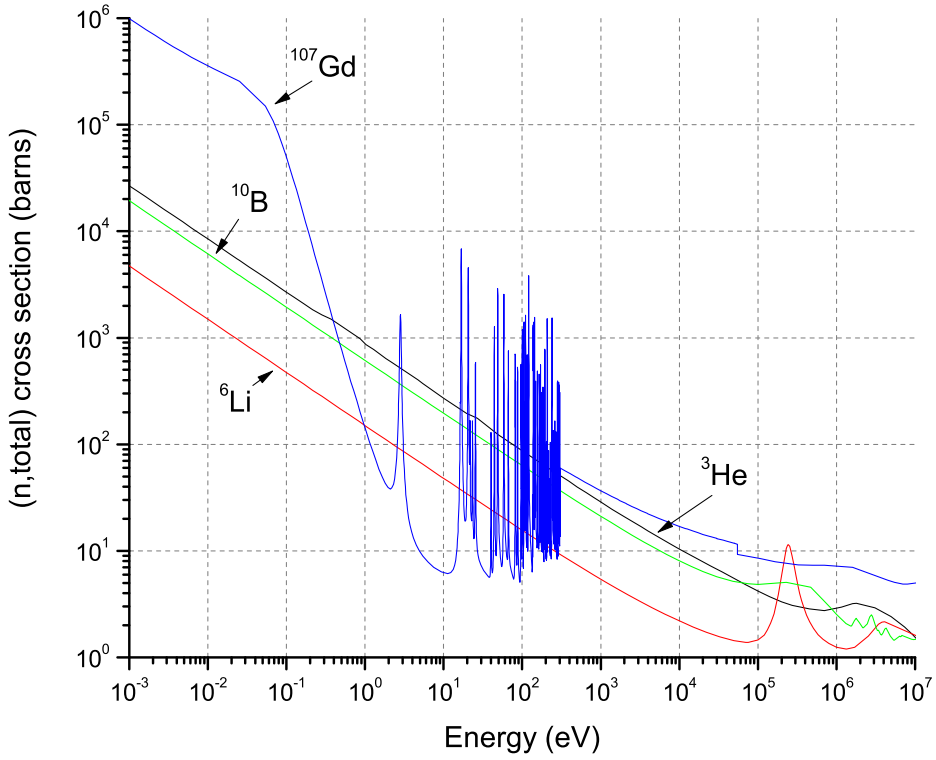

Figure 2.1: Cross sections of typical isotopes used in neutron radiation detectors. Neutrons at room temperature have an energy of 0.025 eV.Data from [ENDF/B-VII, 2013].

2.2 Charged Particle Interactions and Ranges

The theoretical basis for the difference in energy deposition lies in the different mechanisms between charged particle interactions and photon interactions in matter. For photons with energies between approximately 0.5 MeV and 5 MeV Compton scattering is the predominant interaction mechanism between the material and the photon. The probability of an electron having a given kinetic energy after scattering can be expressed as (2.2) (see Appendix A for derivation details)

$$\frac{d\sigma}{dE_e} = 2\pi r_e^2 \sin\theta f(\theta) \left[\frac{1 + \frac{E}{m_e c^2}(1-\cos\theta)^2}{E^2 \sin\theta} \right] \tag{2.2}$$

provided $f(\theta)$ is defined as $f(\theta) = \frac{1}{2}\left(\frac{E'}{E}\right)^2 \left(\frac{E'}{E} + \frac{E}{E'} - \sin^2\theta\right)$. This distribution is shown for ^{60}Co in Figure 2.2. It is then highly likely that the Compton scattered electron will have an energy close to that of the maximum energy for the Compton scattering, 0.96 MeV for the 1.173 MeV photon and 1.12 MeV for the 1.33 MeV photon.

The cumulative distribution function (CDF) is shown in Figure 2.3. In the case of ^{6}Li $(n, ^3\text{H})\,\alpha$ the fission energy is distributed between a triton of energy 2.73 MeV and an alpha of energy 2.05 MeV. The maximum kinetic energy of an electron from a Compton scattering event with an impingement ^{60}Co source is 1.117 MeV (for the 1.332 MeV gamma). In polystyrene with a density of $1\,\text{g}\,\text{cm}^{-3}$, the range of the maximum electron from Compton scattering is around $4.5 \times 10^3\,\mu$m[Berger et al., 2005]. If

Table 2.2: Characteristic kinetic energies of the electrons from a Compton scattering of the two photons from ^{60}Co. It is very likely that an electron will have a kinetic energy greater than 0.8 MeV, which has a range of $0.34\,\text{g}\,\text{cm}^{-2}$ in polystyrene

Gamma Energy	Mean Electron Energy	Median Electron Energy	Maximum Electron Energy
1.17 MeV	0.68 MeV	0.82 MeV	0.96 MeV
1.33 MeV	0.80 MeV	0.96 MeV	1.12 MeV
Average	0.74 MeV	0.89 MeV	

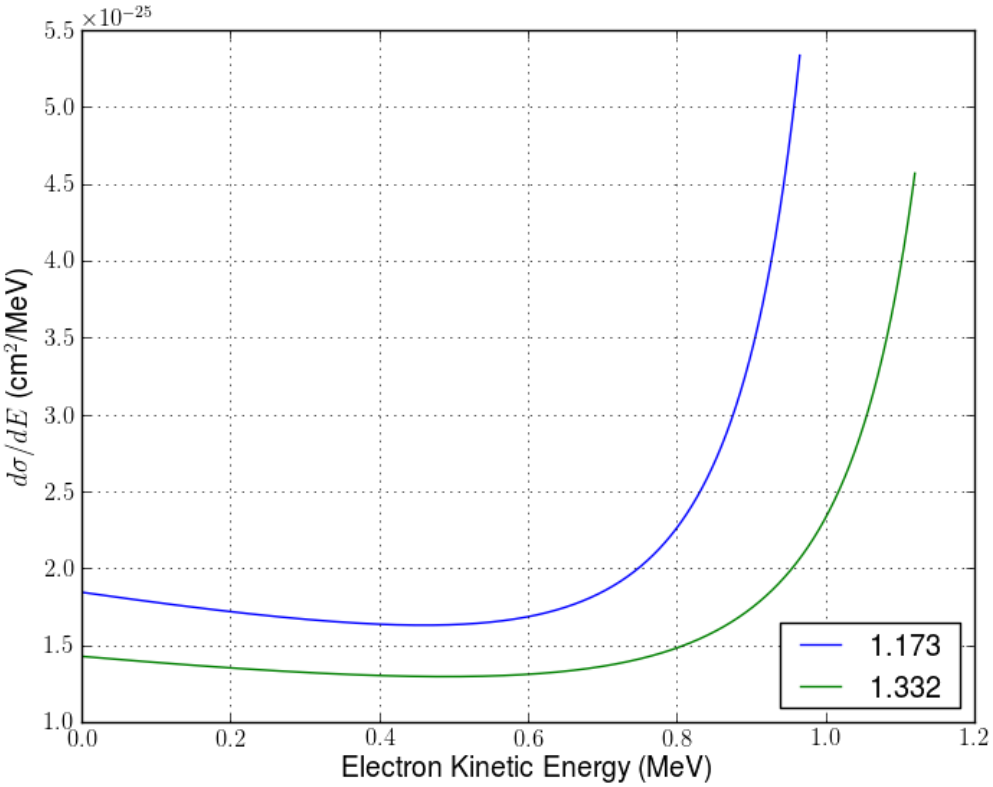

Figure 2.2: Co-60 Compton Electron Differential Microscopic Cross Section. The relative probabilities of a Compton Scattered Electron having a given kinetic energy from ^{60}Co can be determined by their relative differential microscopic cross sections. For example, it almost two and a half times more likely that a Compton scattered electron will have a kinetic energy of 0.95 MeV than 0.75 MeV.

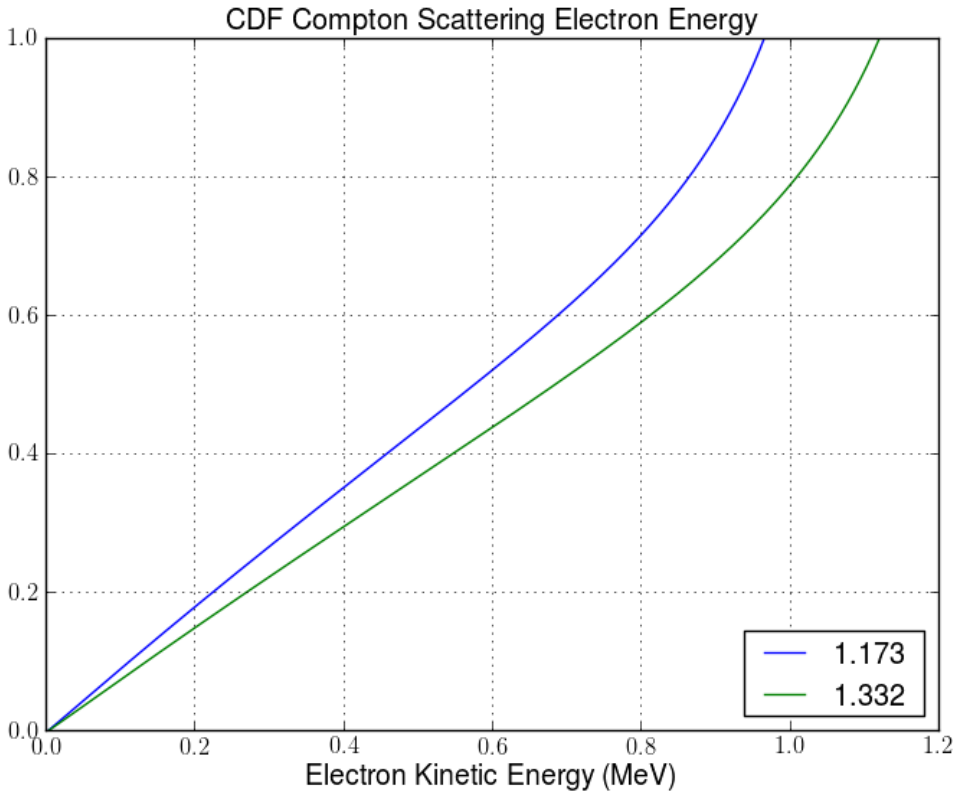

Figure 2.3: Probability of the energy of a Compton Scattered Electron from ^{60}Co. Over half of the electrons from the Compton scattering will have an energy greater than 0.5 MeV

elastic scattering between the alpha, triton and electrons is assumed the maximum kinetic energy of an electron is 1.097 keV for the alpha particle and 1.986 keV for the triton[Turner, 2008]. The range of the electron from a gamma interaction is more than 1×10^3 times greater than the range of electrons from an alpha or triton (Table 2.3). Therefore, it is more likely that the electrons generated by the alpha and the triton deposit significantly more of their energy in a thin film than the electron from a gamma. This is also reflected in the stopping power, where the reaction product secondary electrons have a stopping power 40 times that of the secondary electrons from a gamma [Berger et al., 2005]. The simulated electron range distributions for several energies is shown in Figure 2.4 and summarized in Figure 2.5. The electrons from Compton scattering of ^{60}Co will be on the order of 100 keV , with ranges two orders of magnitude than that of electrons from the charged particle interactions.

Table 2.3: Electron Energy, Range, and Stopping Power [Berger et al., 2005, Turner, 2008]

Electron Parent	Electron Energy	Total Stopping Power MeV cm^2 g^{-1}
gamma	1.12 MeV	1.79
triton	1.99 keV	75.1
alpha	1.10 keV	113

The development of the secondary electron energy ranges so far has been from a simplified treatment of the problem when only the dominant process are considered. Detailed simulations are necessary in order to have a greater understanding of the problem. The energy of the electrons created from an alpha (2.05 MeV), triton (2.73 MeV), and gammas from ^{60}Co were calculated using a GEANT4 simulation, and overlaid on the range of electrons (left axis) as shown in Figure 2.6. It is then clear that the electrons from the ^{60}Co will travel much father than those from the $^6\mathrm{Li}\,(n,\alpha)\,^3\mathrm{H}$ reaction products.

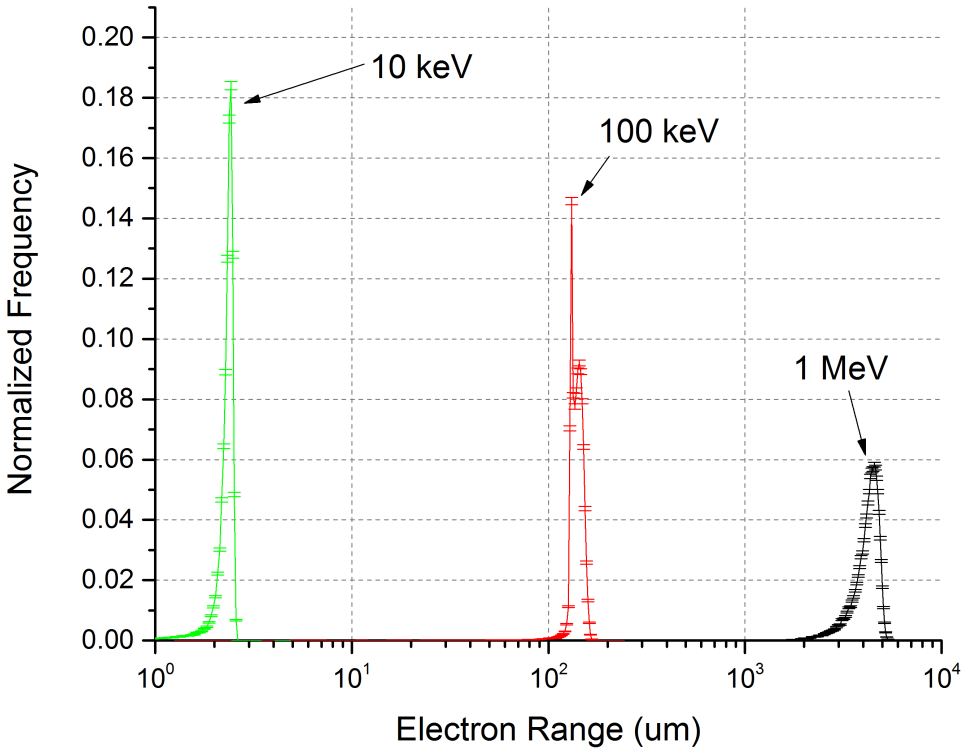

Figure 2.4: Simulated range of 1 MeV, 100 keV, and 10 keV electrons.The simulation is a 10 m box of polystyrene completed with the GEANT4 toolkit. More details of the simulation can be found in section F.8.

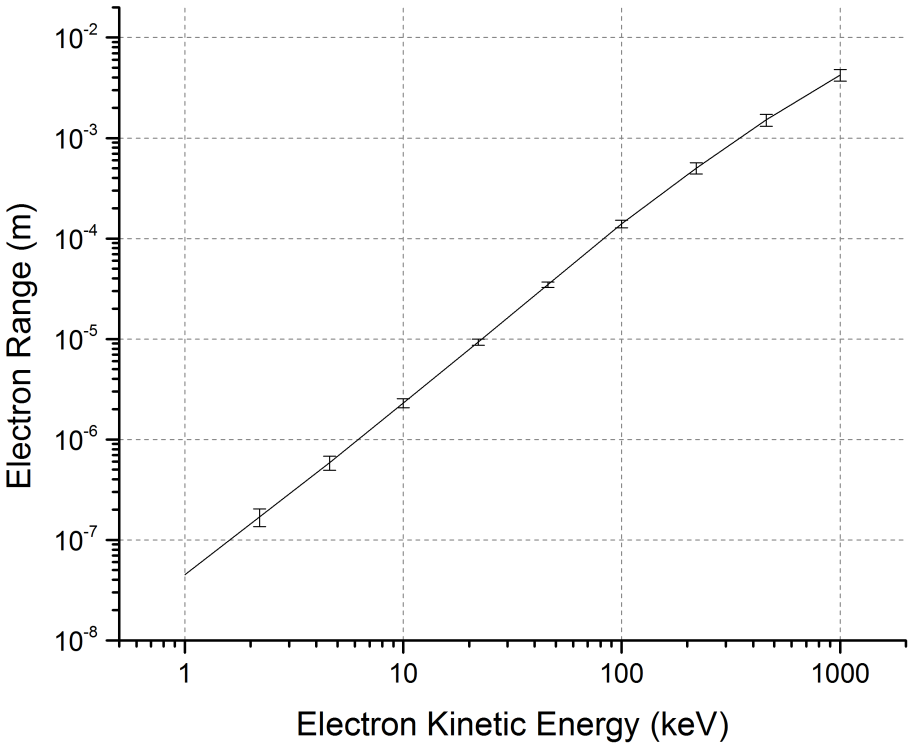

Figure 2.5: Simulated electron ranges for electron kinetic energies ranging from 1 keV to 1 MeV.The simulation is a 10 m box of polystyrene completed with the GEANT4 toolkit. More details of the simulation can be found in section F.8.

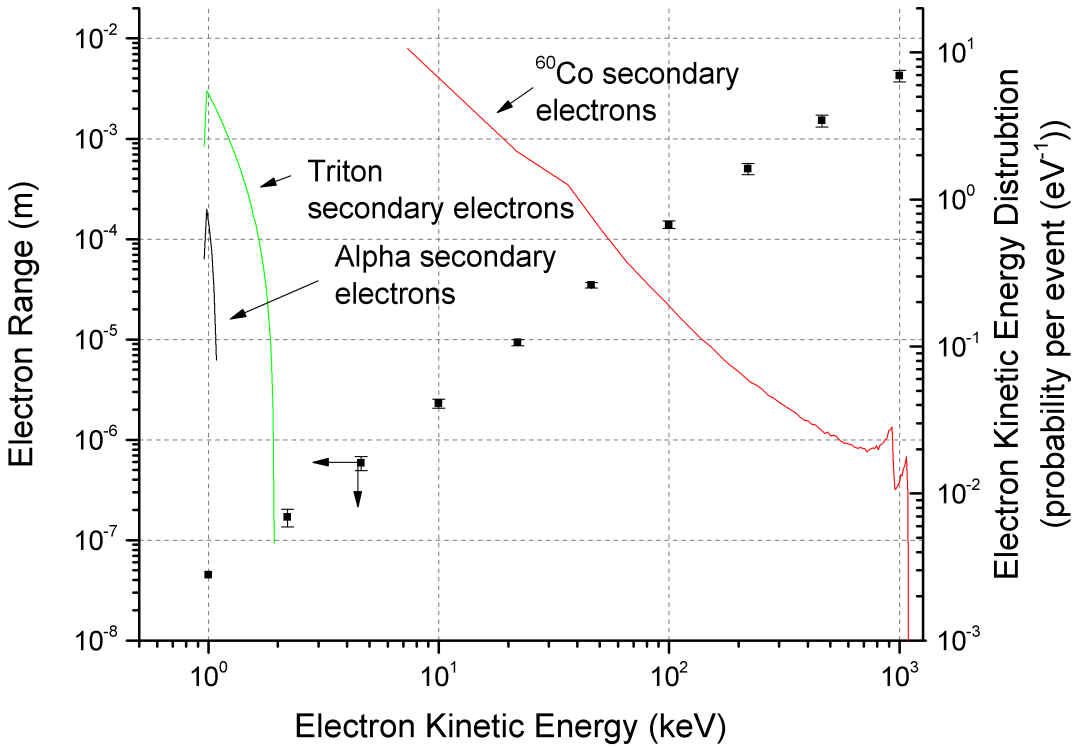

Figure 2.6: The electron range corresponding to the square dots is shown on the left axis. The distribution of the kinetic energy of electrons from 2.05 MeV alpha, 2.73 MeV triton, and secondary electrons from ^{60}Co are shown on the right. The ^{60}Co electrons have energies much greater than the alpha and triton, and their corresponding range is orders of magnitude greater than the ranges of the electrons from the alpha and triton. For example, the average energy of a secondar electron has an kinetic energy around 100 keV, which corresponds to a range of 0.1 mm. The simulation is a 10 m box of polystyrene completed with the GEANT4 toolkit. More details of the simulation can be found in section F.8.

2.3 Scintillation Mechanisms

Scintillation detectors (the detectors on which this work is based) utilize a scintillator to convert ionizing radiation into photons. In inorganic scintillators these photons arise from excitations of electrons in the band gap of the material or dopant, while for organic scintillators the photons generally come from relaxations of aromatic rings in the molecule. Typically the light emitted from the primary phosphor is of a wavelength that is not suitable for detection with a photomultiplier tube, so a secondary fluor is added to absorb and reemit the light at a more favorable wavelength for detection. The process of scintillation in organic scintillators is explained in more detail in subsection 2.3.1, while the number of photons emitted for different types of ionizing radiation is discussed in subsection 2.3.2.

2.3.1 Organic Scintillators

An organic scintillator generally has a π-electron structure similar to that of Figure 2.7 with typical energy levels as shown in Figure 2.8. An incoming electron (liberated from the energy deposition of the ionizing radiation) then excites one of the modes of the π-electron structure. Higher singlet states rapidly (on the order of picoseconds) relax to the first singlet state, and excessive vibrational energy (populations of the vibrational sates) is lost. Thus, after a short period of time the entire excitation population is in the S_{10} state, and the decay of this state creates the prompt fluorescence. The excitations of triplet states typically yield delayed scintillation events or phosphorescence. An excited triplet states immediately decays to the T_0 state by internal degradation without a photon emission. The T_0 state typically decays by interacting with another T_0 state in a $T_0 + T_0 \rightarrow S^* + S_0 + h\nu$ transition. The excited singlet state S^* then also decays to the S_0 state. The $T_0 + T_0$ transitions is slower than direct singlet state de-excitations, and results in a slow component of the pulse, which can be used for pulse shape discrimination.

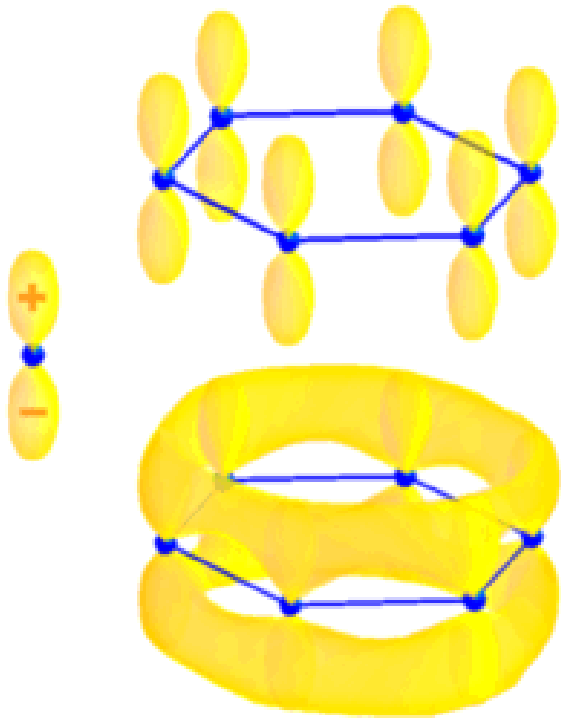

Figure 2.7: Example electron orbitals for Benzene. The distributed, non-localized electron structure of the bottom image is typically of that of scintillators.

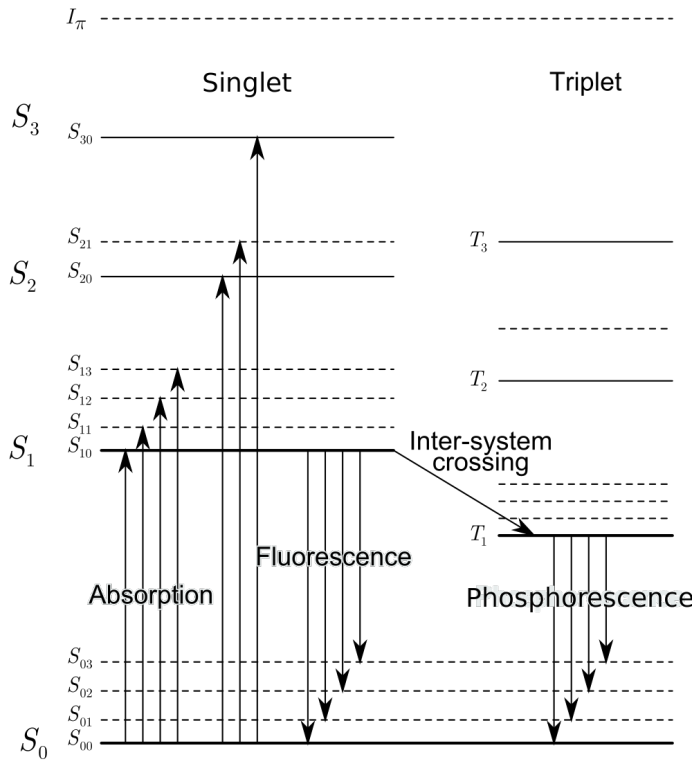

Figure 2.8: Typical π-electron structure of an organic molecule. The ground state of the molecule is shown as S_0, and excited single states are S_1, S_2 etc The triplet states are T_1, T_2, with the vibrational states as S_{OO}, S_{01}, S_{02} and so forth. Figure from Wikipedia.

The light output of an organic scintillator can be empirically related to the energy deposition in the scintillator through the Birks equation [Birks, 1951]. In the absence of any quenching it is assumed that the light output per unit length is directly proportional to the energy deposition per unit length (2.3)

$$\frac{dL}{dx} = S_B \frac{dE}{dx} \tag{2.3}$$

where S_B is the absolute scintillation efficiency and $\frac{dE}{dx}$ is the linear stopping power . If quenching of the light from molecules damaged by the radiation is also assumed to be proportional to the energy deposition per track length, than the Birks equation can be written as (2.4)

$$\frac{dL}{dx} = \frac{S_B \frac{dE}{dx}}{1 + kB \frac{dE}{dx}} \tag{2.4}$$

where kB is the Birks parameter which accounts for the quenching of the light. For low stopping powers (or particles with a very high energy) the light output per unit track length is linear as the quenching term can be neglected. However, for particles with a large stopping power the light output along the track length becomes saturated by quenching. This difference in the pulse height accounts for that difference in light output from a 1 MeV electron compared to a 1 MeV alpha. The *alpha to beta* ratio provides a measure of this effect, and for the GS20 glass is it typically around 0.23. This effect is critical in the developed detectors are the reaction products of of the ^{6}Li neutron absorption are both heavily charged particles subject to this effect. Thus, while there is 4.78 MeV of reaction product energy released in the neutron absorption, the low alpha to beta ratio of the material limits the actual number of scintillation events compared to those produced by a 4.78 MeV beta (electron).

2.3.2 Pulse Height Deficit

The concept of alpha to beta ratio is extended for other charged ions as the pulse height deficit. The pulse height deficit is defined as the number of photons produced per energy of the primary particle (usually a heavy charged ion) relative to the number of photons produced per energy by an electron of the same energy. This is measured as the difference between the energy of the heavy ion and its apparent energy from the pulse height (that produces the same number of photons). Several researchers have investigated the light output of scintillators in response to different types of ionizing radiation[Verbinski et al., 1968]. Figure 2.9 summarizes example results in which the pulse height deficit is apparent for the as the charged ions become heavier.

An illustration of the energy deposition between the different particles resulting in the pulse height deficit is presented in Figure 2.10. The electrons, with their low stopping power and broad track structure deposit their energy over a broader range than do the heavy charged ions (which tend to have rather collimated tracks). Thus, the heavy charged ions deposit a large amount of their energy in a small volume, completely ionizing that volume and inhibiting scintillation.

For a portal monitor scintillator the most likely charged particles would be alphas, tritons and electrons. GEANT4 has the capability to simulate light quenching by setting an appropriate Birks parameter, and Figure 2.12 presents GEANT4 simulated photon distributions in polystyrene with a PPO-POPOP fluor and an assumed light yield of 1,000 photons per MeV. For highly energetic particles the electrons are almost an order of magnitude more efficient at creating light than the tritons, and about 90 times more efficient than the alphas, as shown in Figure 2.11. However, it is unlikely that many electrons originating from ^{60}Co interactions in the scintillator will have an energy in the 1 MeV range, more likely that they will be in the 100 keV range. Thus, as shown in Figure 2.12 the triton from the ^{6}Li reaction will produce about an factor of five more photons than at 100 keV, and dominates the number of photons produced by the alpha particle.

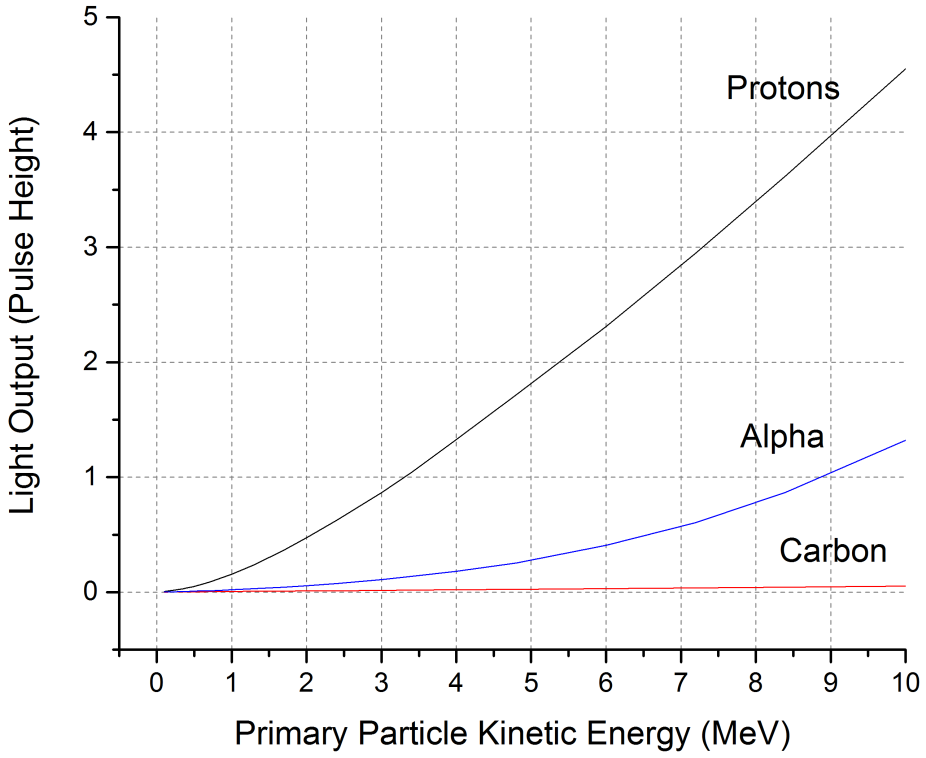

Figure 2.9: Light yield non-proportionality of anthracene. For the same kinetic energy the protons produce more photons alpha, which in turn produces more photons than the carbon ions. This is an example of the pulse height deficit. The alpha to beta ratio of anthracene is 0.29 [Hull et al., 2009]. The figure data is from [Verbinski et al., 1968].

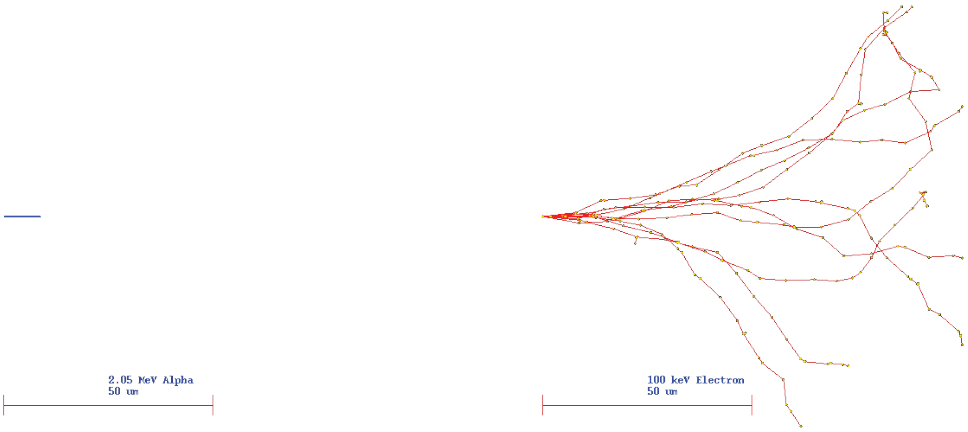

(a) 2.05 MeV Alpha

(b) 100 keV Electron

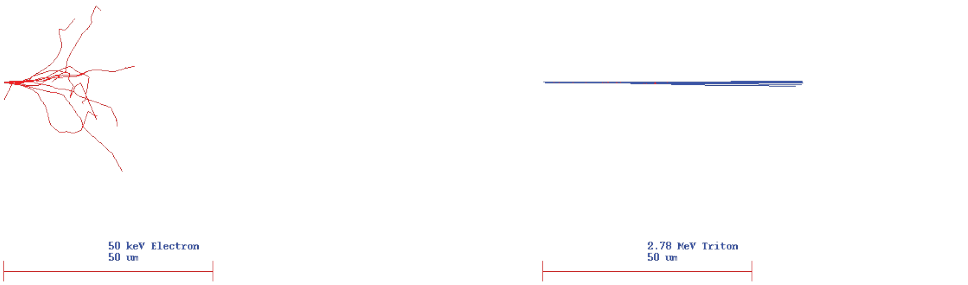

(c) 50 keV Electron

(d) 2.73 MeV Triton

Figure 2.10: GEANT4 simulated Particles tracks of a 10 keV electron, 100 keV electron, 2.05 MeV alpha, and 2.73 MeV triton. The electron tracks are broader than the heavy ion tracks, resulting in a greater spread of the energy deposition and less quenching.

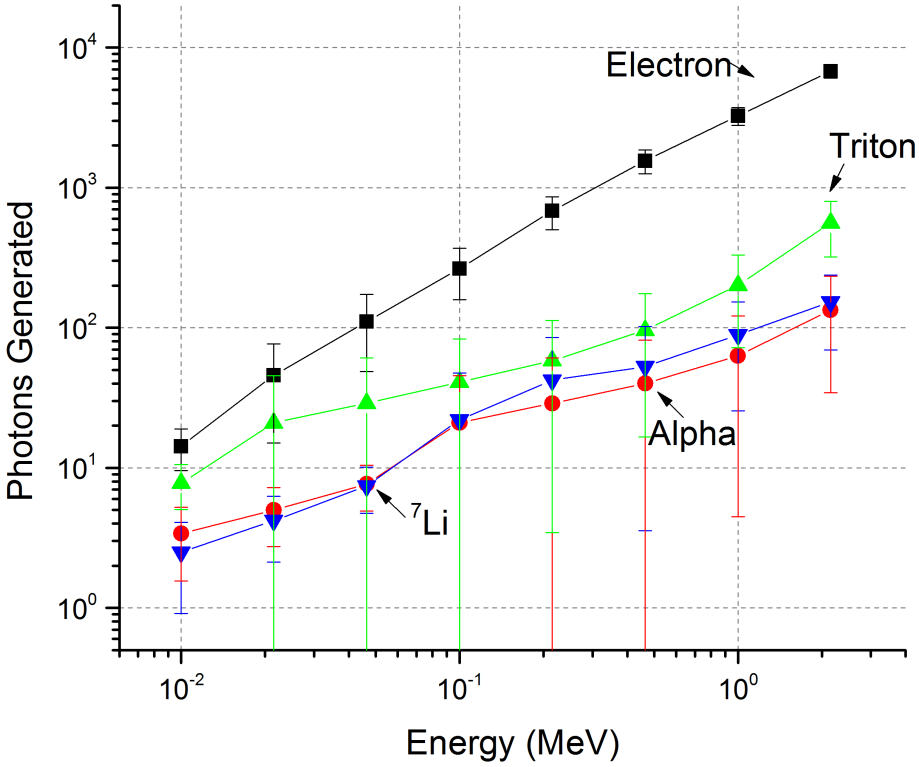

Figure 2.11: Simulated number of optical photons generated from electrons, alphas, tritons and ^{7}Li.The simulation is a 10 cm box of 10% loaded ^{6}LiF polystyrene based scintillator assumed to have a light yield of 3000 photons /MeV completed with the GEANT4 toolkit. More details of the simulation can be found in section F.9.

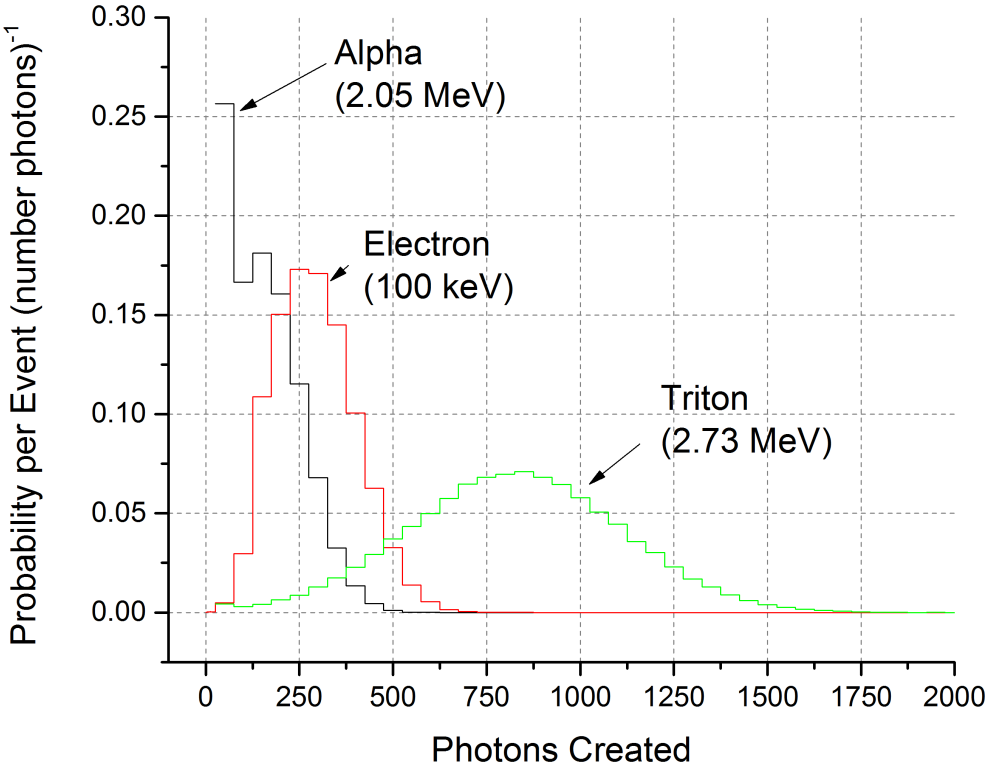

Figure 2.12: Simulated optical photons distributions for the particles of interest in a portal monitor. The energy of the electron was chosen to be the average energy deposited by ^{60}Co in 1 mm of polystyrene. The simulation is a 10 cm box of 10% loaded ^{6}LiF polystyrene based scintillator assumed to have a light yield of 3000 photons /MeV completed with the GEANT4 toolkit. More details of the simulation can be found in section F.9.

Table 2.4: GEANT4 simulated number of optical photons produced for the ^{10}B and ^{6}Li neutron absorptions. The scintillator is assumed to have a light yield of 1,000 photons per MeV of electron energy.

	Particle	Photons Produced	Pulse Height Deficit
^{10}B	α (1.78 MeV)	72 ± 8	27
	^{7}Li (1.02 MeV)	42 ± 8	
	electron (2.78 MeV)	3,030 ± 160	
^{6}Li	α (2.05 MeV)	87 ± 9	8.5
	triton (2.75 MeV)	528 ± 23	
	electron (4.78 MeV)	5,250 ± 300	

The pulse height deficit is computed by simulation of the charged particles and the corresponding electron. This analysis yields a pulse height deficit for the ^{6}Li reaction as 8.5, and 27 for the ^{10}B. These results are summarized in Table 2.4.

2.4 Optics and Light Transport

Effective scintillator detectors collect as much light as emitted from the scintillator as possible. In practice two effects limit the fraction of the emitted light collected; the optical self-absorption in the material and losses at the edges of the optical surfaces [Knoll, 2009]. The optical self-absorption of a scintillator is a material property in which photons are reabsorbed by the material. This effect is important for large area scintillators and for scintillators which are not optically clear, both of which apply to the developed polymeric scintillators. Typically this effect is mitigated by the use of a wavelength shifting fiber in which the light is transferred to a material which has a much lower optical self-absorption.

Light collection of a scintillation event is emitted isotropically, and therefore only a very small fraction of the photons can travel directly to a photon detector surface. The majority of the light must then be collected by reflecting back into the medium. Snell's law governs the reflection of light at an optical boundary, and there are two

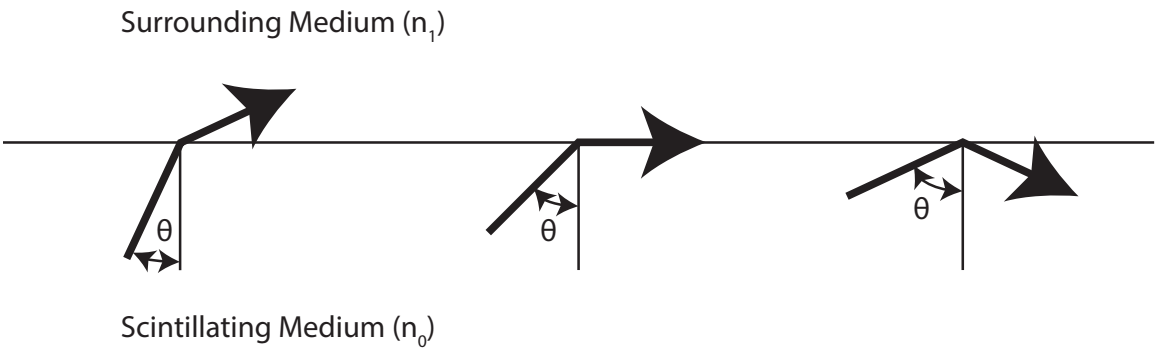

Figure 2.13: Reflection of light at an optical surface is governed by Snell's law. The fraction of light reflected back into the material is greatest at an angle of incident equal to θ_c

cases to consider as shown in Figure 2.13 and described by Snell's Law, (2.5)

$$\theta_c = \sin^- 1 \frac{n_1}{n_0} \tag{2.5}$$

where θ_c is the critical angle, n_1 is the index of refraction of the surrounding medium and n_0 is the index of refraction of the scintillator. If the angle of incidence, θ, is greater than the critical angle total internal reflection will occur. When the angle of incidence is less than the critical angle particle reflection (or *Fresnel* reflection) will occur and there will be partial transmission of the photons to the surrounding medium. To ensure that the light stays within the desired medium it is usually encased in a reflector, of which there are two types (Figure 2.14). A polished metallic surface (such as aluminized mylar) may be applied as a specular reflector which are generally better when the length is much longer than the thickness[Gobain, 2012]. A diffusive reflector, such as teflon tape, is better for conditions when the detector is thick compared to its length [Knoll, 2009].

Photons that are emitted exactly along the direction of the scintillator will only be effected by the absorption length of the material (typically on the order of 100 cm to 400 cm for optically clear materials[Gobain, 2008]) while photons emitted in directions nearly normal to the direction of the scintillator will need to undergo thousands of

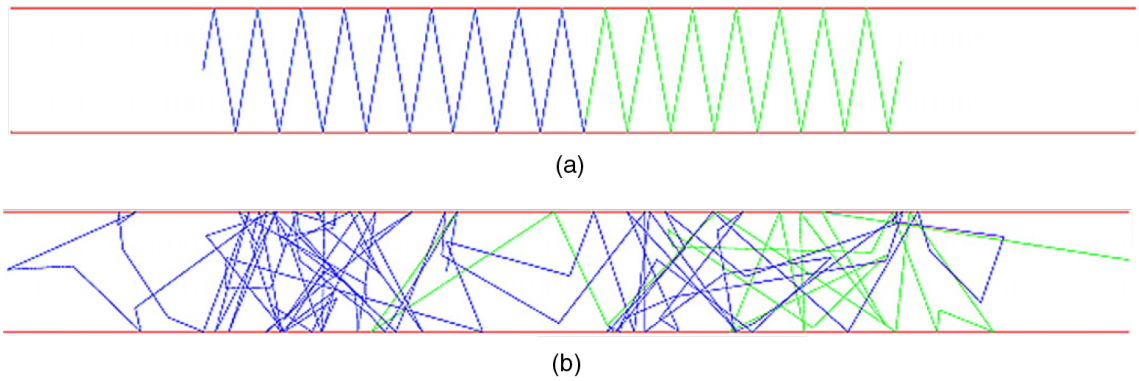

Figure 2.14: Specular reflection (a) in which the light in a single incoming direction is emitted as a single outgoing direction. The rough surface of a diffusive reflector (b), causes the light to be reflected at many angles. Figure from [Riggi et al., 2011].

reflections in order reach the PMT, which can double the length the photons must travel. For perfect specular reflection it has been shown through simulation the the number of photons throughout a scintillating strip is only reduced by the optical absorption in that strip [Riggi et al., 2011]. In a realistic scintillator with a diffusive reflector the number of photons decreases by a factor of more than ten 50 cm from the origination of the photon[Riggi et al., 2011].

In the cases of a large scintillating detector, such as the one presented in this work, it may be necessary to employ more than one PMT to collect the light. In such cases the use of light pipes may enhance the collection efficiency. Light pipes are not without costs, however, as they are generally of a high index of refraction to maintain a high internal reflection, and it is desirable to optically match the surface at which the scintillator is to be viewed to prevent reflection.

The magnitude of the difficulty of collecting the optical photons is illustrated in Table 2.5. The simulation is a slab of PVT based scintillator (EJ-200) that is 200 cm long, 30 cm wide, and of thickness between 100 µm to 1 cm with perfectly polished sides so that the only interactions will be specular reflection due to Snell's law. The geometry of this simulation is shown in Figure 2.15. While this simulation is not entirely representative of the light production (a uniform volumetric distribution would

Table 2.5: Fraction of photons detected on a single PMT in a slab of various thickness from a point source located 25 cm and 50 cm from the detector. The optical properties simulated are of that of a PVT based scintillator with an optical attenuation length set to 200 cm.

Slab Thickness	Fraction Collected (50 cm)	Fraction Collected (25 cm)
100 µm	1.1%	1.1%
220 µm	1.3%	1.7%
460 µm	1.5%	1.9%
1 mm	2.2%	2.8%
2.2 mm	3.5%	4.2%
4.6 mm	5.1%	6.2%
1 cm	6.3%	7.3 %

more accurately reflect the production in the scintillator) and the boundary conditions (perfectly smooth, polished surfaces are unrealistic), it demonstrates that there is a large reduction in the light collection due to having a thin detector. It is also observed for the thin films that the distance from the PMT to the origination of the light has little effect as the rays need to start out nearly perpendicular to the PMT surface.

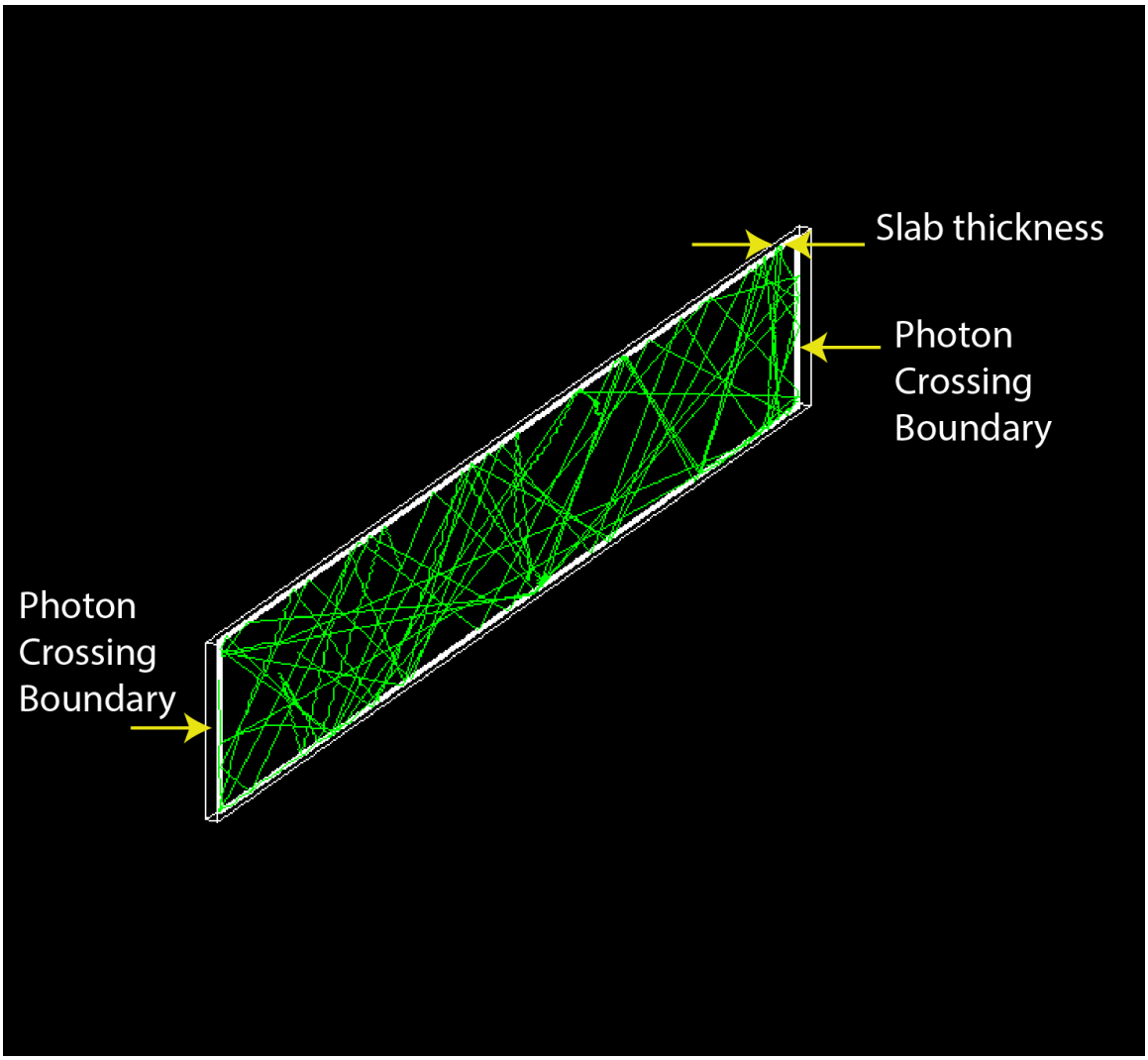

Figure 2.15: Geometry of a the light collection in a thin scintillating slab. The material is a PVT based scintillator, with perfectly polished surfaces. Three optical photon events (represented by the green lines) are shown. The PMT's are considered to the the face of the material.

Chapter 3

Methods

In the design of a detector the theory must be supplemented by accurate models of the complex interactions in the radiation portal monitor to determine the performance. Once the performance of a design has been determined a method must be chosen for how to optimize the design to ensure the best use of the materials while meeting the performance criteria. Three models of the detector physics are employed; two Monte Carlo based methods and one deterministic method. The deterministic model, XSDRN [Greene et al., 2011b], solves a discretized one dimensional Boltzmann transport equation, and is described in section 3.4. Probabilistic models follow the path of individual neutrons with interactions based on the probability of a given event occurring. Such codes are also known as Monte Carlo models, for which MCNPX (described in section 3.3) and GEANT4 (described in section 3.2) are well known examples. MCNPX is employed for detailed neutronic modeling, while GEANT4 is employed for optical photon simulations and detailed energy deposition calculations.

The optimization of the detector is completed by a genetic algorithm using the XSDRN model to quickly simulate a large number of geometries. Small perturbations on these geometries are then modeled with the MCNPX model to ensure that the results are accurate and that true convergence has been reached. The genetic algorithm is introduced in section 3.5.

3.1 Pulse Height Discrimination

Generally, two methods are available for discrimination; 1) pulse shape discrimination and 2) pulse height discrimination. In pulse shape discrimination the different decay times between the neutron and gamma pulses are exploited to develop a metric that allows for the classification of the pulse, and preforms best when the pulses are noticeably different. Pulse height discrimination is based on setting a pulse height discriminator that acts as a partition between two classes of pulses.

A pulse height discriminator may be set by hardware electronics or by software. A mathematical lower level discriminator (MLLD) is then introduced to clarify the determination of what discriminator setting will be necessary to achieve a given intrinsic efficiency criteria. The intrinsic efficiency for a given MLLD is determined for a sample by first determining the photon fluence over the sample (usually by a MCNPX calculations, these calculations are explained in Appendix D). The recorded spectra is then normalized the photon fluence to determine the count rate per incident photon per channel. As the intrinsic efficiency is defined as the count per incident quanta of radiation, the spectra needs to be integrated from the channel number represented by the MLLD to the end of the spectra over the channels to determine the count rate. By summing only the counts that are above the discriminator represented as the MLLD these counts are then discarded from the analysis. A formulation of the MLLD is presented in (3.1),

$$\epsilon_{\gamma,int}\left(MLLD\right) = \frac{\int_{MLLD}^{\infty} p(x)dx}{\Phi} \tag{3.1}$$

where $p(x)$ is the spectra as a function of channel number and Φ is the is the incident gamma flux. By computing the gamma intrinsic efficiency as a function of the MLLD, one only needs to find what MLLD corresponds to having a intrinsic efficiency of less than one in a million.

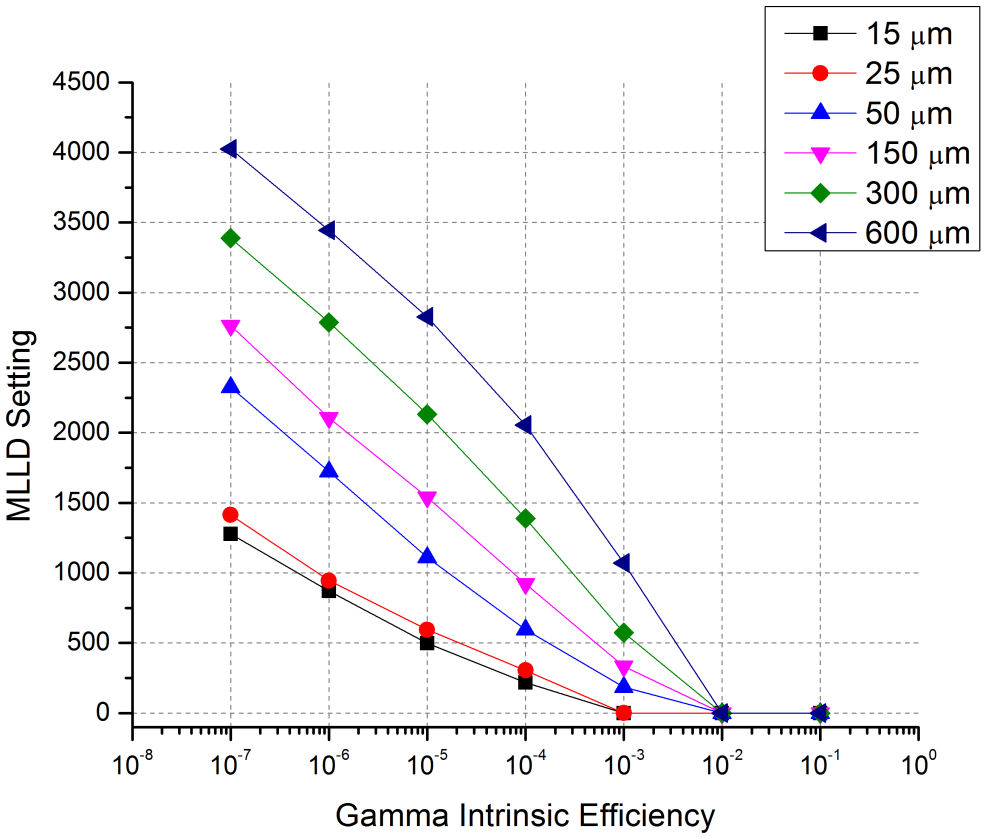

Figure 3.1: Gamma intrinsic efficiency versus the pulse height discriminator setting (MLLD) to achieve the corresponding level of discrimination in 10% loaded polystyrene. It is observed that there is a change in the shape of the curves reflecting the increased fraction of energy deposition in thicker films relative to the thinner films.

A sequence of polystyrene films (10% by weight enriched LiF) were fabricated by Dr. Mabe and analyzed for their ability to achieve different gamma intrinsic efficiencies in the MLLD framework. These measurements and calculations, presented in Figure 3.1, demonstrate the utility of the MLLD. This figure shows, as expected, that increasing the MLLD causes a lower intrinsic efficiency as counts below the MLLD are discarded. Thicker films, where more energy is deposited and thus produce more photons, require higher MLLD settings in order to achieve the same level of discrimination as their thinner counter parts.

Table 3.1: Fraction of Neutron Count Rate Above Discriminator Setting in 10% loaded polystyrene

Thickness	Neutron Fraction
15 µm	0.21
25 µm	0.30
50 µm	0.16
150 µm	0.009
300 µm	0.002
600 µm	0.002

A pulse height discriminator to achieve the necessary gamma discrimination will not be without cost, however, due to an overlap between the neutron and gamma pulse height distributions. For example, the calculated gamma intrinsic efficiency for six polymeric films along with the neutron response of two of the films is shown in Figure 3.2, In order to achieve an intrinsic efficiency of less than 1×10^{-6} the MLLD must be set above 2,000 channels, discarding a large majority of the neutron counts. It is observed that if the films are thin enough (less than 150 µm) it is possible to have a significant count rate above the mathematical lower level discriminator necessary for the pulse height discrimination of one in a million. This is seen by the 50 µm film and the 150 µm film having the tail of their neutron spectra above the pulse height discriminator necessary for an intrinsic efficiency of 1×10^{-6}. Table 3.1 shows the fraction of neutron count rate that is above the MLLD necessary for $\epsilon_{int,\gamma n} \leq$ 1E−6. Films less than 50 µm have over 16% of the counts above the necessary discriminator setting, while thicker films have a factor of 10 less. In addition it is observed in Figure 3.2 that for neutrons, thicker films only enhance the resolution of the film and do little to increase the light yield, as most of energy from a neutron event is captured in the film.

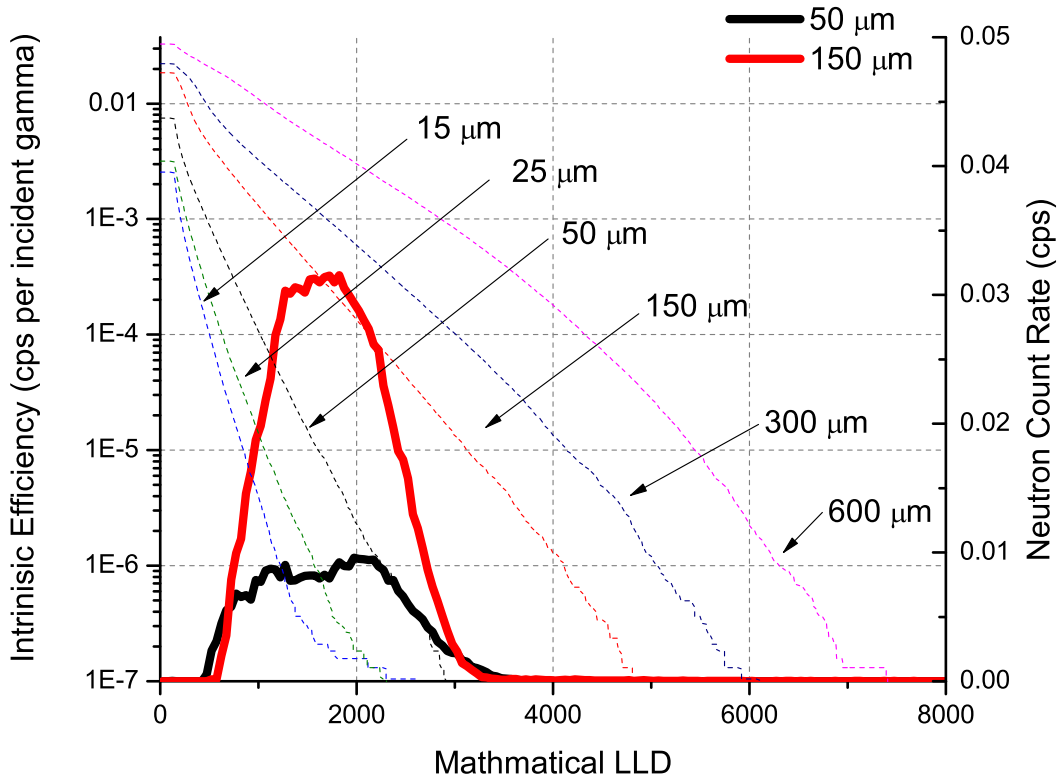

Figure 3.2: Gamma intrinsic efficiency (dashed lines) plotted against neutron counts (solid). The gamma spectra has been normalized by the number of incident photons upon the sample, while the neutron spectra has not. The material is polystyrene loaded with 10% ^{6}LiF.

3.2 GEANT4 Modeling

GEANT4 is a free toolkit for the simulation of particles as they travel through matter[Agostinelli et al., 2003]. In general two types of applications were authored with the GEANT4 toolkit; ranges along with energy deposition and light transport. All of the applications shared a common electromagnetic physics list based on the Livermore data set, and a cross section driven hadron physics list was used for the neutron interactions. Ions were transported with the general ion physics list which contains detailed alpha and triton models. Optical photons were transported with

the default Optical Photon physics list. More details on the GEANT4 toolkit may be found in Appendix C.

3.2.1 Energy Deposition Simulations

The GEANT4 toolkit has the ability to track the energy deposition in different materials as well as the tracking of electrons to a least 1 keV[Agostinelli et al., 2003]. It is proposed to represent the detector geometry as a single layer of neutron absorbing thin polymeric film mounted on top of a non-scintillating material (PMMA). For simplicity, the initial events for runs will be chosen by setting up a particle gun for thermal (0.025 eV) neutrons upon the detector and for both gammas resulting from a ^{60}Co decay. It is expected that the Livermore data-driven parameterized electromagnetic physics will be necessary to calculate the ionizing energy deposition, extending the standard electro-magnetic physics down to 1 keV. The neutron interactions will be simulated with a hadronic modules, using the high performance flavored modules to use the ENDF cross sections to calculate the interaction rates.

Energy Deposition Validation

The validation of this GEANT4 simulation was completed by reproducing the single collision energy loss in water as well as comparing the spectral shapes and averages of simulated and measured spectra. The reproduction of the single collision energy loss will ensure that the electron physics are implemented correctly, while the simulation of the polymeric film energy deposition allows the user to gain confidence that the correct tracking and binning analysis has been implemented.

The simulation was validated by reproducing the single collision energy loss for water as well as comparing spectra shapes and averages of simulated spectra to the measured spectra. The single collision energy loss spectra for water that was simulated is shown in Figure 3.4. In general there was excellent agreement between the simulated energy spectra and a previously published spectra[Turner et al., 1982],

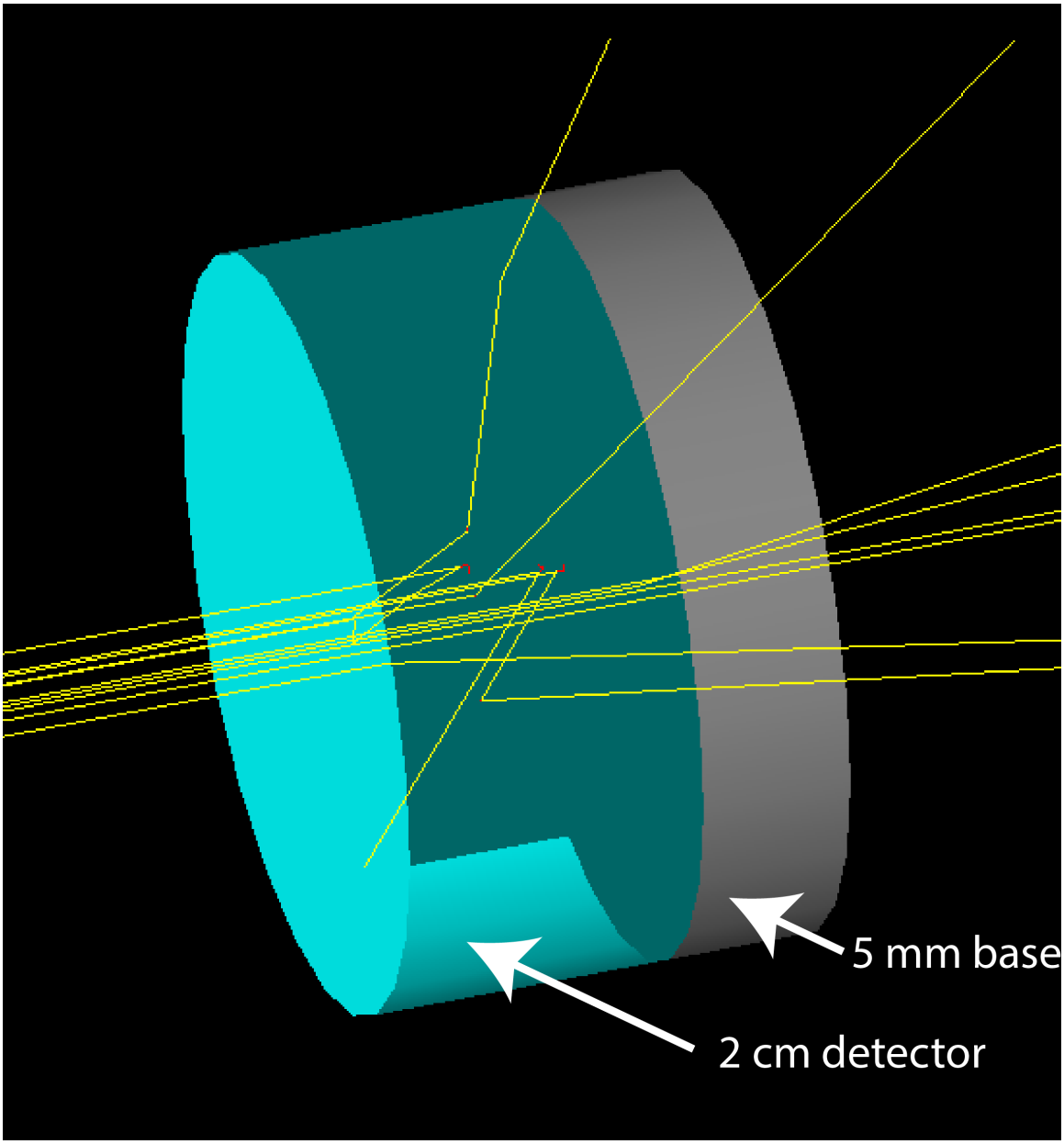

Figure 3.3: GEANT4 Geometry for the Simulation of Energy Deposition. What is shown are ten photons from a ^{60}Co source impingement upon a 2 cm thick detector. The photon tracks are shown in yellow, while the electron tracks are shown in red.

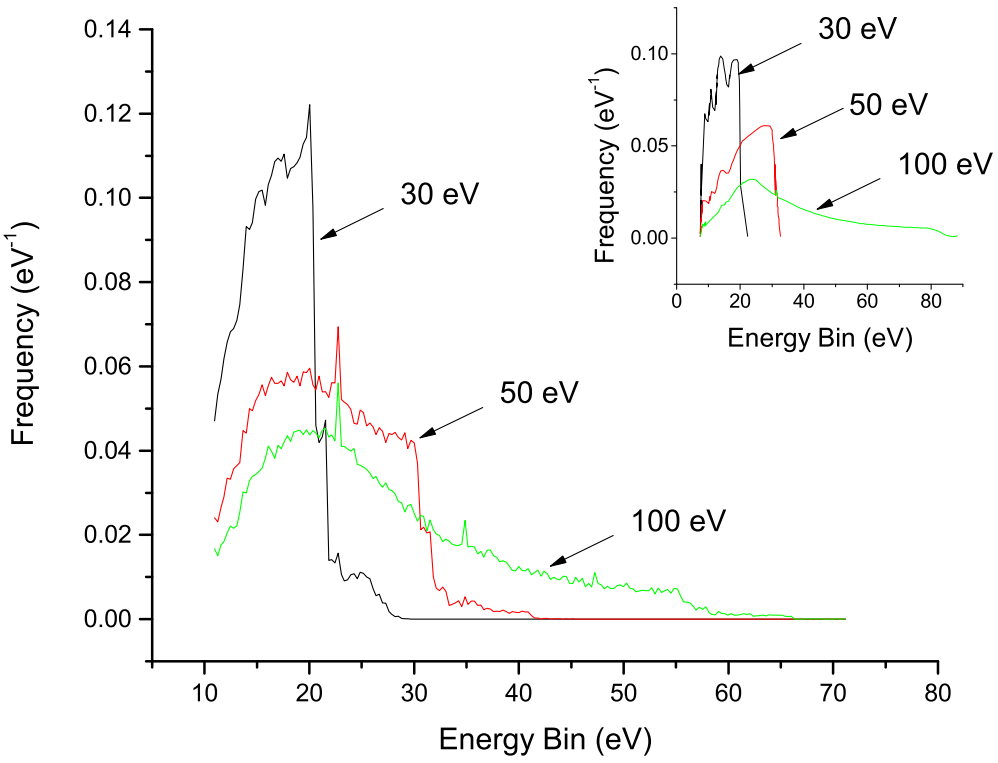

Figure 3.4: Simulated single collision energy loss of electrons in water. The GEANT simulated data is shown in the foreground, while the insert contains the data from [Turner et al., 1982].

with the simulated spectra having much better resolution than the reference. It is thought that this is due to the water model in GEANT4 having better cross sections than the previously published spectra.

The validity of the GEANT4 simulation for thin films is determined by comparing the spectra shapes of measured spectra to simulated energy deposition. Example gamma simulated spectra are shown in Figure 3.5, where for thin films there is an almost linear increase in the spectra endpoints with film thickness. The simulated energy deposition per incident photon from a ^{60}Co source and the measured pulse height spectra from the ^{60}Co irradiator per incident photon can be compared by finding a calibration between them, in this case the Compton edge of a thick sample.

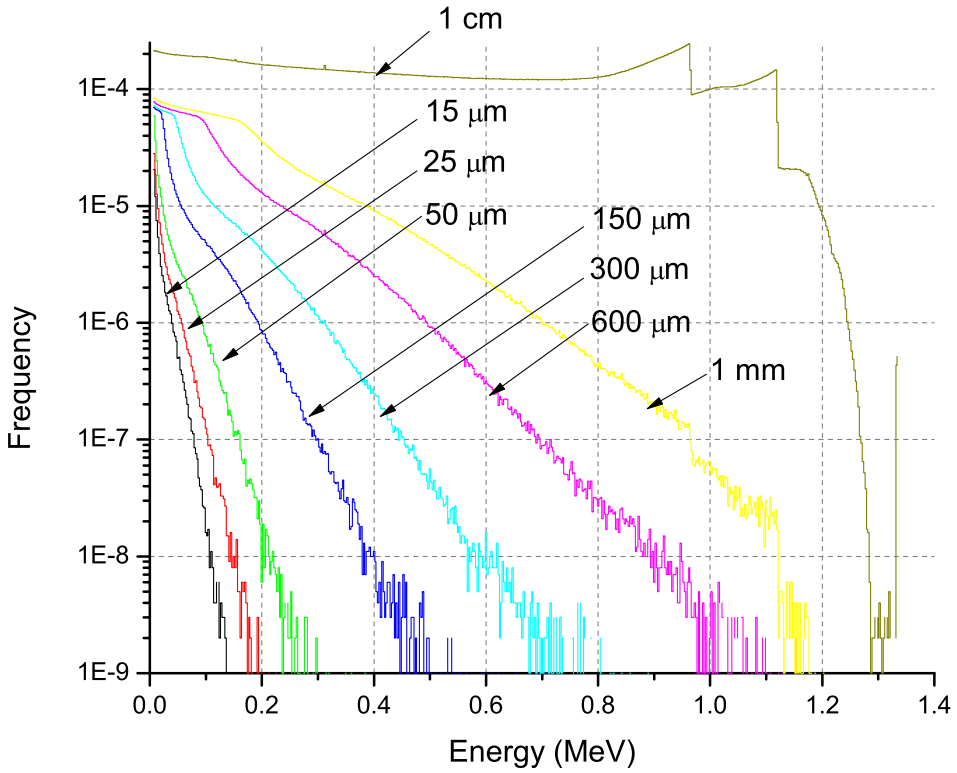

Figure 3.5: GEANT4 simulated energy deposition from incident the 1.17 MeV and 1.33 MeV photons of ^{60}Co in polystyrene films loaded with 10% ^{6}LiF of different thickness. The Compton edge of the two photons is clearly visible for the 1 cm film, while the other films show an almost linear increase in energy deposited with thickness.

The measured Compton edge of a 1 mm film can then be correlated with the simulated energy, as shown in Figure 3.6. The energy of this feature on the measured spectra was then compared to the energy on the simulated spectra, with all of the values being within 10%.

A direct comparison between the simulated average energy deposition and pulse height are shown in Figure 3.7 and Figure 3.8. The average energy deposition is shown on the left axis and the spectra average light yield (SALY, or the pulse height) is shown on the right axis. The largest amount of energy that can be deposited in the neutron

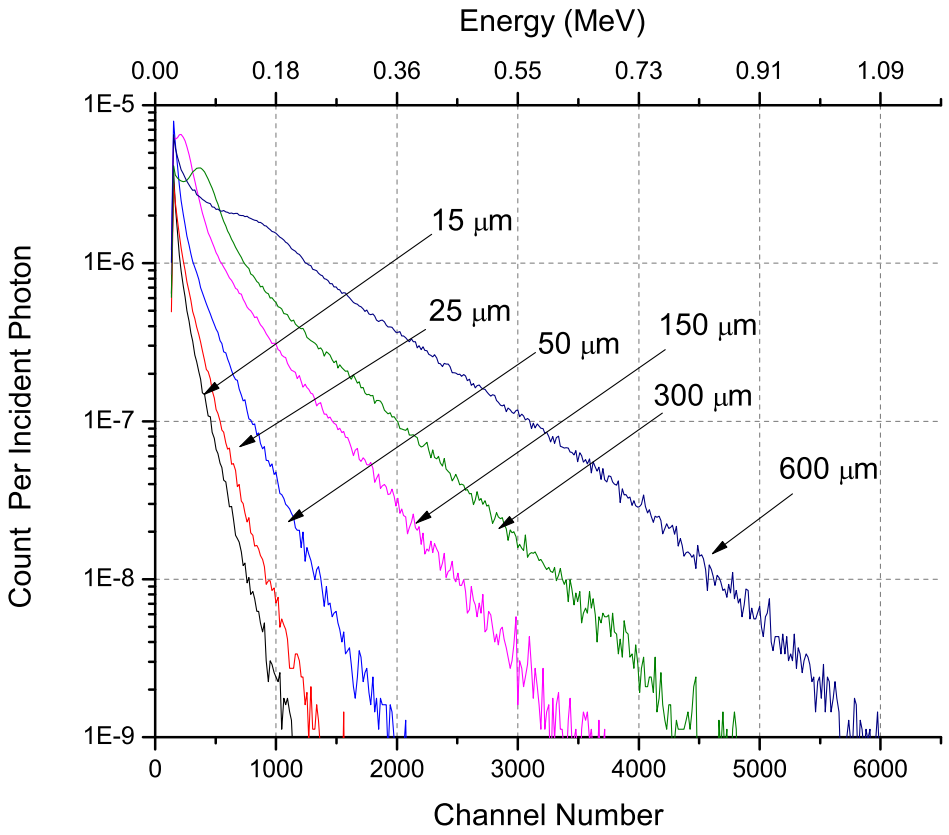

Figure 3.6: Comparison of the energy deposition and binned pulse height spectra for 10% loaded polystyrene from a ^{60}Co source. The simulated and measured spectra have the same shape, indicating agreement. The fabricated films greater than 600 µm were of poor optical quality and therefore their results are not shown.

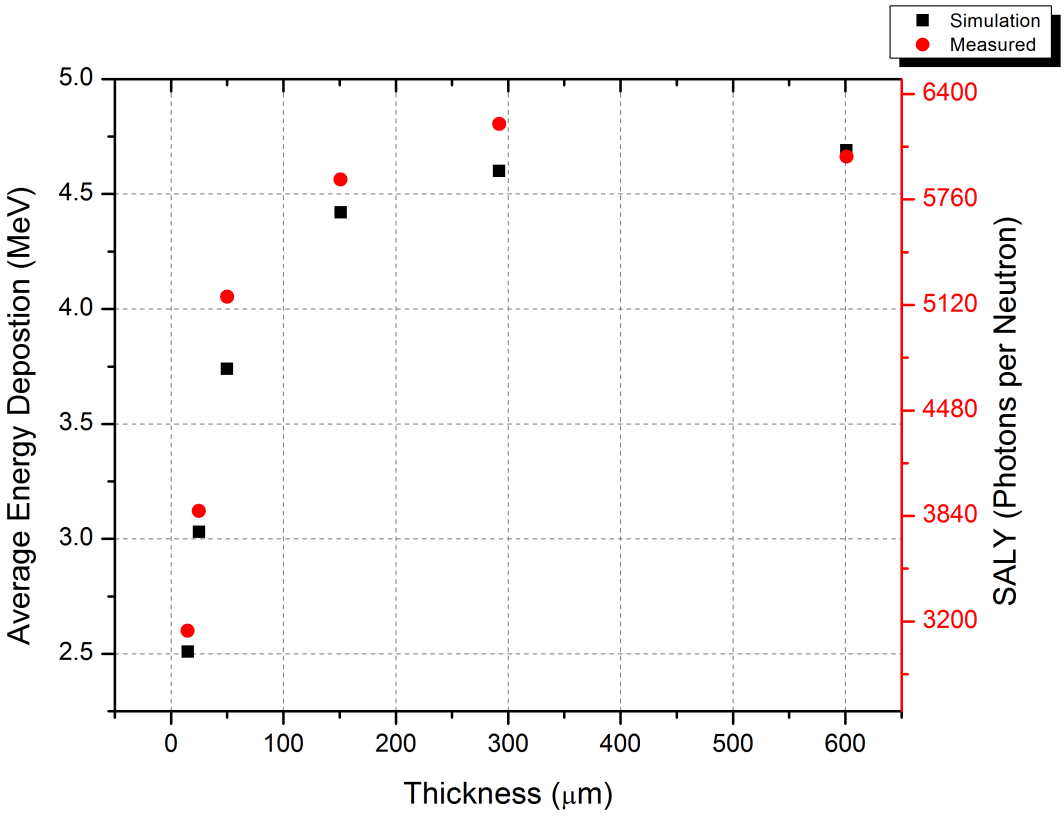

Figure 3.7: Average energy deposition and measured light yield for neutron interactions in 10% loaded polystyrene. The solid lines are calculated values and the red dots are measurements. The incident particle for the simulation is a neutron of energy 0.025 eV, while the measured is the response of thermal neutron spectrum measured from the Cf-252 irradiator. The reaction products depositing the energy are an alpha and a triton.

interaction is 4.78 MeV, which is approached after 200 µm in both the measurement and simulations. This asymptotic behavior is not observed for the gamma spectra.

3.2.2 Optical Photon Simulations

Photons are considered to be optical photons in the GEANT4 model when the wavelength of the photon is much greater than atomic spacing allowing for their wave-like nature. Optical photons were simulated in GEANT4 by creating an optical

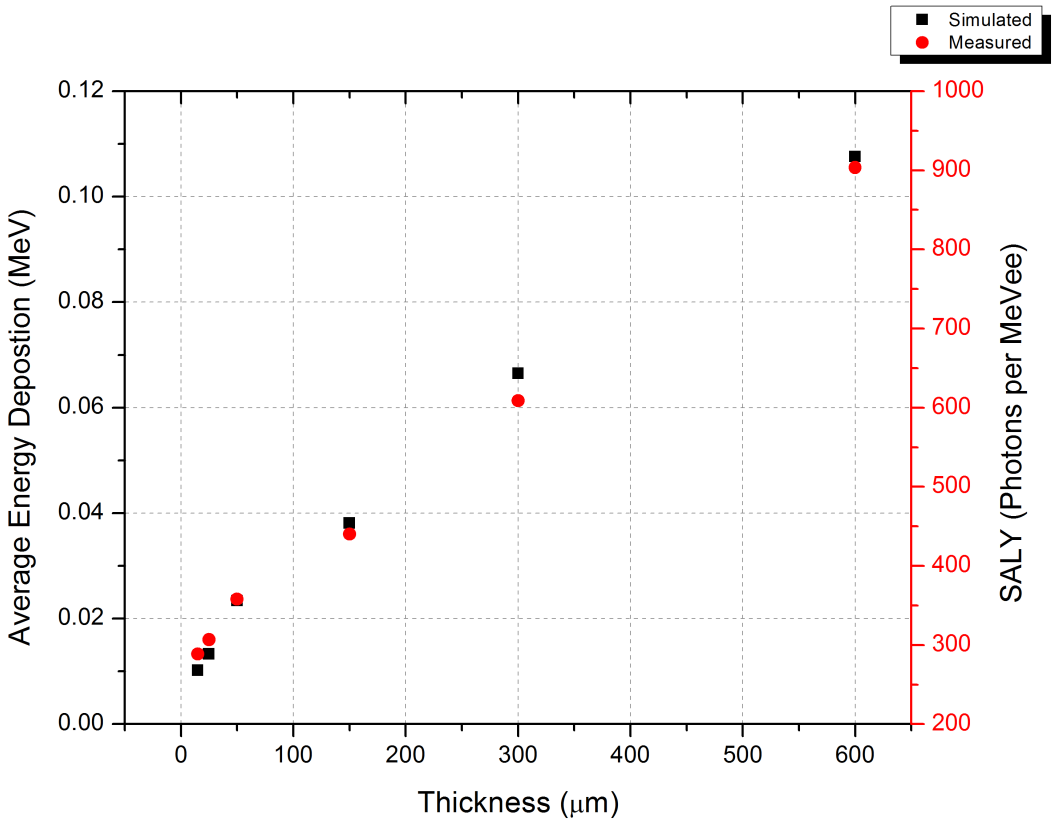

Figure 3.8: Average energy deposition and measured light yield for ^{60}Co interactions in 10% loaded polystyrene. The solid lines are calculated values and the red dots are measurements. The maximum amount of energy that could be deposited by a ^{60}Co photon is 1.33 MeV.

material property table for each of the optical materials. In general this involves setting the scintillation yield of the material, the resolution of the material, the optical photon absorbance of the film, the decay time, and the Birks parameter of the material to simulate the light quenching of the material. Scattering at the boundary between two surfaces can be handled by the UNIFIED model for Optical Surfaces, by the use of look up tables based on the measured data values [Janecek and Moses, 2010], or simply based on the index on Snell's law. For this work a look up table model was employed. More details on the GEANT4 simulations involving light transport can be found in subsection C.3.3.

3.2.3 Optical Photon Yield

The GEANT4 optical photon model was verified by measuring a detector and then simulating a similar detector in the GEANT4 toolkit. The comparison of the simulated entire detection mechanisms (including the energy deposition, scintillation, and optical photon collection) to the a measured value provides confidence in the entire model; however, it should be noted that a validation of this type could allow for individual errors to miraculously cancel each other out. Two cases where considered for the validation: 1) a sample mounted onto a PMT and 2) fabricated layered detectors that where 10 cm by 15 cm by 6 cm . The single sample mounted on the PMT was used to establish the Birks constant for the material and the light yield (see subsection C.3.3), and the fabricated layered detectors measurements were used to provide confidence of the ability to simulate a large scale detector system.

A single sample mounted on a PMT provides a simple geometry to validate the parameters used in the light transport simulations. The geometry consist of a sample mounted with a thin layer of optical grease to the PMT, and the entire assembly is wrapped with teflon grease, as shown in Figure 3.9. This mimics the measurement of a sample mounted on a PMT, expect for the efficiency of the photocathode is not

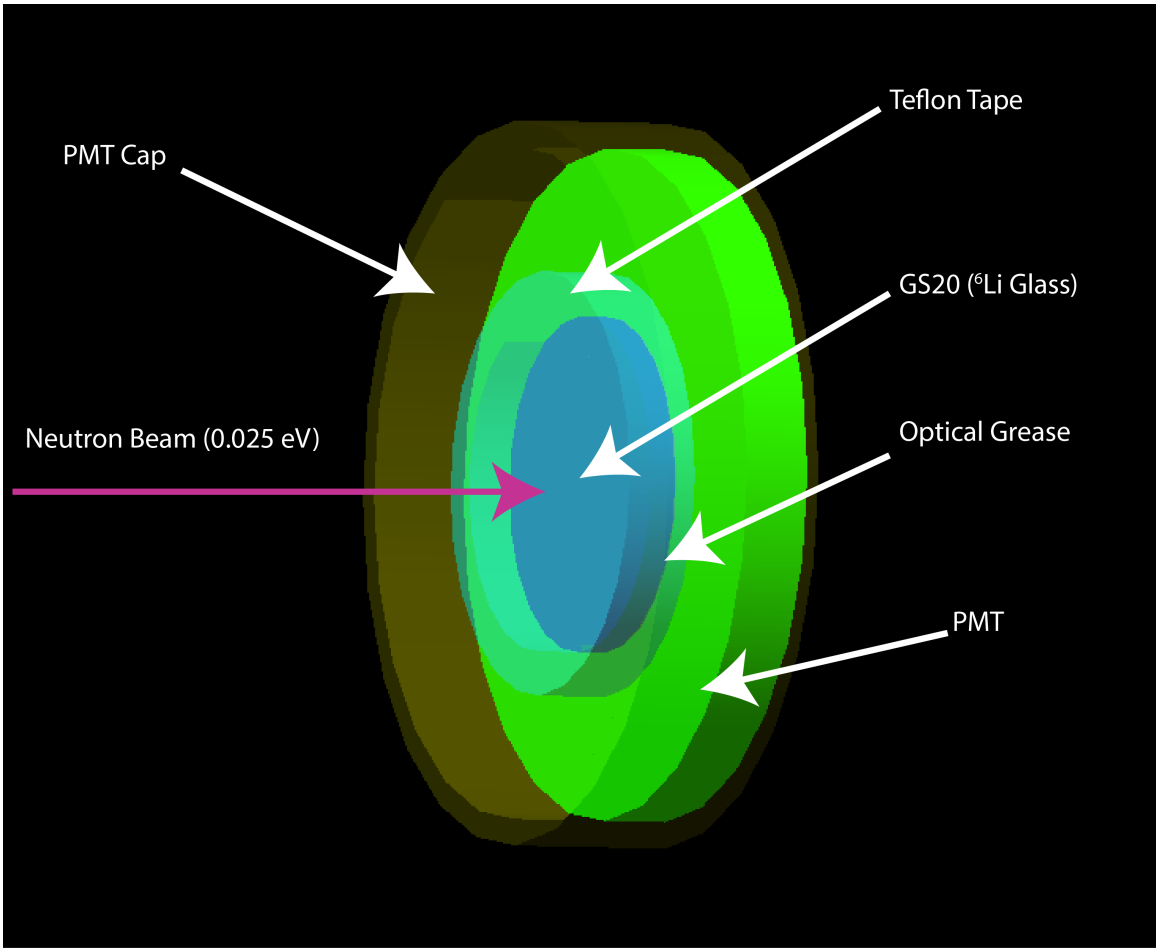

Figure 3.9: Simulated detector geometries for the single detector light collection validation. The two detector materials used in the study are GS20 and ten percent ^{6}LiF polystyrene.

considered. The simulated neutron and gamma optical photon spectra for GS20 and polystyrene based film are shown in Figure 3.10 and Figure 3.11.

The large scale transport of optical photons with the different boundary processes simulation was validated by measuring four assemblies of 10.16 cm by 15.24 cm scintillators with an attached fishtail light guide. Two of the samples where a 10% loaded ^{6}LiF polystyrene cast to 50 µm and 100 µm, while the other samples were a 100 µm ^{6}LiF loaded ZnS:Ag (purchased from Eljen, EJ-426) and a recast carborane sample from South Carolina State University. The PMMA slabs and light guide were

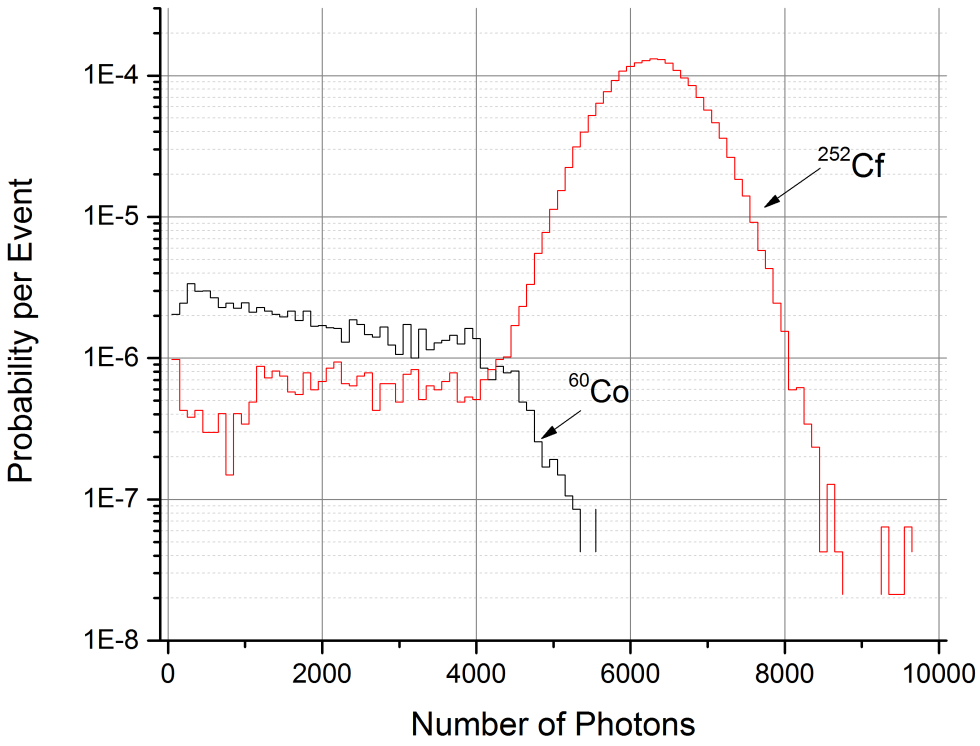

Figure 3.10: Simulated Gamma and Neutron Optical Photon Distribution in GS20. The simulation is described in more detail in section F.6.

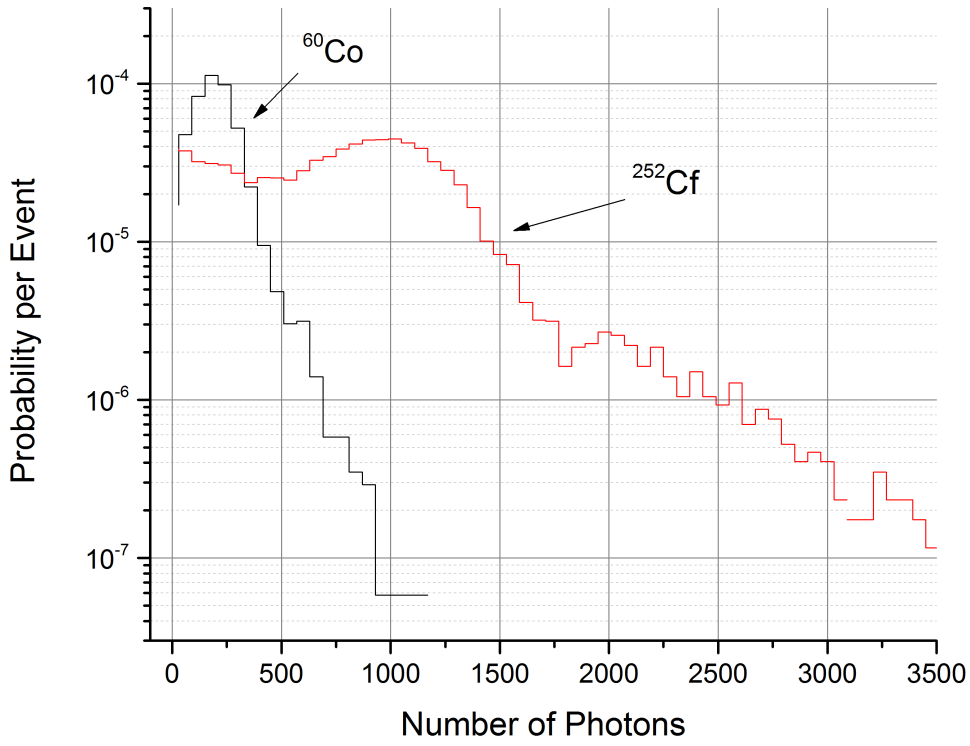

Figure 3.11: Simulated Gamma and Neutron Optical Photon Distribution for a polystyrene film. The simulation is described in more detail in section F.6.

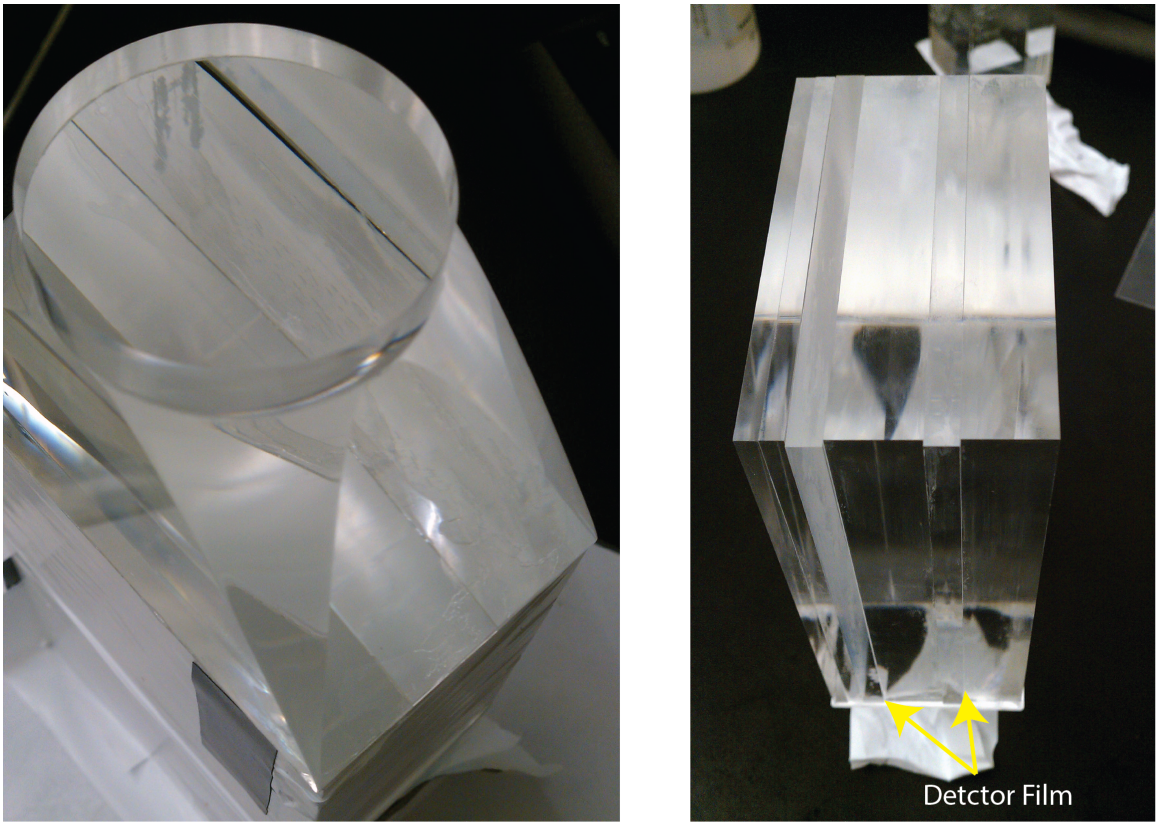

a) Fishtail light guide mounted on samples b) Sandwhiched layers

Figure 3.12: Image of the light guide and the layered PMMA slices between cast ^{6}LiF loaded polystyrene detectors.

also purchased from Eljen Technologies. The slabs and scintillators were mounted together with optical grease, as shown in Figure 3.12 and Figure 3.13.

The agreement between the simulated number of optical photons and the measured number of optical photons detected is shown in Table 3.2, with the measured collected spectra shown in Figure 3.14. The number of optical photons measured was calibrated by measuring the sample of pure material attached directly to the PMT, and simulating the efficiency of collecting the photons in that geometry. There are several factors effecting the agreement between the simulation and measurement. The optical coupling of the simulation was assumed to be perfect without air bubbles, which is not consistent with reality, as demonstrated in Figure 3.13. The opacity of the films were estimated

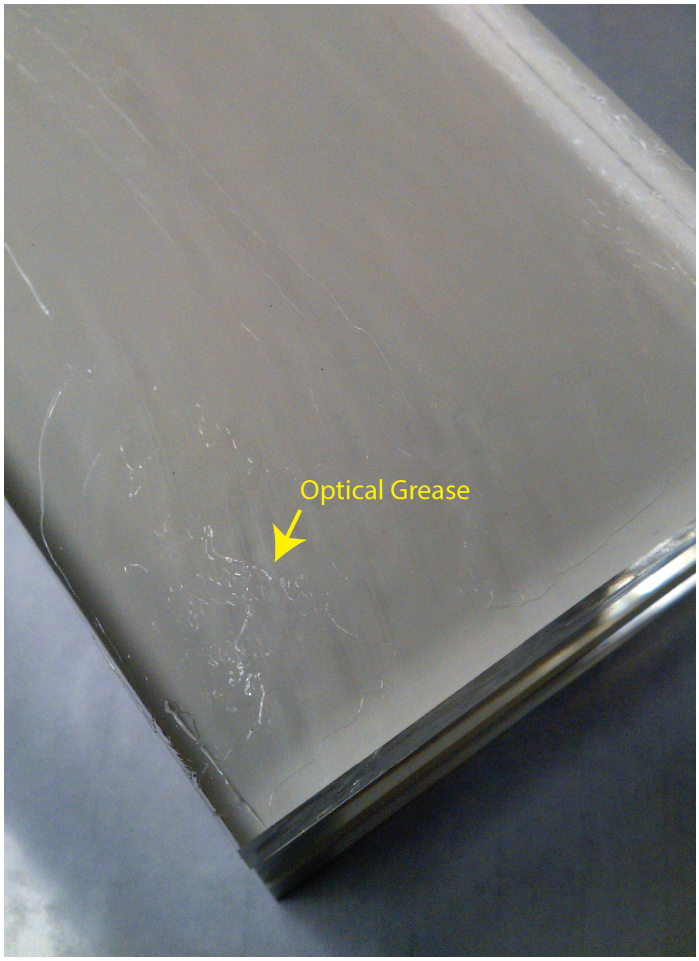

Figure 3.13: Image of the optical mounting of the detector slabs to the PMMA. The detector material shown in this sample is EJ-426 (LiF loaded ZnS:Ag) and is opaque. In the case of the EJ-426 optical grease was only applied to the back face of the detector material per the manufactures instructions.

Table 3.2: Agreement between the simulated light collection in the 4" by 6" detector assemblies and the measurements.

Sample	Measured Photons Collected	Simulated Photons Collected
EJ-426	1, 500	2,100
PS LiF, 50 µm	220	260
PS LiF, 100 µm	100	130

from their absorbance profiles, which depends on how the sample was mounted in the measurement. Finally, and probably contributing the largest to the discrepancies, no attempt was made to fine tune the material parameters for the optical grease and teflon than that which was available as an example in the GEANT4 toolkit.

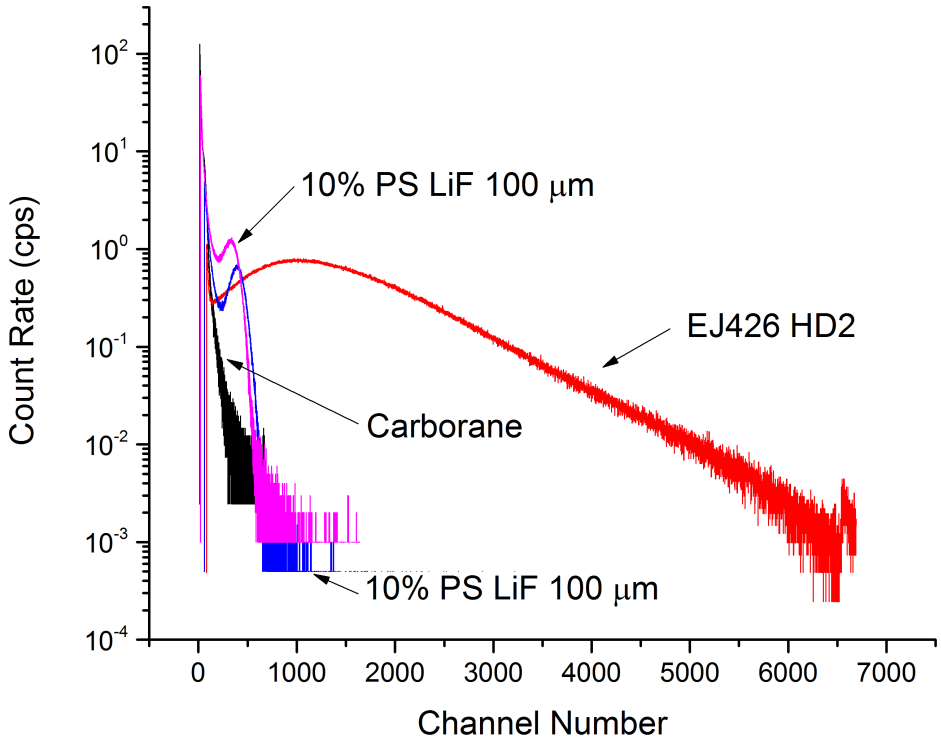

Figure 3.14: Measured light yield of the 4" by 6" detector assemblies. The response of the ZnS:Ag doped with ^{6}LiF (EJ-426 HD2) dominates the response. The effect of a doubling the thickness of the polystyrene films is observed in the higher count rate of the 100 µm film with a slightly lower light yield than the 50 µm film.

3.3 MCNPX Modeling

The performance of films is simulated in MCNPX, a Monte Carlo transport code[Pelowitz, 2006]. The geometry is as in the PNNL reports, namely a nanogram of ^{252}Cf encased in 0.5 cm of lead and 2.5 cm of HDPE. The size of the RPM8 is 12.7 cm deep, by 30 cm wide and 2 m tall. The interaction rate, I_{sim} provides the total number of simulated neutron interactions in the detector and is calculated using the a cell flux tally in MCNPX and a tally multiplier card. The reaction rate $^{6}\text{Li}\,(\text{n},\text{t})\,\alpha$ can be calculated by then applying the appropriate input for the FMn card and using an F4 card to calculate $\phi(E)$. This is in accordance with the direct evaluation of the PNNL criteria, which require a absolute neutron count rate of 2.5 count/s/ng^{252}Cf. Note that in this calculation the source strength is set to be 1 ng ^{252}Cf, which has a neutron emission rate of 2.3×10^{3} neutron/s.

$$I_{\text{sim}} = S_0 I \tag{3.2}$$

$$= 2.3 \times 10^{3}\,\text{neutron/s} I \tag{3.3}$$

However, not all of these interactions will lead to counts above the pulse height discriminator setting necessary for meeting the gamma intrinsic efficiency. This is corrected for by scaling I_{sim} by the fraction of counts, η, that occur above the gamma LLD (3.4), (3.5).

$$\eta \equiv \frac{\int_{MLLD}^{\infty} p(x)dx}{\int_{0}^{\infty} p(x)dx} \tag{3.4}$$

$$\text{Count Rate} = I_{\text{sim}}\eta \tag{3.5}$$

The MCNPX model was benched marked for characterized samples in the in house ^{252}Cf neutron irradiator by simulating the interaction rate and comparing it to the

Table 3.3: Comparison between simulated neutron interaction rate and measured count rate. It is expected that some of the uncertainity in the fabricated samples comes from not knowing exactly the amount of ^{6}Li in the film, as it is determined before casting or pressing.

Sample	Simulated Interaction Rate	Measured Count Rate	Relative Error
GS20	424	428	0.7%
PS 30% LiF 50 µm	56	51	9.5%
PS 30% LiF 25 µm	108	96	13%
PEN, 10% LiF, 110 µm	75.1	70	7%
EJ426 HD2	226	224	0.8%

Table 3.4: Comparison between simulated dose rate and measured dose rate.

Measured		Simulated	
Distance	Dose Rate	Distance	Dose Rate
10.2 cm	10 mRem /h	10.2 cm	10.3 mRem /h
13 cm	5.5 mRem /h	12.8 cm	5.4 mRem /h
28 cm	2 mRem /h	28 cm	1.8 mRem /h

measured count rate. These results are summarized in Table 3.3. It should be noted that the interaction rate is not directly the count rate as an interaction needs to have its scintillation photons collected in order to be a count. One would then expect the simulated interaction rate to be a few percent higher than the measured count rate. In addition the polymeric sample composition is determined before pressing or casting providing a means for the uncertainty of the composition. The relative error is defined as $(sim - obs)/obs)$.

The gamma irradiator fluence was calibrated by measuring the dose rate are various positions, and then simulating the dose rate in MCNPX. The results of this study are shown in Table 3.4, and in general good agreement is observed between the simulation and the measurement. In some cases where the simulated dose rate is higher may be due to uncertainty in the exact location of the probe in the measurement.

3.4 XSDRN Modeling

The XSDRN model was a simplified model of the RPM along an axis through the midpoint of the RPM. A S_n of 16 was used for the quadrature, and convergence for the flux was set at 1×10^{-7} for the inner iterations. Only two types of materials were simulated in the XSDRN calculation; a detector material containing the ^{6}LiF and a moderating material of polystyrene. A 44 group neutron cross sections of each of these materials were processed using NITWAL [Greene et al., 2011a] (without any resonance regions) assuming an infinite, homogeneous medium for simplicity. The XSDRN model consisted of a multi-group isotropic boundary source on the left most boundary on the RPM, with the values for this flux calculated by an MCNPX simulation. A MCNPX calculation was used to determine the neutron flux incident upon the left most side of the RPM, and then this flux was input as the surface boundary flux condition in XSDRN. The number of neutron absorptions was calculated using an activity flag in the XSDRN model. The fitness function for this model was implemented as the activity normalized the number of detector layers. The number of layers was chosen as the normalization factor instead of the actual mass of absorber to allow for different film compositions to be simulated more readily.

The comparison between the MCNPX simulation and the XSDRN is shown for some of the samples in Table 3.5 and Table 3.6, where the change in rank is computed by rank of the MCNPX model versus the rank of the XSDRN model. It is observed that the XSDRN model preformed fairly closely to the MCNPX model, but tended to over predict and favor geometries that had repeated layers and clusters. This was very noticeable when the geometries started with a neutron absorber layer this is attributed to the breakdown of the diffusion equation in a strongly absorbing medium near a source. Some stratification of the results were also observed, leading to the conclusion that the XSDRN calculations should only be used as a general guide. More details are available in the simulation code base, summarized in section F.16.

Table 3.5: 10 Genome Length RPM Model Interactions rates

Genome	Activity	Interaction Rate	Rank Change
0011010000	9.30	3.82	↓ 13
0110100000	10.50	3.81	0
0101010000	10.12	3.79	↓ 7
0101100000		3.79	↓ 1
0011100000	9.63	3.77	↓ 3

Table 3.6: 20 Genome Length RPM Model Interactions rates

Genome	Activity	Interaction Rate	Rank Change
00100101000000000000	7.77	3.79	↓ 19
00011000100000000000		3.78	
00011000010000000000		3.76	
00110001000000000000		3.69	↓ 15
01011010010000000000	23.46	3.66	↑ 1

3.5 Genetic Algorithm Optimization

Genetic algorithms provide a search technique analogous to biological evolution in which instead of searching from general to specific solutions, or from more simple to complex, genetic algorithms generate solutions by mutating and combining parts of the best previously known solutions. At each step in the search for the best solution a collection of solutions called the current *population* is refined by replacing members with solutions representing the offspring of the best individuals. The goals is then to find the best solution to the problem as determined by some criteria, called the *fitness function*. The genetic algorithm typically consist of four tasks: creating an initial population, evaluating that populations fitness, selecting members of the current population to breed, and then applying genetic operators to the selected members to breed the new population. This is completed until either a maximum generation is reached or the desired fitness is achieved, as shown in 3.1.

Algorithm 3.1 Genetic Program Outline

```
while error > goal do
  for all t ∈ F do
    Compute fitness
  end for
  for all t ∈ F do
    Choose individuals based on fitness
  end for
  Select individuals for next population
  Crossover selected individuals
  Mutate selected individual
end while
```

3.5.1 Problem Representation

The thickness of the RPM (12.7 cm) was divided into slices, where each slice could be either a detector slice or a moderator slice. These slices of detector material (represented as a `1`) or moderator material (represented as a `0`) were append into a sequence. This sequence of one's and zero's (or bit string) then completely represented the geometry of the RPM and formed the basis for all possible solutions to the optimization problem. For example the sequence `0001110010` would represent a detector that had three moderator slices, three detector slices, another two moderator slices, and a final detector slice before a single moderator slice as the reflector. Example geometries are shown in subsection 4.2.1. In terms of genetic algorithms the set of all possible solutions is referred to as the *genome*. The length of the genome is thus the number of slices in the geometry, where a higher length genome allows for a more complicated geometry. The initial population for the genetic algorithm was initialized to be random bit strings with equal probability of a slice being a detector slice or moderator.

3.5.2 Population Selection

Several different selection techniques are available to select the individuals from one population to reproduce in the next. Among the most common are fitness proportional selection (roulette selection) and tournament selection. Roulette selection occurs when the individuals are ranked by their fitness, and individuals are chosen by their fitness rank. This is analogous to a roulette wheel where the space a candidate occupies on the wheel is proportional to its fitness. Higher fitness individuals will occupy more space, and will thus have a higher probability of being selected. Tournament selection is another selection technique in which a pool of solutions are chosen at random from the current population. Within this tournament pool a fitness proportional selection will be used to select individuals for the next generation. The fitness function will be explained in detail in subsection 3.5.4.

3.5.3 Genetic Operators

Individuals selected for reproduction are subjected to genetic operators to breed the next generation. Genetic programs generally contain two genetic operators, crossover and mutation. Crossover serves to create new members of the population by interchanging the genetic material of two parents in which significant changes in the solutions are achieved. Mutation serves to slightly modify an existing solution.

Crossover is defined in genetic programming as the swapping of genetic material from one individual to another. For bit strings several crossover operations are commonly used; they are 1) single point crossover, 2) two point crossover, and 3) uniform crossover. An example of the crossover operations are shown in Figure 3.15. In single point crossover a single point is selected on both parents genes and the genetic material between the two parents is swapped. In two point crossover two points are chosen on the parents bit strings and the genetic material is swapped between the intervals. Uniform crossover uses a set mixing ratio for which according to that ratio

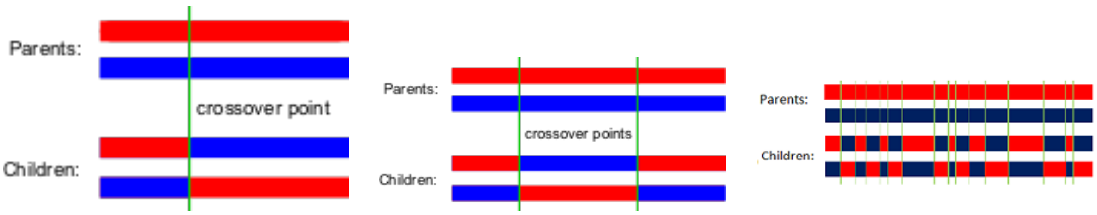

(a) Single Point Crossover (b) Two Point Crossover (c) Uniform Crossover

Figure 3.15: Genetic Crossover Operations. Images from Wikipedia

an individual bit will be interchanged between the two parents to yield the daughters.

Mutation is used to produce small, random changes in the genomes to maintain genetic diversity. The mutation operation was chosen to be a simple bit flip in which a randomly chosen `1` or `0` in the geometry was flipped; for example `001001010` could be mutated to `001001000`. Generally the mutation rate is set very low (less than 2%) in order to prevent the search for the solution to becoming simply a random search. In this representation of the problem a mutation produces a very large change in the solution and the mutation rate was set even lower.

3.5.4 Fitness Function

The fitness function defines the criteria for ranking solutions and probabilistically including them in the next generation. The fitness function was chosen to count rate per mass of ^{6}Li, provided that the geometry meet the total count rate criteria. If it failed to meet the count rate criteria a zero fitness was returned (3.6).

$$f(\vec{x}) = \begin{cases} 0, & \text{if countRate}(\vec{x}) \leq 2.5\,\text{cps/ng}^{252}\text{Cf} \\ \text{countRatePerMass}(\vec{x}), & \text{otherwise} \end{cases} \tag{3.6}$$

Films that have excessive detector layers will be penalized by the normalization by the mass of ^{6}Li that they contain, while favoring films that have the minimum number of

Table 3.7: Bit String Simplified Geometry Descriptions

Genome Length	Slice Thickness	Possible Geometries
5	2.54	31
10	1.2700	1,023
15	0.8467	32,765
20	0.6350	1,048,575
25	0.5080	33,554,431
30	0.4233	1.07×10^9
35	0.3629	3.44×10^{10}
40	0.3175	1.10×10^{12}

detector layers that meet the count rate criteria and have a more effective utilization of the neutron flux which increase their count rate.

At this point it is instructive to make a note about the size of the solution space, highlighted in Table 3.7. For small genome lengths (less than 10) it is possible to exhaustively search the hypothesis space of possible solutions, which is not feasible for the larger genome lengths, as the search space increases as 2^n, while the refinement of the geometry increases linearly. Therefore, efficient evaluation of the fitness function is necessary in order to evolve a reasonable number of solutions, suggesting a deterministic code such as XSDRN. In addition, a hybrid method of finding a basic geometry in a low search space and then preforming perturbations on that geometry will have a better performance than attempting to search the higher geometry solution space.

3.5.5 Convergence

Convergence to an optimal solution of the problem by the genetic algorithm was determined by an exhaustive search of the genome space for lengths less than eight (255 combinations) and using perturbations of the optimal solutions for higher search spaces. For the small search spaces it was observed that the genetic algorithm would converge to an optimal solution almost all of the time; and in the cases when it did not the solution it did converge to was a top candidate. The convergence to the top

candidates can then be corrected by preforming perturbations on the top candidates. A perturbation on a optimal genome is defined as taking each detector slice and translating it a half slice thickness to the left and the right. For example, for a five length genome a perturbation on `010100` would involve first doubling the genome to `001000100000` and then perturbing the slices as `010000100000`, `000100100000`, `001001000000`, and `001000010000`. The perturbations on the length length genome increased the interaction rate from 3.81 interactions per second to 3.85 interactions per second for the optimal ten length genome, and from 3.85 interactions per second to 3.87 interactions per second. Thus, it is determined that the genetic algorithm converged to a very close to optimal solution.

Chapter 4

Results

The basis for setting a pulse height discriminator to differentiate between neutron and gammas can be attributed to the secondary electrons and the difference in energy mechanisms as presented later. However, the application to physical detectors has yet to be concretely formulated. This section will serve to remedy that and present a pulse height discrimination scheme capable of discrimination between neutrons and gammas.

It is currently understood that the light output per path length in the film (which is directly proportional to the pulses collected on the PMT) is related to the stopping power of the radiation in the film material. For a given material the stopping power of the film will be constant, and therefore the light output of the film can be found by integrating the light output per path length over the total length of the film. It is then possible to conclude that the light output of a film is proportional to the energy deposited in the film.

Preferential energy deposition by reaction products from neutron interactions relative to gammas will enhance the discrimination by creating larger neutron light pulses than the gamma pulses, allowing for fewer neutron pulses to be classified as gamma pulses because they are below the MLLD. Thus, neutron-gamma discrimination can be enhanced by optimizing the energy deposition in the film.

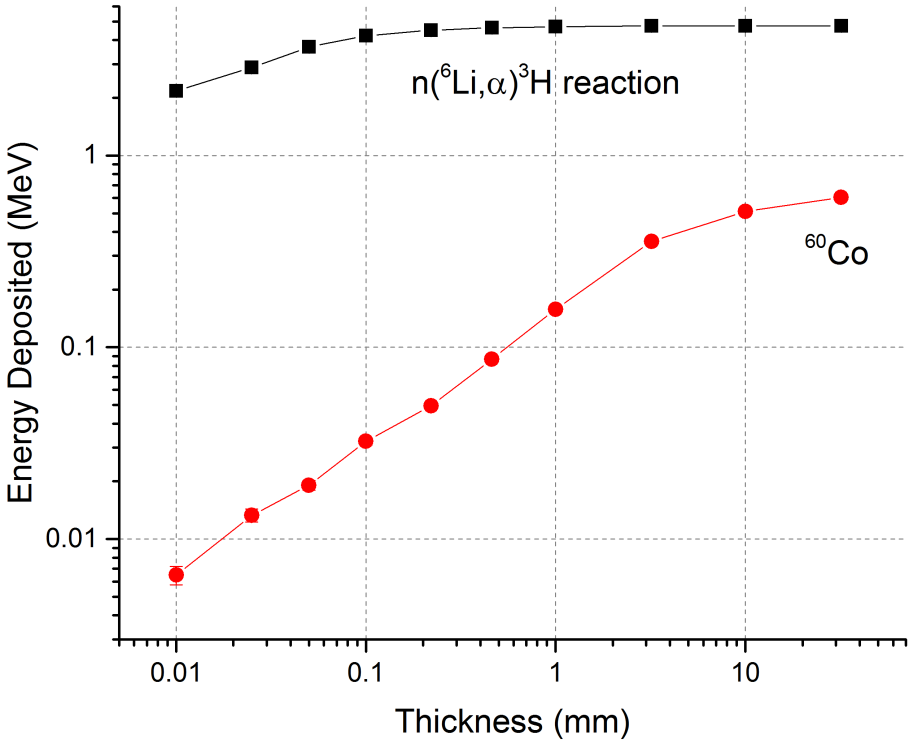

Figure 4.1: Simulated energy deposition and film thickness. As the films get thinner it is very unlikely for gamma events (and their secondary electrons) to deposition all of their energy, while above 50 µm there is very little impact on the energy deposited by neutrons.The simulation is a 10% loaded ^{6}LiF polystyrene. More details of the simulation can be found in section F.5.

4.1 Energy Deposition

The average energy deposited by a neutron and gamma reaction was investigated for different film thickness to determine if an optimal thickness exits in a geometry similar to Figure 3.3. Figure 4.1 shows that the energy deposition of the gamma quickly falls off as the films get thinner, while it isn't until the neutron films become on the order of the range of the triton that the energy deposition is impacted.

Interactions that occur near the edge of the film may have a large impact in the energy absorbed in the film for very thin films where a large fraction of the volume is within a mean free path of the surface of the detector material. For example, for a 25 µm film the range of the triton exceeds the thickness of the film. The energy loss of interactions occurring near the edge of the film was investigated by simulating the energy loss for a large planar detector where the beam spot is 3 mm and the area of the detector face is 10 cm. The geometry for this simulation shown in Figure 3.3, with the interaction position defined to be distance to the first interaction of the beam in the material along the direction of the beam. Figure 4.2 examines the impact of where the interaction took place in the film on the energy deposition. It is observed that for neutrons events that take place within the center of the films tend to deposit a large majority of their energy in the film, while events that occur on the edge of the film have partial energy depositions in accordance with the ranges of the charged particles. The Compton edge is observed at 1 MeV in the simulated photon energy deposition for the 1 cm film, as expected. A secondary effect in having a backing material is also observed for photons in which there is a heightened energy deposition for interactions that occur in the film but near the boundary and electrons are back scattered into the detector material.

Figure 4.3 illustrates the simulated kinetic energy of secondary electrons from Compton scattering and from alpha and triton interactions. It is observed that kinetic energy of the secondary electrons from the neutron reaction products have predominately energies in the kilo-volt range, while the Compton scattering electrons have energies in hundreds of kilo-volts range. However, it should be noted that there is only one secondary electron from a Compton scattering and multiple secondary electrons from the reaction products. The kinetic energy distribution is broken down by the two reaction products in Figure 4.4, while the relative number of secondary electrons is shown in Figure 4.5. It is apparent that the triton contributes more secondary electrons than heavier alpha, while they have similar energies of the secondary electrons.

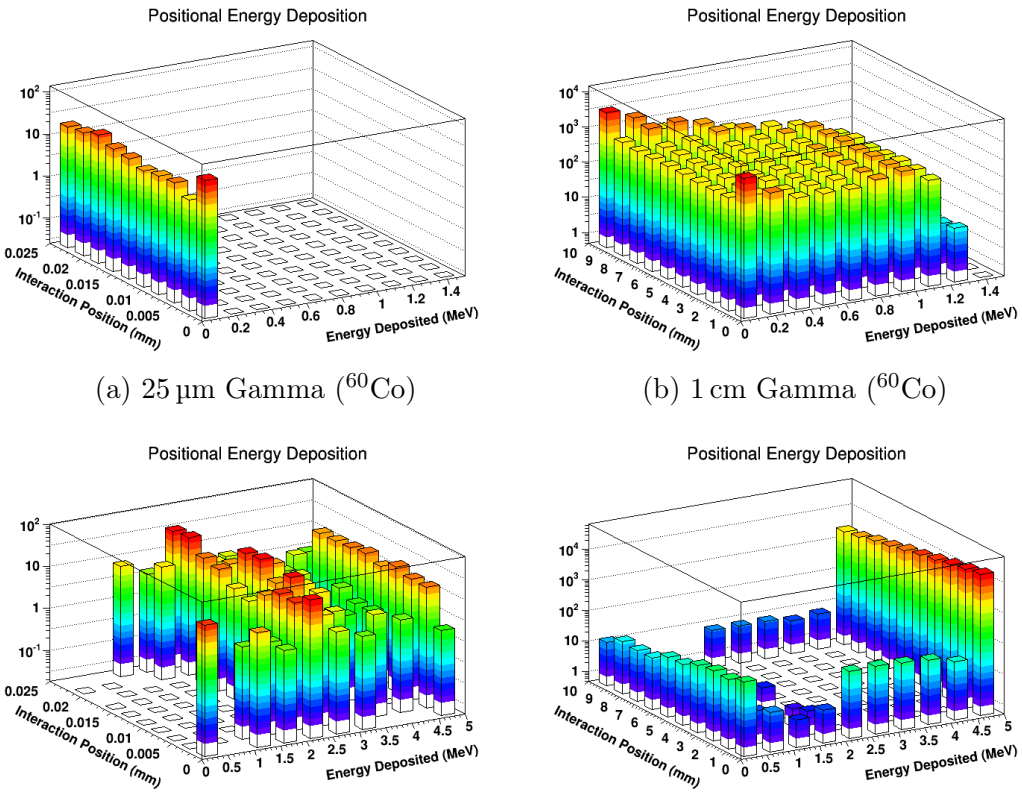

(a) 25 µm Gamma (^{60}Co)

(b) 1 cm Gamma (^{60}Co)

(c) 25 µm Neutron

(d) 1 cm Neutron

Figure 4.2: Simulated average energy depositions and the position of the first interactions. The beam is considered to be incident on position 0, and thus interactions that occur on the front of the film have a much higher probability depositing all of their energy. Events that occur on the edge of the film much less likely to deposit all of their available energy.

The average energy deposited was computed for each thickness and normalized by the incident energy for gammas by the Q-value of the reaction for neutrons, and is presented in Table 4.1. For thickness greater than 150 µm there is little benefit in increasing the thickness of the film in terms of energy deposition by neutrons, since over 90% of the energy is being deposited in the film. The energy deposition and light yield were also investigated by simulations in the GEANT4 environment for polystyrene based films. These simulations (summarized in Figure 4.7) show that as expected the light output was linear with the energy deposition. The importance of

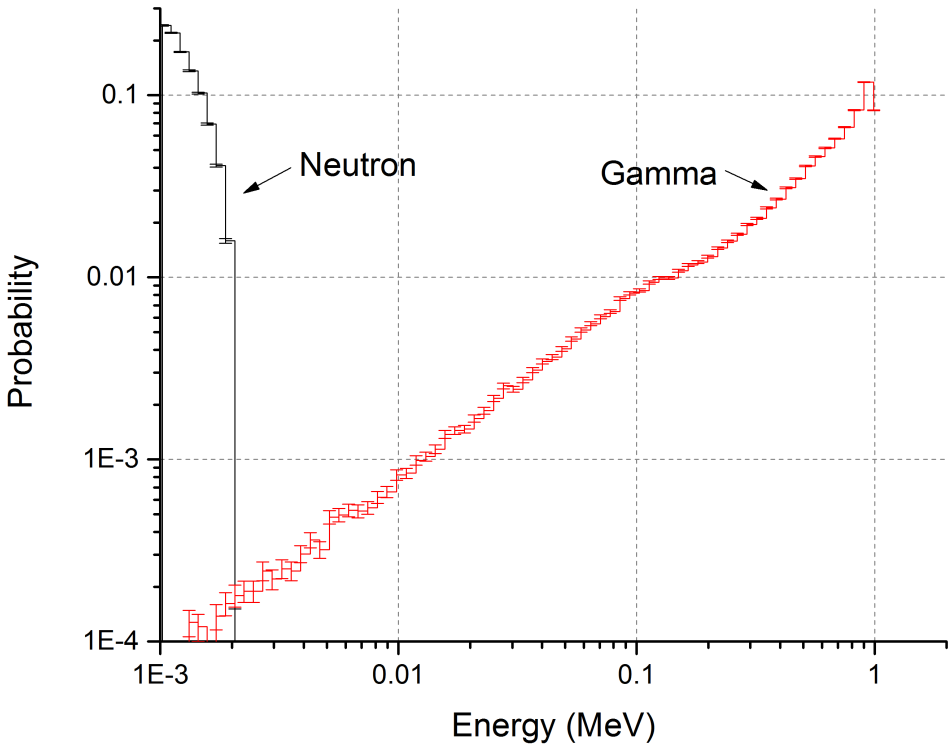

Figure 4.3: The kinetic energy of the first secondary electron from Compton scattering with ^{60}Co and from ^{6}Li reaction products. The energy distribution of all of the electrons produced in the interactions is shown in Figure 2.6.The simulation is a 10% loaded ^{6}LiF polystyrene. More details of the simulation can be found in section F.5.

the particles causing the scintillation events is due to the quenching of the light from heavy charged particles. Thus, while the gammas from ^{60}Co deposit less energy than neutrons in a the same thickness of films, the light output is much higher per unit energy deposited. However, it is instructive to look at the distributions of how many photons were created per event. As the films become thicker and more of the triton energy is captured the response of the triton starts to dominate the alpha (Figure 4.8), resulting in the number of photons peaking around 650 photons for this simulated sample. For photons, shown in Figure 4.9, it is observed that the distribution is flat

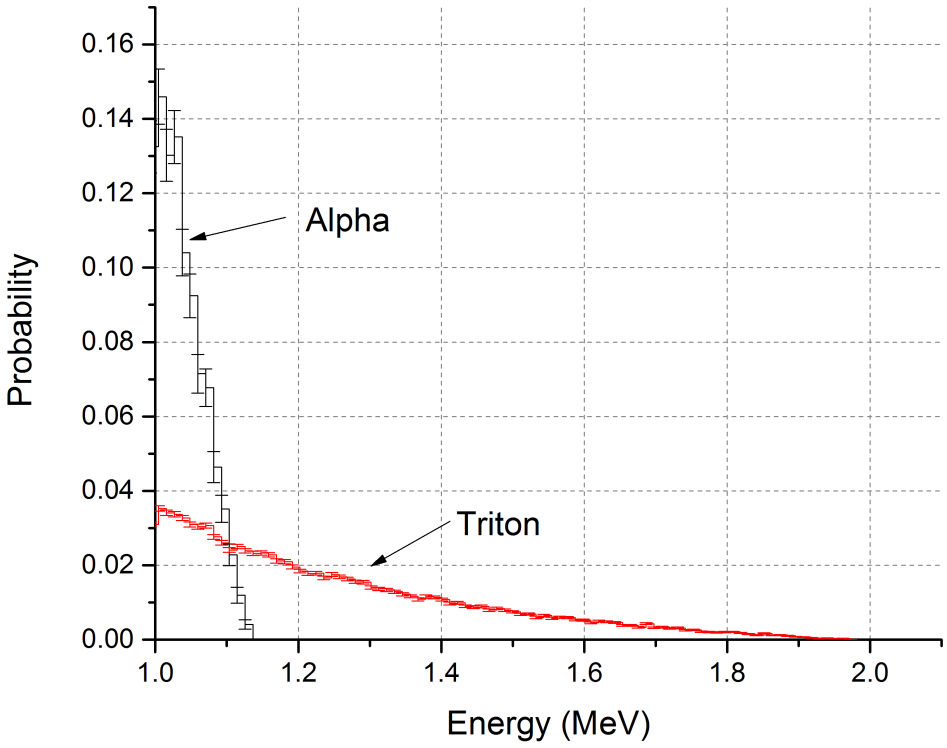

Figure 4.4: Kinetic energy distribution of the first secondary of the neutron reaction products (alpha and triton) from a ^{6}Li interaction. Most of the electrons have kinetic energies in the 1 keV range. The simulation is a 10% loaded ^{6}LiF polystyrene. More details of the simulation can be found in section F.5.

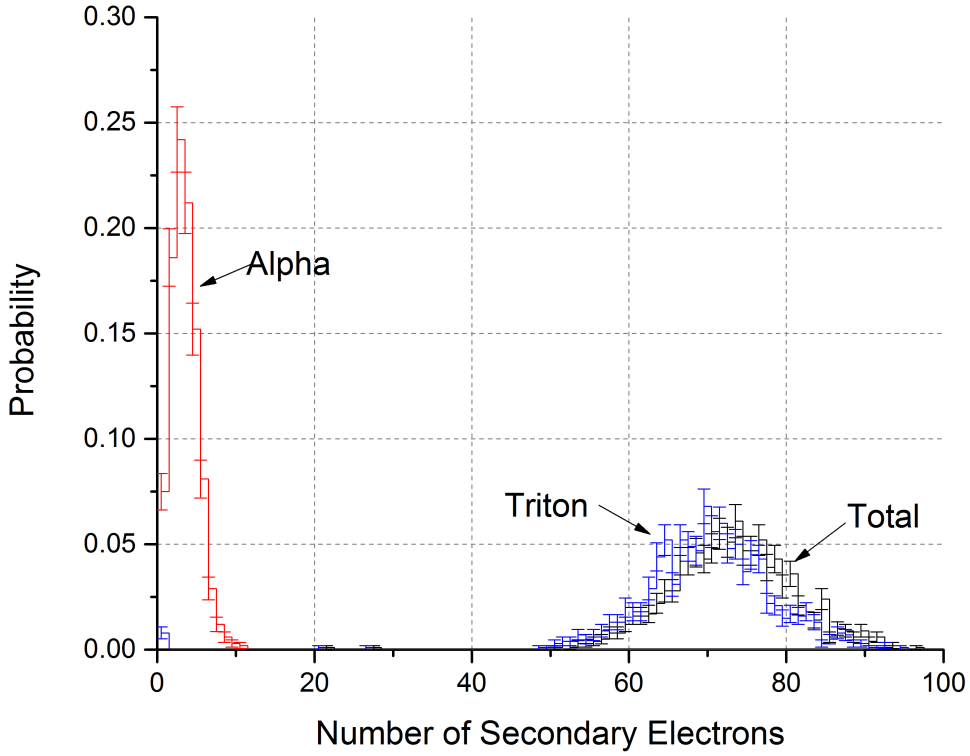

Figure 4.5: Distribution of the Number of Secondary Electrons Produced Per Neutron Interaction. The alpha particle produces almost a factor of 16 less photons than the triton. The simulation is a 10% loaded ^{6}LiF polystyrene. More details of the simulation can be found in section F.5.

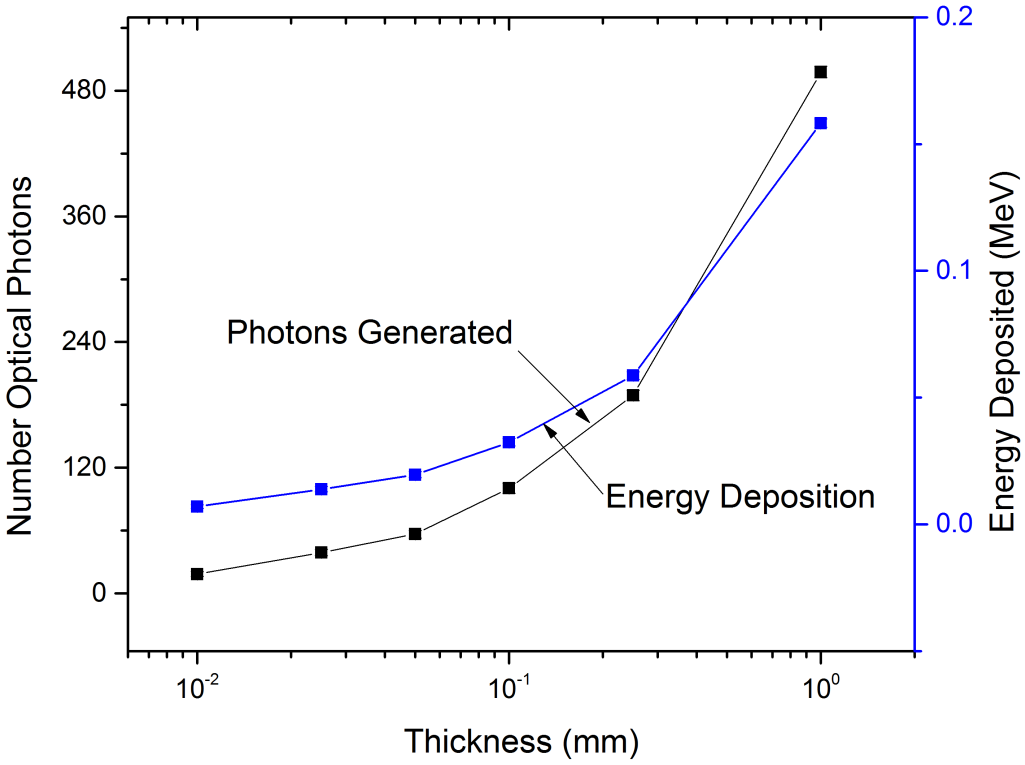

Figure 4.6: Simulated energy deposition from gamma (^{60}Co) and the corresponding simulated light yield. The simulation is a 10% loaded ^{6}LiF polystyrene. More details of the simulation can be found in section F.6.

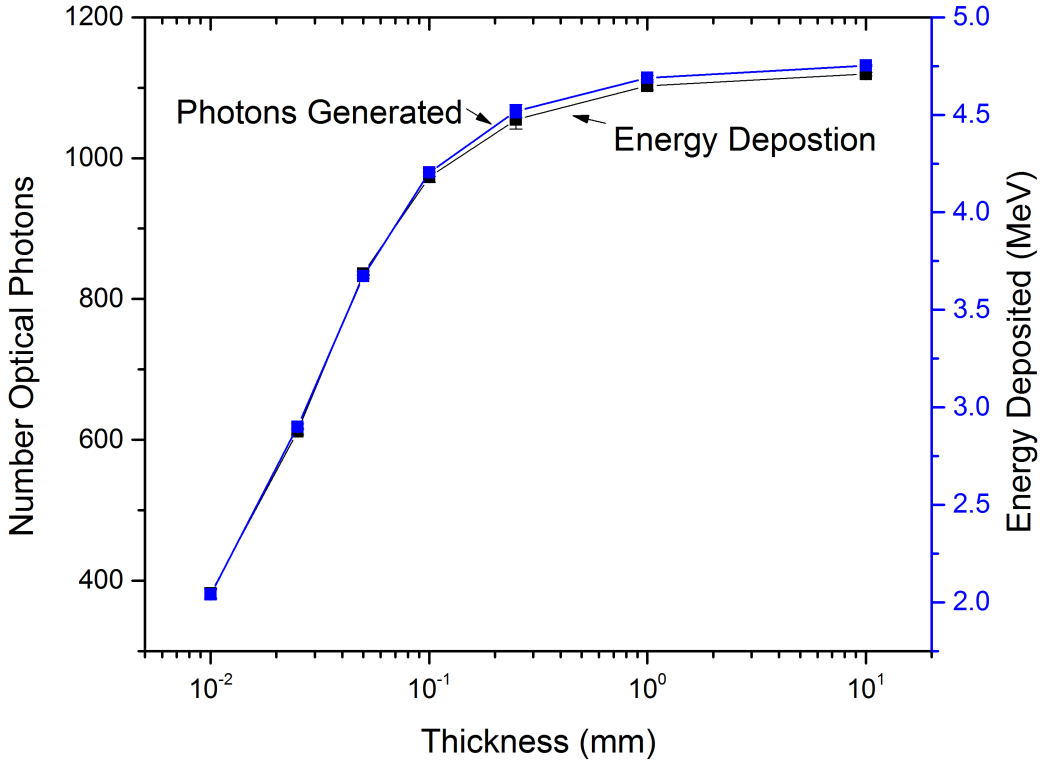

Figure 4.7: Simulated energy deposition and light yield from neutron interactions. The simulation is a 10% loaded ^{6}LiF polystyrene. More details of the simulation can be found in section F.6.

Table 4.1: Fraction of total energy deposited per interaction of a neutron and the photons from ^{60}Co in films of various thickness. The total energy deposited in a neutron event is 4.78 MeV, while the maximum energy deposited from a ^{60}Co is 1.33 MeV.The simulation is a 10% loaded ^{6}LiF polystyrene. More details of the simulation can be found in section F.5.

Thickness	Gamma Fraction	Neutron Fraction
15 µm	0.010	0.531
25 µm	0.013	0.634
50 µm	0.017	0.782
150 µm	0.032	0.927
300 µm	0.052	0.964
600 µm	0.087	0.982
1 mm	0.130	0.989
1 cm	0.425	0.998

for very thick films, but for thinner films the probability is greatly increased for an event to generate a low number of photons.

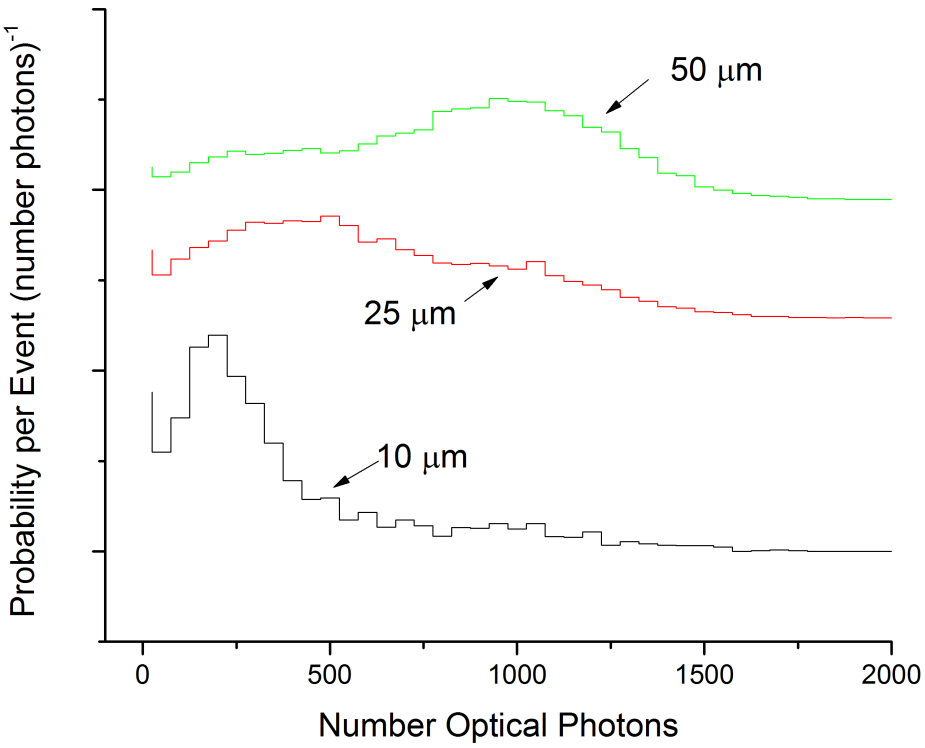

Figure 4.8: Simulated number of photons generated from neutron interactions. For the 10 μm film it is observed that the majority of the photons are generated by a partial energy deposition corresponding to the alpha particle, and this effect tappers off as the films get thicker. The simulation is a 10% loaded ^{6}LiF polystyrene. More details of the simulation can be found in section F.6.

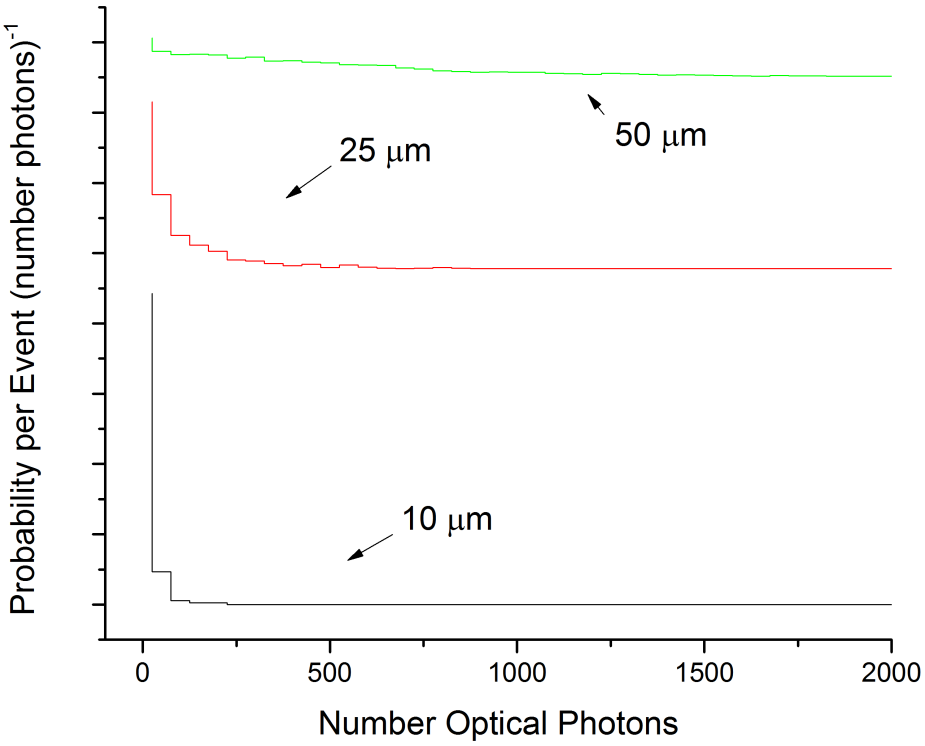

Figure 4.9: Simulated number of photons generated from gamma interactions. Thinner films produce distributions that are skewed towards the left due to having less energy deposition. The simulation is a 10% loaded ^{6}LiF polystyrene. More details of the simulation can be found in section F.6.

4.2 Optimal Detector Designs

The neutron count rate criteria of 2.5 counts per second per nanogram of ^{252}Cf can be used to estimate the size of a detector needed to meet this criteria for various detector efficiencies. If the detector has an intrinsic efficiency of 100%, that is it records every neutron that passes through it as a count, a square of length 23.4 cm would be have sufficient area. A square of length 23.4 cm has an area less than the area of this page. A detector efficiency of 50% would require double the area (or a side length of 33.1 cm), and a detector with efficiency of 1% requires an area of a square of length 73.9 cm. The fabricated polymer films have an intrinsic efficiency on the order of 1×10^{-3}, which requires covering a sphere of radius 2.08 m area to fulfill the count rate criteria, which is not physically available. Alternative usage of the material, such as layering, must then be considered in order to have fulfill the neutron criteria.

There exists a number of different mechanism for which the absolute neutron efficiency of a film can be increased. In the case of the RPM, there are several design parameters that can be explored:

- the neutron absorber loading of the film,
- the thickness of the film,
- the geometry of the film (cylinders or sheets), and
- the placement of the films.

It is expected that the loading of the film will be limited by the optical clarity, and that the thickness of the film will be determined by the optimization of the energy deposition. Thus, of the above design parameters only the geometric placement of the films is an available optimization space.

Preliminary work by this author provided a simple design in which the detector layers are linearly placed throughout the detector volume in an alternating fashion. The analysis of the neutron flux throughout this detector lead to a flat flux profile

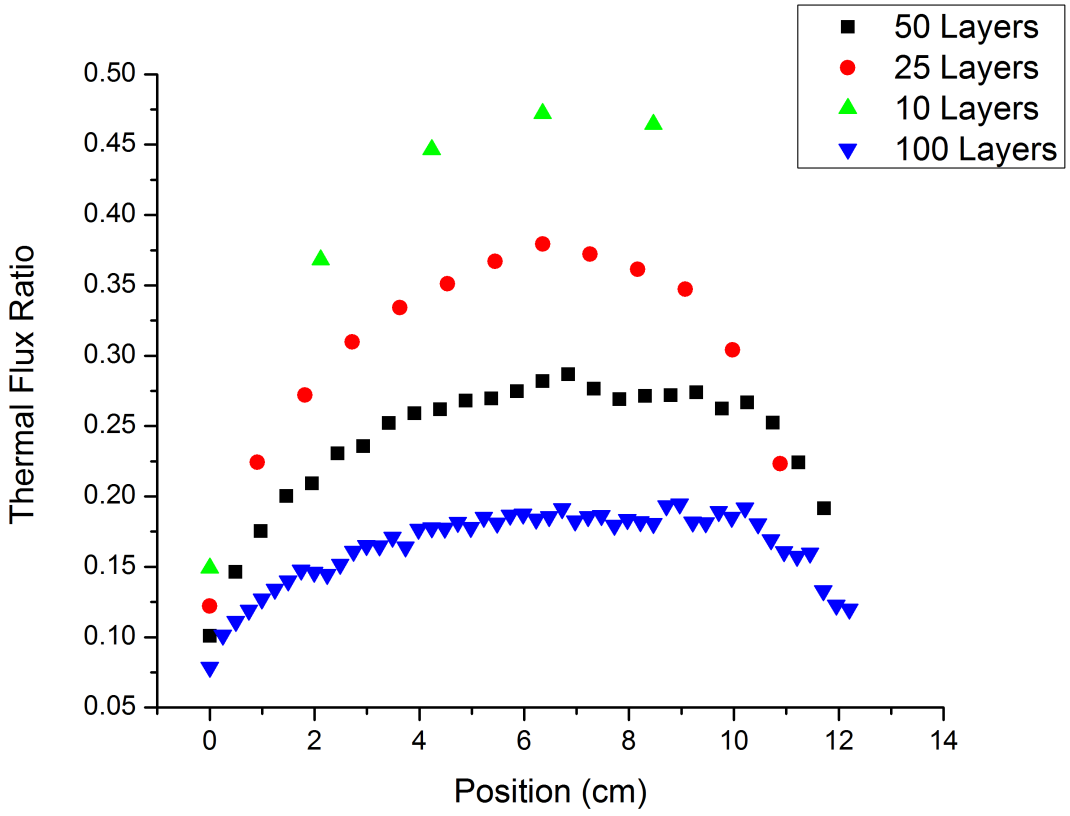

Figure 4.10: Fraction of the neutron flux that is thermalized through a alternating detector and moderator layered RPM. The low thermal fluxes result in a poor utilization of the high thermal cross section of ^{6}Li.

as shown in Figure 4.10. Effective utilization of the neutron flux is necessary for minimizing the amount of neutron absorber (^{6}Li) that is used in the detector.

4.2.1 Optimal Layered Detector Geometries

The optimal genomes are listed for 10 15, 20 length, and 30 length genomes for a minimum interaction rate of 2.5 interactions per second in Table 4.2, 5.0 interactions per neutron per second in Table 4.3, and for 7.5 interactions per second in Table 4.4. It is observed that higher length genomes tended to shows a slight decrease in the total interaction rate while containing the same amount of ^{6}Li. This effect is attributed

Table 4.2: Optimal genome geometries for a total minimum interaction rate of 2.5 interactions per second. The detector and simulation is configured per the PNNL criteria.

Genome	Interaction Rate	Mass ^{6}Li
0011010000	3.82	12.6 g
00100101000000000000	3.79	12.6 g
000101000010000000000000000	3.75	12.6 g

Table 4.3: Optimal genome geometries for a total minimum interaction rate of 5 interactions per second. The detector and simulation is configured per the PNNL criteria.

Genome	Interaction Rate	Mass ^{6}Li
011101001000000	5.31	21.0 g
01011010010000000000	5.21	21.0 g
011001001000010000000000000000	5.06	21.0 g

to the accuracy of the MCNPX calculations. It is also observed (most prominently in Table 4.4) that some geometries have very similar interaction rates. For large interaction rates more ^{6}Li is required, increasing the number detector layers needed. This causes a lower thermal to fast neutron flux ratio, especially towards the middle of the detector. A flat flux profile implies that that positioning of the film layers does not matter as no region has a higher thermal flux than another. In the cases where a lower interaction rate is desired the changes to the film positions can be attributed to the difference that perturbations make on the geometry, and are mostly within the Monte Carlo error.

Table 4.4: Optimal genome geometries for a total minimum interaction rate of 7.5 interactions per second. The detector and simulation is configured per the PNNL criteria.

Genome	Interaction Rate	Mass ^{6}Li
01111101110100001000	7.56	41.2 g
0111110101001010100 0	7.53	41.2 g

The rendering of several of these geometries are shown in Figure 4.11, Figure 4.12, and Figure 4.13 with the genomes written out in Table B.3, Table B.2, and Table B.1.

The neutron flux as it crosses the detector is of interest to examine the utilization of the neutrons. Figure 4.14 shows the flux profiles for an optimal geometry for a 20 length genome with a minimum of 2.5 interactions per second and Figure 4.15 shows the flux profiles for a minimum of 5 interactions per second. It is observed that the fast flux quickly decreases as the there is a build up of the thermal flux. Once the thermal flux has reached about 4×10^{-3} neutrons $/\mathrm{cm}^2/\mathrm{s}$ it is advantageous to place layers of ^{6}Li to reduce the thermal flux. A build up of the thermal flux is observed after the last detector layer, and the thermal flux declines as neutrons leave the detector.

4.2.2 Wrapped Polymer Cylinders

In addition to planar detector sheets a possible replacement geometry could be to wrap the detector sheets around a wavelength shifting light core in concentric cylinders and replace the helium tube directly. MCNPX simulations were completed of geometries containing two, three, and four cylinders of wrapped detector material. It is envisioned that the detector material could be deposited on a flexible sheet and wrapped to create a cylinder, however, for simplicity a concentric cylinder design is simulated. The outer diameter of the cylinders were set to be two inches (2.5 cm) to be a direct replacement of the existing helium three tubes. The exact placement of the helium tubes in an RPM is not known, so the tubes were placed one-third of the way back in the detector material, and spaced equidistance apart. Calculations have shown that when a matrix of tube positions are considered (i.e. varying the x coordinate for all y coordinates, for all possible combinations) that there is little difference when the cylinders are offset. In particular, it is shown in Table 4.5 that the variation of the x coordinate has a negligible effect on the count rate, as long as most of the cylinders are about a third of the way towards the front of the detector. The final spacing of

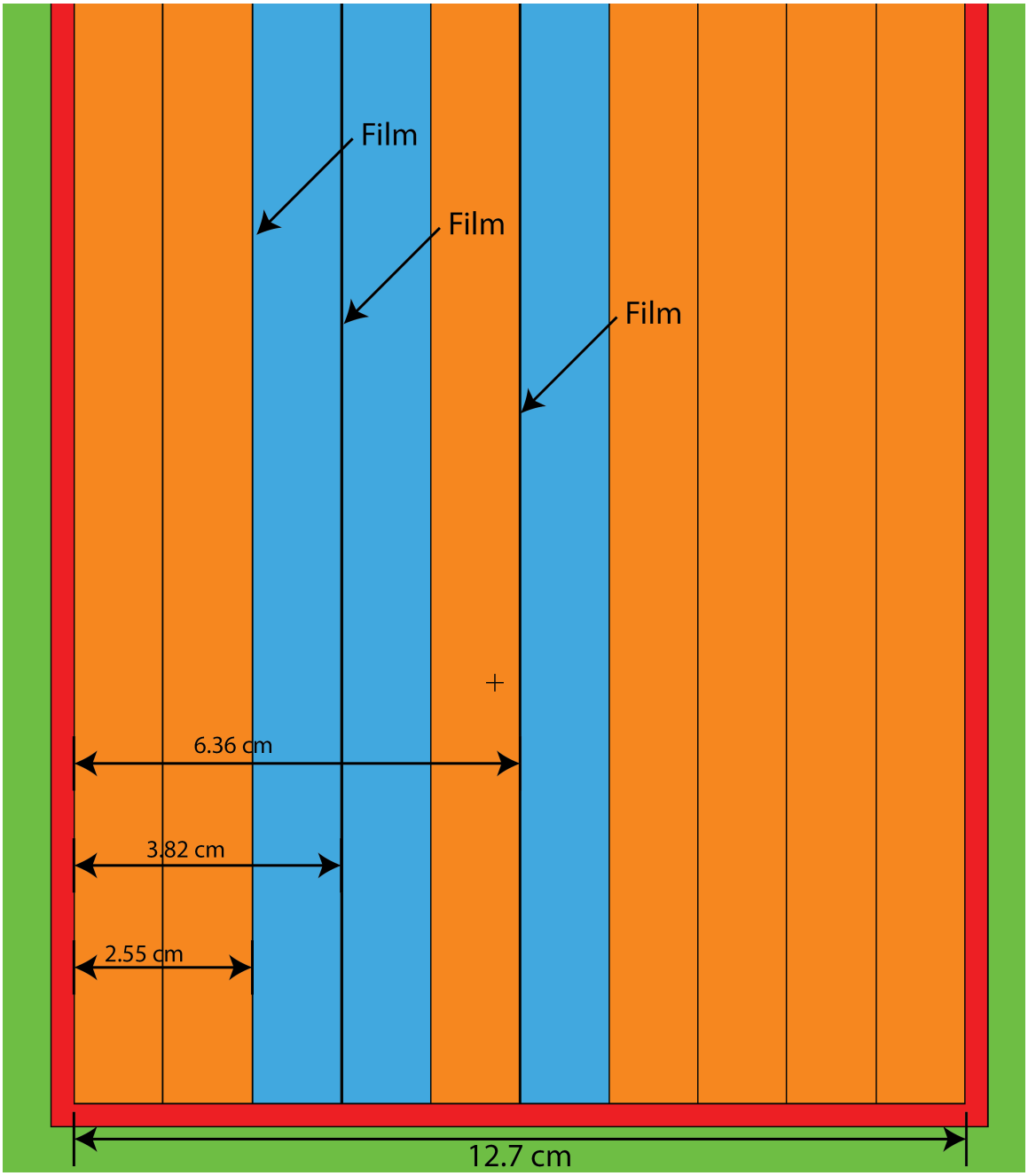

Figure 4.11: Position of 10% ^{6}Li loaded polystyrene films in an RPM8. The minimum count rate achieved in this configuration is 2.5 interactions per second per nanogram ^{252}Cf.

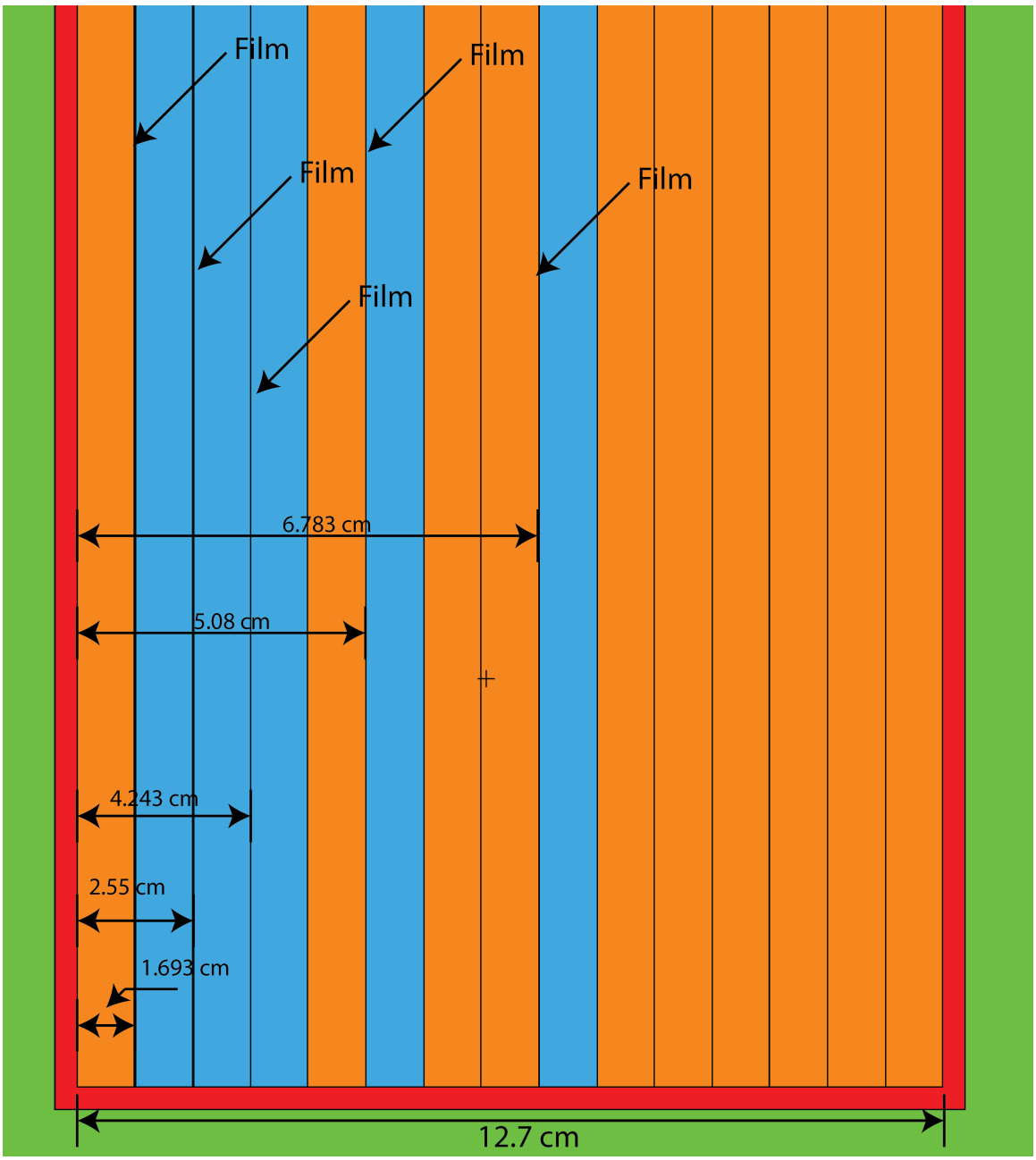

Figure 4.12: Position of 10% ^{6}Li loaded polystyrene films in an RPM8. The minimum count rate achieved in this configuration is 5.0 interactions per second per nanogram ^{252}Cf.

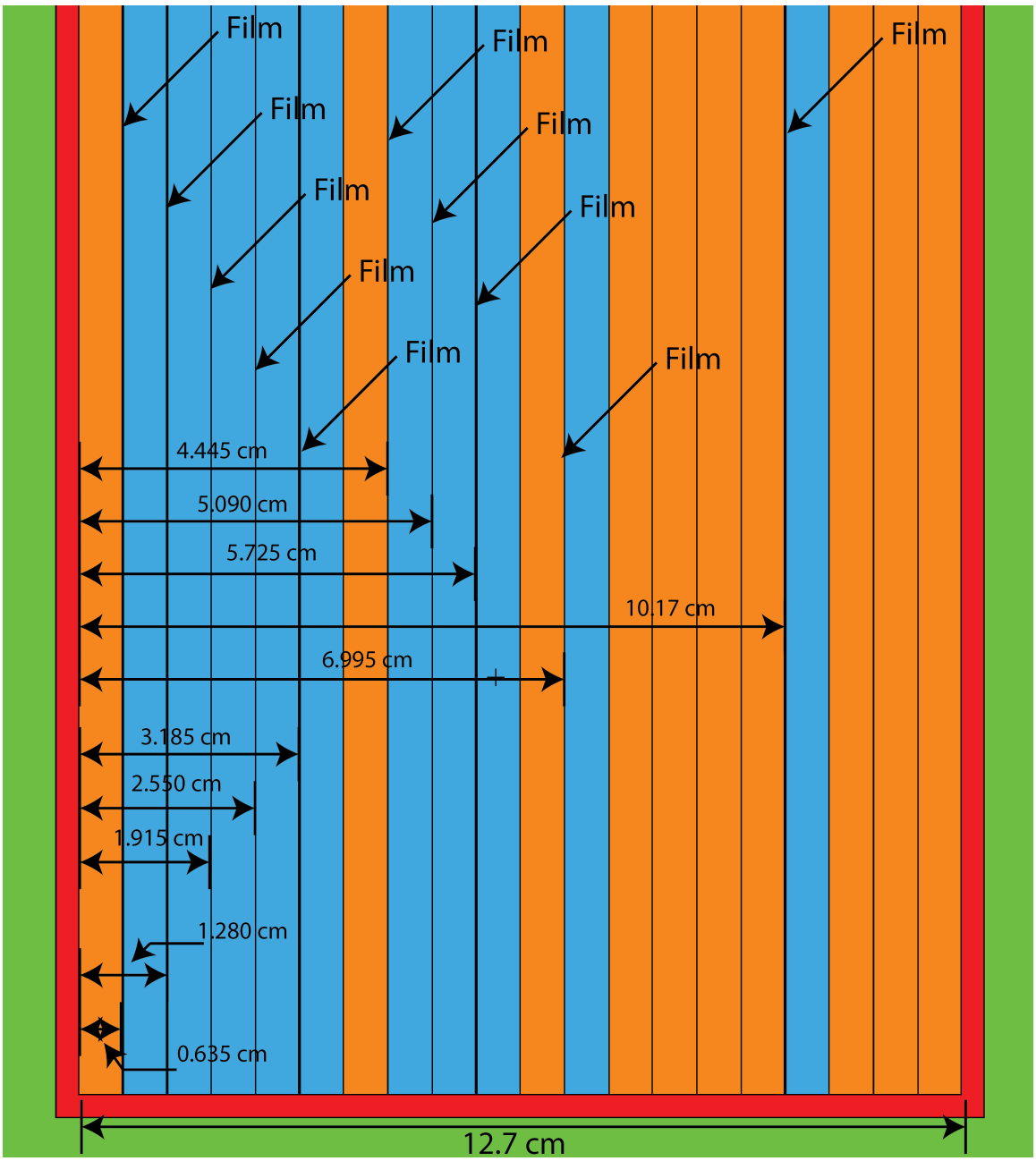

Figure 4.13: Position of 10% ^{6}Li loaded polystyrene films in an RPM8. The minimum count rate achieved in this configuration is 7.5 interactions per second per nanogram ^{252}Cf.

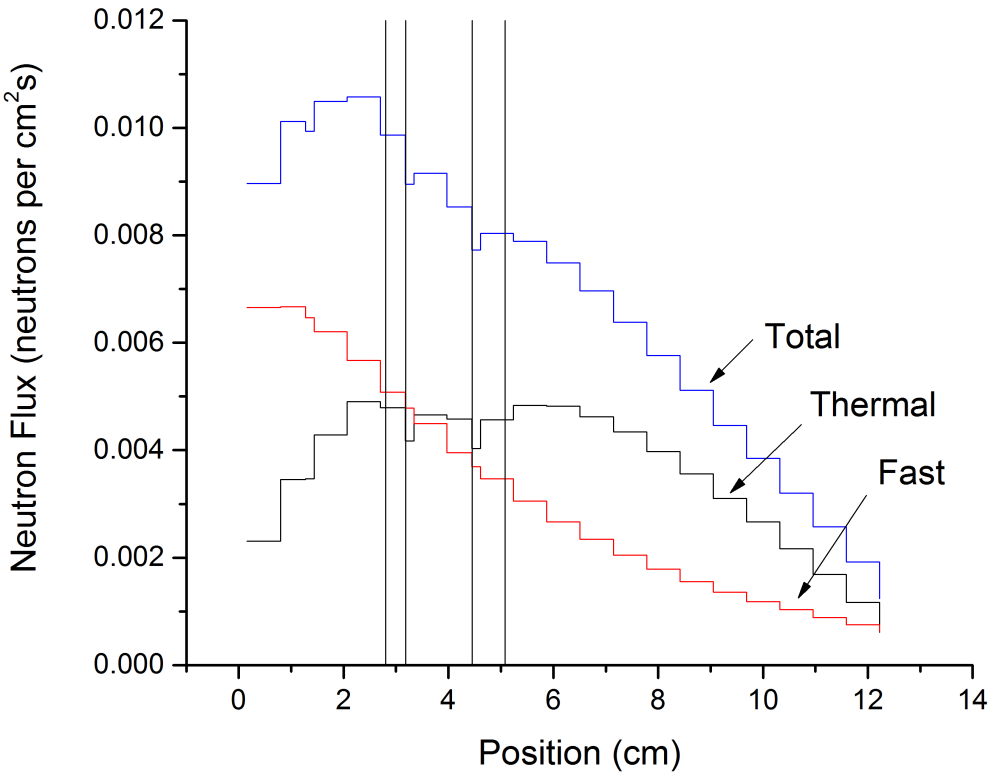

Figure 4.14: Neutron flux profile for a 20 length genome with an interaction rate of 3.82 interactions per neutron. The vertical lines represent detector film layers.

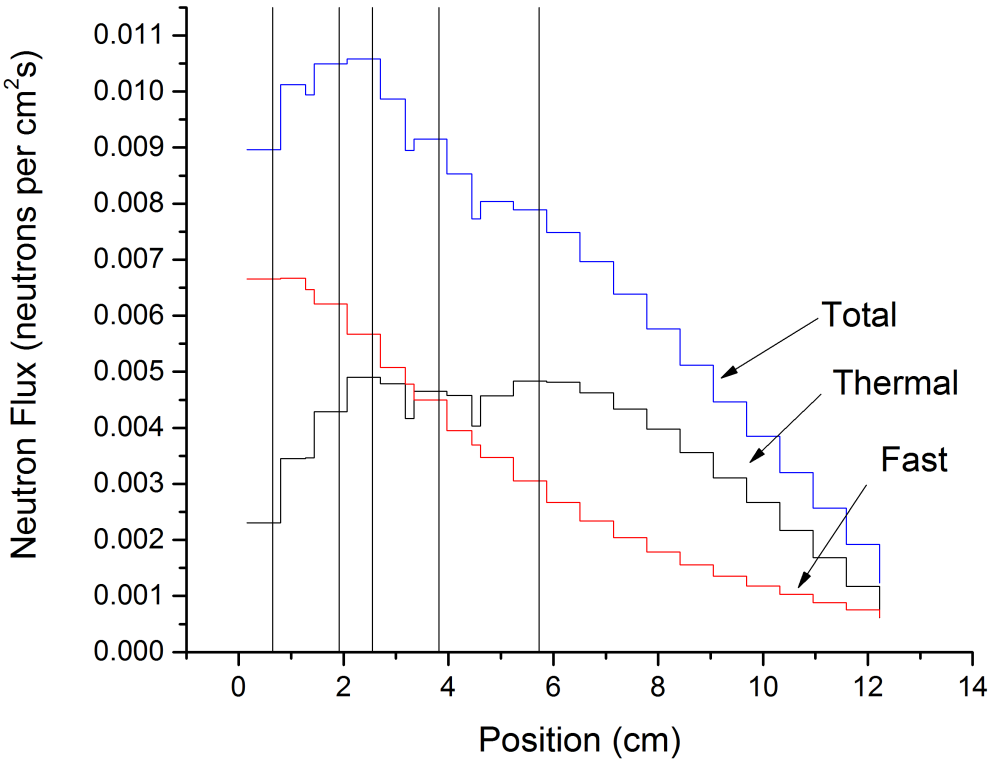

Figure 4.15: Neutron flux profile for a 20 length genome with an interaction rate of 5.31 interactions per neutron. The vertical lines represent detector film layers.

Table 4.5: Effect of the cylinder position on the total neutron interaction rate. The percent changes in the total reactivity are less than the errors of the Monte Carlo uncertainty. The position of the x coordinates are shown, while the y positions are given in Table 4.6.

Cylinder Coordinates	Interaction Rate Change	Cylinder Coordinates	Interaction Rate Change
Three Cylinders		Five Cylinders	
4.0,4.0,4.0	0%	4.0,4.0,4.0,4.0,4.0	0%
4.0,4.0,5.5	1.5%	4.0,4.0,2.5,4.0,4.0	0%
4.0,4.0,2.5	1.5%	4.0,4.0,2.5,5.5,4.0	0.3%
4.0,5.5,4.0	1.5%	4.0,4.0,4.0,5.5,4.0	0.3%
4.4,4.4,4.4	2.0%	4.0,4.0,5.5,4.0,4.0	0.7%
4.4,4.4,2.5	2.5%	4.0,4.0,4.0,2.5,4.0	1.0%
4.0,2.5,4.0	3.4%	4.0,4.0,4.0,5.5,2.5	1.0%
5.5,4.0,4.0	3.4%	4.0,4.0,2.5,4.0,5.5	1.7%
4.0,5.5,2.5	3.9%	4.0,4.0,2.5,5.5,2.5	1.7%

Table 4.6: Positions of the wrapped cylinders in the RPM. The thickness of the RPM corresponds to the x dimension, and the width of the RPM cabinet extends from $-15.25\,\text{cm}$ to $15.25\,\text{cm}$

Number Cylinders	x coordinate	y coordinate
2	4.23 cm	$\pm$ 10.16 cm
3	4.23 cm	0 cm, $\pm$ 7.625 cm
4	4.23 cm	$\pm$ 3.05 cm, $\pm$ 9.15 cm

the tubes inside the radiation portal monitor is described in Table 4.6, and shown in Figure 4.16 and Figure 4.17. The thickness of the RPM (12.7 cm) corresponds to the x dimension, where the front of the detector is at x equals 0.0 cm. The width of the RPM cabinet extends from $-15.25\,\text{cm}$ to $15.25\,\text{cm}$, where a y coordinate of zero is on the midline of the detector width.

Several pertinent design constraints can be learned from the careful study of these results. As observed in the 10% and 20% loading of ^{6}LiF a doubling of the loading does not imply a doubling of the interaction rate for the same geometry. This effect

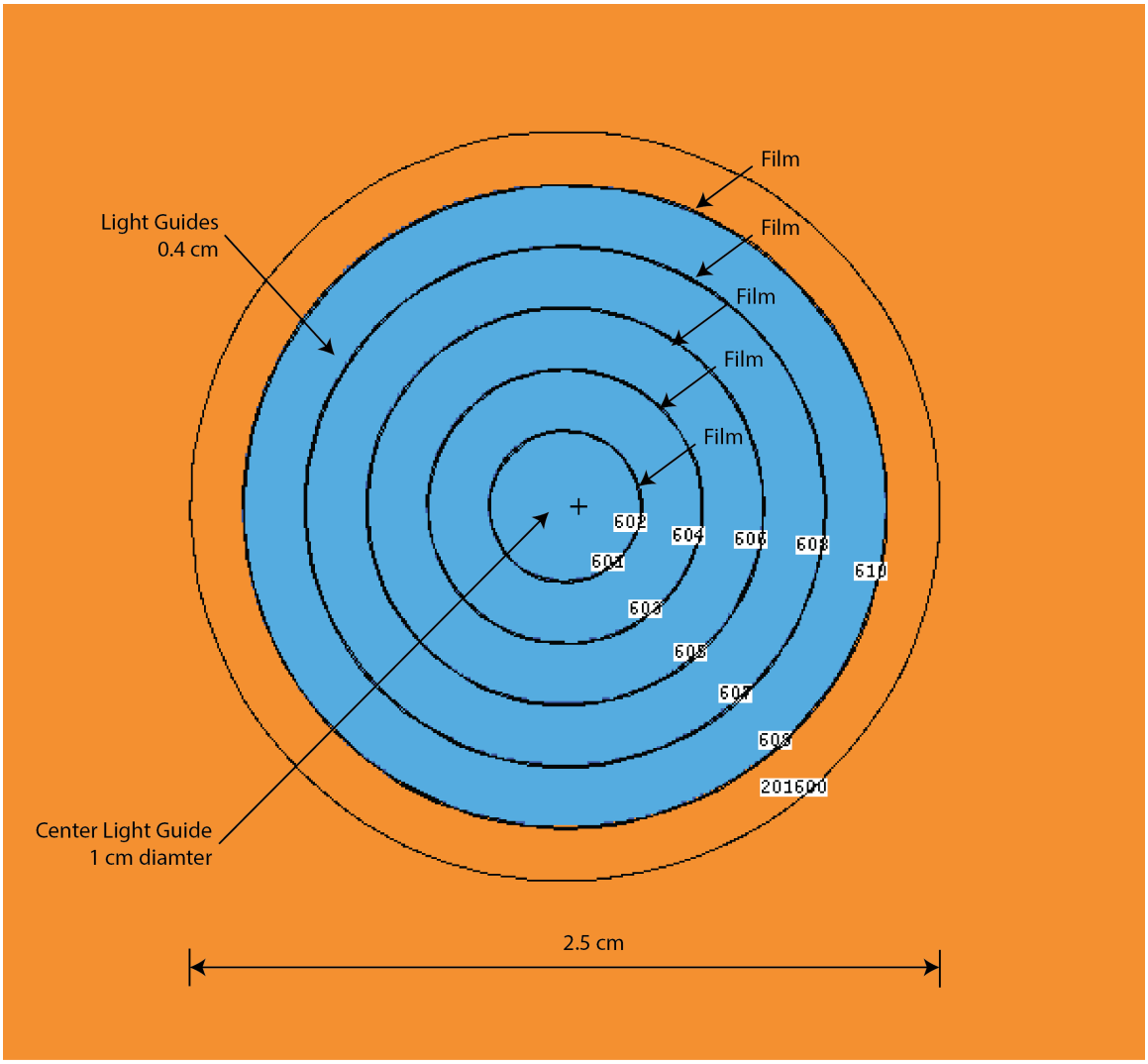

Figure 4.16: MCNPX Rendering of a wrapped cylinder. There is a 1 cm diameter inner light guide surrounded by films separated by 0.4 cm thick light guides.

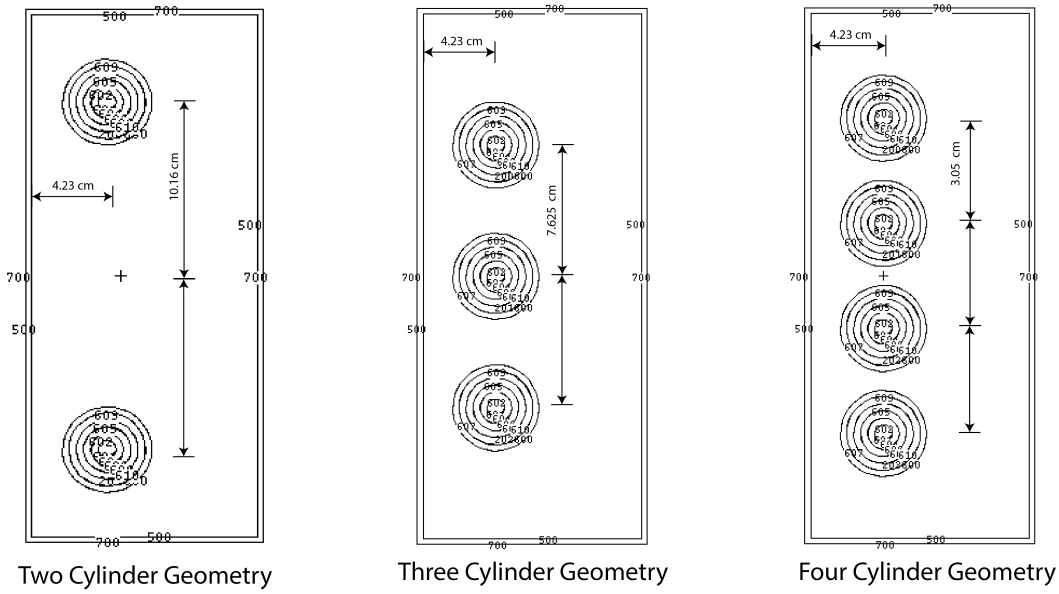

Figure 4.17: MCNPX Rendering of wrapped cylinders placed in an RPM8 Cabinet.

Table 4.7: MCNPX simulated interaction rate of two wrapped cylinders of polymer loaded ^{6}LiF in the RPM8 footprint

Polymer	Fraction ^{6}LiF	Mass ^{6}Li g	Interaction Rate count s^{-1} ng^{-1} ^{255}Cf	Interaction Rate per Mass count/s/ng^{252}Cf/g
PS	0.10	4.80	1.321 ± 0.03	0.28
PS	0.20	9.60	1.852 ± 0.04	0.19
PS	0.30	14.38	2.160 ± 0.04	0.15
PEN	0.10	4.77	1.325 ± 0.03	0.28
PEN	0.20	9.54	1.841 ± 0.04	0.19
PEN	0.30	14.31	2.157 ± 0.04	0.15

Table 4.8: MCNPX simulated interaction rate of three wrapped cylinders of polymer loaded ^{6}LiF in the RPM8 footprint

Polymer	Fraction ^{6}LiF	Mass ^{6}Li g	Interaction Rate count s^{-1} ng^{-1} ^{255}Cf	Interaction Rate per Mass count/s/ng^{252}Cf/g
PS	0.10	7.20	1.482 ± 0.02	0.21
PS	0.20	14.39	2.240 ± 0.03	0.16
PS	0.30	21.58	2.706 ± 0.04	0.13
PEN	0.10	7.15	1.368 ± 0.02	0.19
PEN	0.20	14.31	2.119 ± 0.03	0.15
PEN	0.30	21.46	2.608 ± 0.04	0.12

Table 4.9: MCNPX simulated interaction rate of four wrapped cylinders of polymer loaded ^{6}LiF in the RPM8 footprint

Polymer	Fraction ^{6}LiF	Mass ^{6}Li g	Interaction Rate count s^{-1} ng^{-1} ^{255}Cf	Interaction Rate per Mass count/s/ng^{252}Cf/g
PS	0.10	9.60	1.879 ± 0.03	0.20
PS	0.20	19.19	2.816 ± 0.04	0.15
PS	0.30	28.77	3.360 ± 0.05	0.12
PEN	0.10	9.54	1.726 ± 0.02	0.18
PEN	0.20	19.08	2.668 ± 0.04	0.14
PEN	0.30	28.62	3.234 ± 0.04	0.11

is due to the the flux self-shielding of the outer material layers in which the outer material layer depletes the thermal neutron flux thus making the flux seem harder to the interior layers of the wrapped film assembly. In addition, it can be observed in all cases the the minimal amount of ^{6}Li has the highest count rate per mass, again due to shelf-shielding. None of two wrapped cylinder designs spaced by 0.4 cm would be ability to fulfill the radiation portal monitor neutron count rate criteria, thus a direct replacement of the assemblies is not possible. However, there would be the possibility (if 78% of the events are above the lower level discriminator) to use a 30% loaded PEN or PS film in a four cylinder arrangement as a replacement technology.

To limit the effects of self-shielding the light guide thickness was increased from 0.4 cm to 0.8 cm, and an array of five cylinders (placed at 0 cm, $\pm$5.08 cm and $\pm$10.16 cm) were simulated, the geometry of which is shown in Figure 4.18. The interaction rate for the 30% loaded polystyrene film was 2.92 cps/ng^{252}Cf (2.79 cps/ng^{252}Cf for the 30% loaded PEN) using 21.4 g of ^{6}Li, thus having an interaction rate per mass that is 15% higher than the four cylinder, 30% ^{6}LiF loaded PS wrapped cylinder detector. This indicates that it is more desirable to space out the detector materials than to pack them into a short space.

The five cylinder design (with 0.8 cm spacing between detector film layers) had three layers of detectors in each of the five cylinders. The inner most layer, with an inner radius of 0.5 cm, contained 13% of the mass ^{6}Li, while the second layer contained 33% and the outer layer (inner radius 2.12 cm) contained the majority of the absorber at 54%. The interaction rate of each detector film layer in a cylinder is described for all five cylinders in Table 4.10. It is observed that the outer cylinder (located at $\pm$ 10.16 cm)reaction rates are very similar to the other three, suggesting that the edges effect and the flux depression due to presences of the other cylinders are negligible. In addition, it is observed that when the interaction rate is normalized by the fraction that each cylinder occupies in the assembly there is little difference (beyond the 5% statistical convergence on the tallies) in the reaction rate per unit mass between the layers, thus suggesting a close to optimal material usage is achieved. If it was

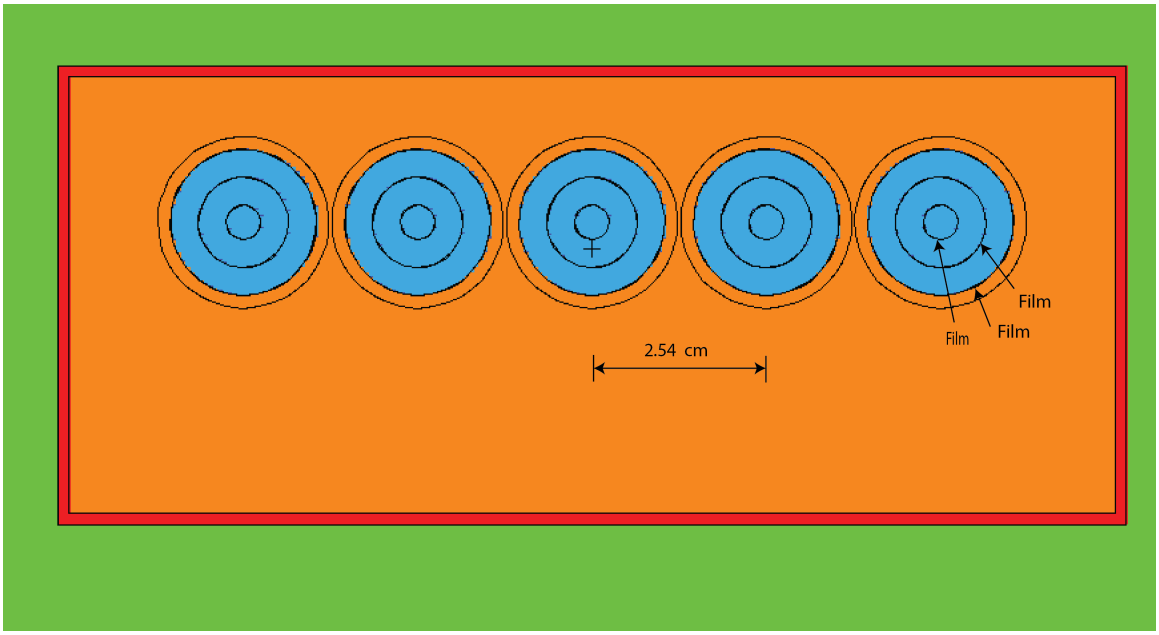

Figure 4.18: MCNPX Rendering of five wrapped cylinders placed in an RPM8 Cabinet. The spacing between the detector layers is 0.8 cm, with the total detector having an interaction rate of 2.92 cps/ng^{255}Cf.

Table 4.10: Simulated Interaction rate (per nanogram ^{252}Cf). The tally convergence was within 5% for all tally values.

Fraction of Assembly	−10.16 cm	−5.08 cm	0 cm	5.08 cm	10.16 cm
0.13	0.072	0.074	0.069	0.070	0.062
0.33	0.180	0.201	0.186	0.189	0.172
0.54	0.318	0.351	0.330	0.338	0.310

necessary, however, to trim material the inner cylinder would be an ideal candidate due to contributing little in the way of total counts. In this design the outer cylinders had over 56% of the total interaction rate, while the innermost cylindrical film layers contributed less than 12% to the total interaction rate.

Table 4.11: Light collection efficiencies of several detector designs simulated by PNNL[Jordan et al., 2003]. The detector is BC-408 (PVT based scintillator) of dimensions 127 cm x 57.15 cm x 5.08 cm.

Number of PMTs	Light Collection Efficiency	
	2-in PMT	5-in PMT
2	7.0%	18.8%
4	13.3%	30.7
6	18.4%	40.2%

4.3 Light Collection

There is no assurance that the detectors designed based on interaction rate would be feasible to construct; due to their low light output and opaqueness collecting the light from scintillation events is extremely difficult. Additional simulation work then needs to be completed to ensure that a RPM in the layered detector design has a realistic method of collecting the light emitted from the scintillation events. Light transport modeling provides a way to calculate the performance of such a design while providing insights for the improvement of a detector design. Several previous authors have used the GEANT4 toolkit to simulate the light collection efficiency of their detector designs. In PNNL 14283 the authors looked at a variety of different PMT placement and detectors designs to increase the light output of a detector in the Advanced Large-Area Plastic Scintillators (ALPS) project [Jordan et al., 2003]. The authors found that for a 127 cm by 57 cm by 5 cm slab of BC-408 (a typical PVT based plastic scintillator) wrapped in a loose foil of 85% reflectivity that the light output could be almost doubled by doubling the number of PMT's. These results are summarized in Table 4.11. For this detector design the number of PMT's was set at two, 2 inch PMTs with the knowledge of adding additional PMTs will increase the light collection.

The choice of cladding around the light guide and detector is essential to optimize the number of optical photons collected. The cladding material must be matched

Table 4.12: The effect of Teflon, mylar, and air cladding on the light collection of a scintillating slab. The simulation is 100 µm thick slice of material 2 m long, 30 cm wide with a rectangular PMT on each end. The photons are born isotropically throughout the material. It should be noted that there is substantial self-absorption in ZnS:Ag, which results in a very small fraction of the photons collected. In practice, however, ZnS:Ag high light output causes it to outperform the other materials.

	Coating	Fraction of Photons Crossing Boundary	Expected Number of Photons Crossing Boundary
EJ-200	Teflon	12%	1,200
	Air	14%	1,400
	Mylar	9.6%	960
PS LiF	Teflon	4.3%	86
	Air	4.5%	90
	Mylar	4.0%	80
EJ-426	Teflon	0.46%	736
	Air	0.45%	720
	Mylar	0.42%	672

for the wavelength of the photons that are being transported as well as the index of refraction of the material, taking into account the bulk absorption of the material and specular or diffusive reflection as the boundaries. A GEANT4 simulation was then completed of a PVT based scintillator, polystyrene loaded with 10% ^{6}LiF scintillator, and ^{6}LiF loaded ZnS:Ag scintillator with claddings of air, mylar, and teflon. The collection efficiencies are presented in Table 4.12. It was then determined that Teflon tape would be the best material to ensure that the highest fraction of photons are collected. In order to decrease the optical photon absorption a wavelength shifting bar was employed. The effect of using a wavelength shifting bar instead of PMMA of a light guide is dramatic; a factor of almost 10 more photons are detected when the wavelength shifting bar is employed.

A four layered detector design was then simulated with GEANT4 in order to determine the number of optical photons that were collected. This design has the 100 µm, 10% loaded ^{6}LiF films sandwiched between wavelength shifting (each 5 mm

Table 4.13: Effect of a WLS on the light collection of a scintillating slab. The simulation is 100 µm thick slice of material 2 m long, 30 cm wide with a rectangular PMT on each end.

	Percent Photons Crossing Boundary	
Detector Material	PMMA	WLS
EJ-200	0.68%	12%
PS LiF	0.14%	4.3%
EJ-426	1.3×10^{-3}%	4.5×10^{-3}%

thick) with a single PMT at the top and bottom. This design collects 8% of the optical photons emitted; for a polystyrene film with an average light yield of 2,000 photons per neutron 400 would then hit the photocathode. It is expected that this is enough photons to create a signal above the noise for a typical PMT, while an increased signal can be achieved by additional PMTs.

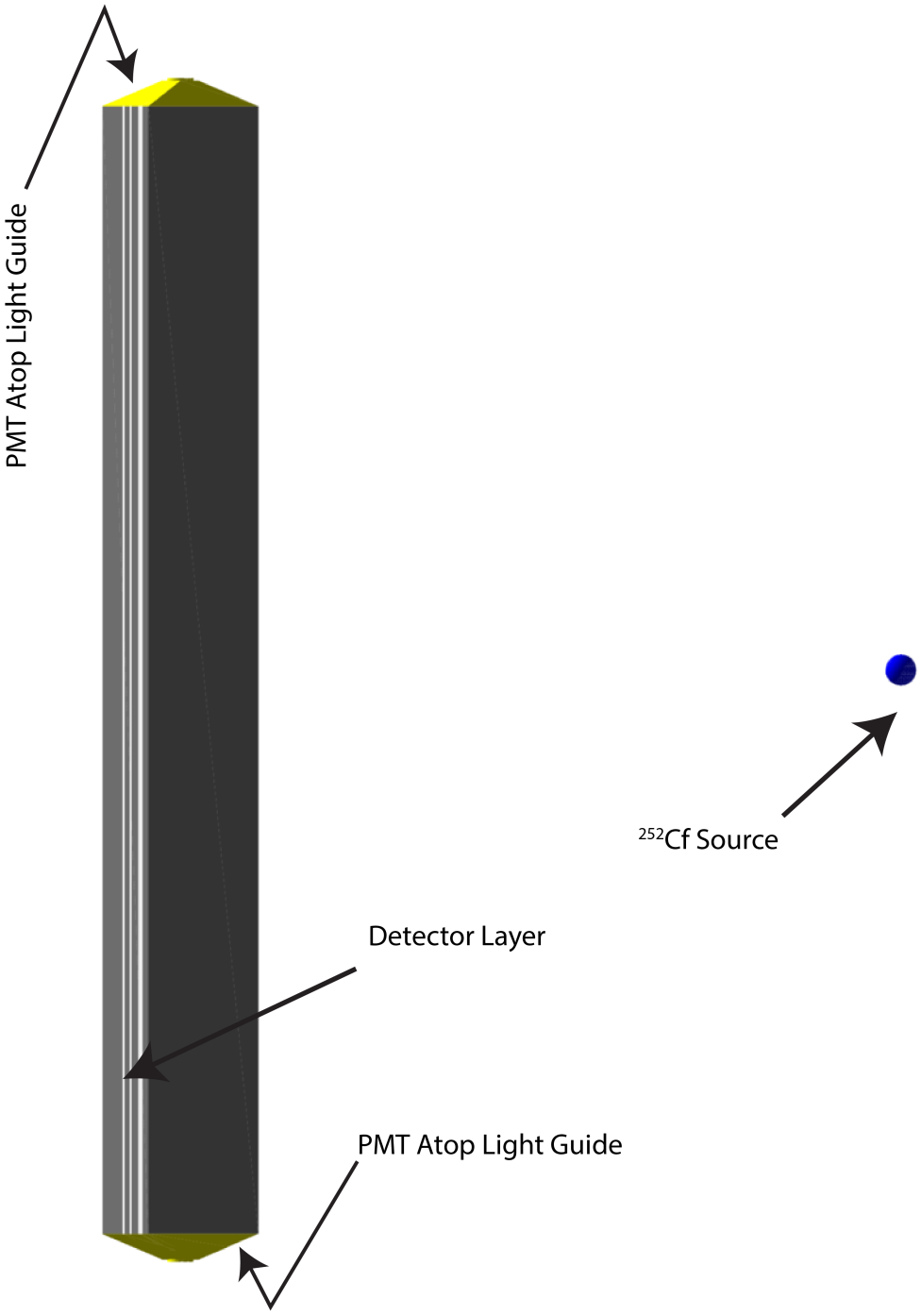

Figure 4.19: Simulated RPM8 with light transport in GEANT4. This design is capable of meeting all of the criteria set forth for radiation portal monitors.

4.4 Simulated Detector Performance

A replacement portal monitor has been designed for layered polymeric films that effectively utilize the ^{6}Li in the detector material. An example of the an optimized geometry is shown in Figure 4.20 in which the films are 100 µm thick placed in a wavelength shifter. The positions of the films necessary to meet the detector criteria are shown in Table 4.14. These layered detector designs consist of 100 µm, ^{6}Li fluoride loaded polymers that are encased in 5 mm of a wavelength shifting plastic in addition to a 100 µm ^{6}LiF loaded ZnS:Ag commercial scintillator also encased in a wavelength shifter. The wavelength shifter was assumed to have a material composition similar to that of high density polyethylene, which also served as the moderator. If two 2 in photomultiplier tubes are placed at the top and bottom of a fishtail light guide mounted on the top and bottom of the detector cabinet, 8% of the optical photons generated in a 10% loaded polystyrene film can be collected. It is assumed for the estimated 5 in PMT photons collected that the light collection efficiency of 5 in PMT can be estimated from the ratio of the 2 in PMT to 5 in PMT light collection efficiency as reported in [Jordan et al., 2003].

Table 4.14: Simulated detector performance in a design capable of meeting the DHS / DNDO criteria.

Detector Composition	Film Positions	Estimated Photons Collected	
		2 in PMT	5 in PMT
10% ^{6}LiF polystyrene	2.54 cm, 3.82 cm, 6.36 cm	160	432
10% ^{6}LiF polyethylene naphthalene	1.90 cm, 3.82 cm, 5.08 cm	240	410
^{6}LiF loaded ZnS:Ag	3.17 cm, 6.35 cm	1,900	5,130

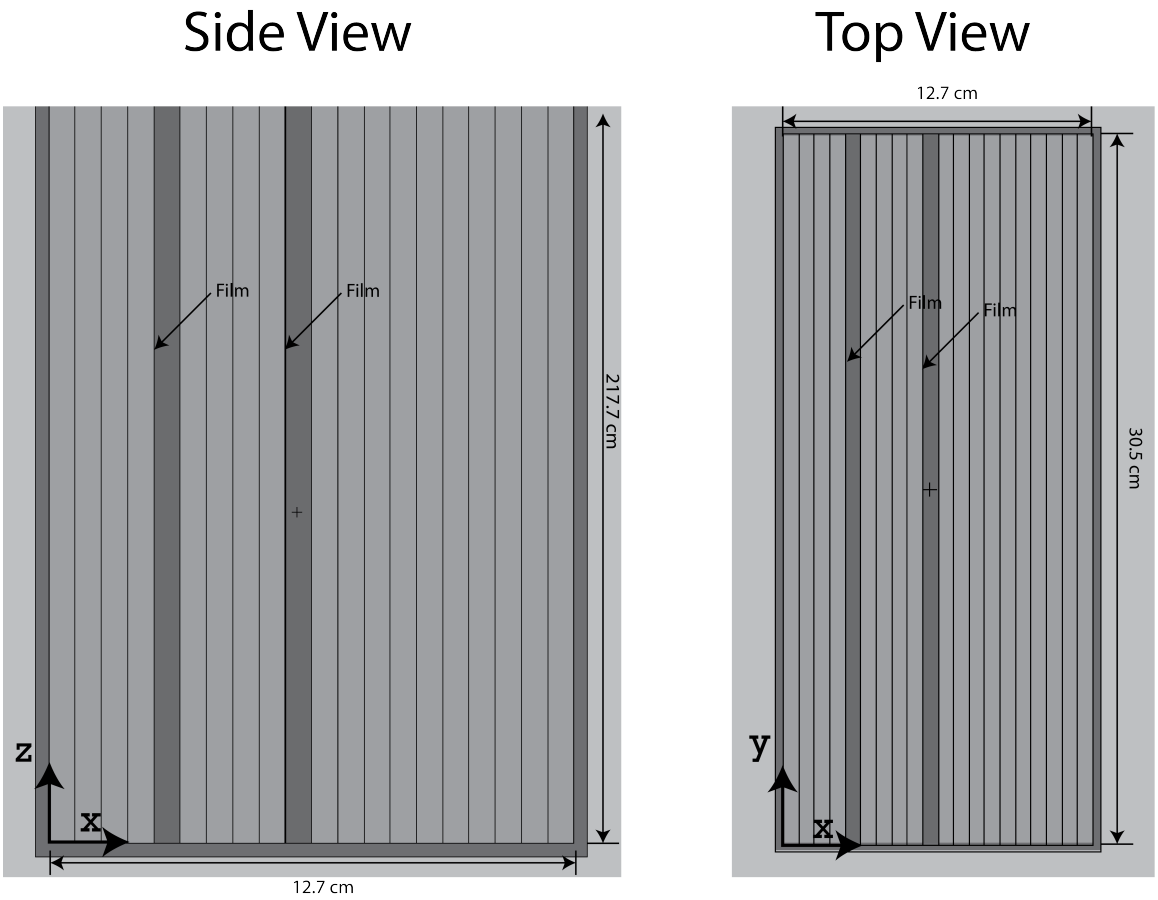

Figure 4.20: Example geometry of a film inside the radiation portal monitor. The film material is ^{6}LiF loaded ZnS:Ag, which has a high loading of ^{6}Li. The origin is shown in the lower left of each figure, along with the axis.

Chapter 5

Conclusions

Thin polymeric films loaded with ^{6}Li films or ^{6}Li loaded ZnS:Ag scintillators show promise for replacement portal monitors. Design of a replacement detector technology capable of meeting the criteria set forth by DHS/DNOD needs to consider the neutron interaction used for detection, the subsequent energy deposition of the reaction products into the material, the scintillation that results from the energy deposition, and the transport of photons from the interaction site to the photomultiplier tube. Understanding these complex reactions involve understanding the mechanisms of scintillation, light transport, and energy deposition. Techniques need to be developed for determining the gamma intrinsic efficiency and simulated detector performance while validating the simulations with measurements.

5.1 Neutron - Gamma Discrimination

The neutron - gamma discrimination necessary for RPMs may be satisfied for thin films by employing a pulse height discriminator. A mathematical lower level discriminator (MLLD) is established for a given film by computing for which channel the integrated photon spectra (above the given channel) normalized by the photon fluence (determined by MCNPX simulations) is less than 1×10^{-6}. Counts above the MLLD are classified as neutron counts, and counts below are discarded. The thickness of the film impacts

the discrimination firstly through the interaction rate, but a far greater contribution to the neutron - gamma discrimination originates from the range of the secondary electrons produced by Compton scattering in gamma-photon events and their energy deposition. The electrons from the gamma interactions generally have energies on the order of 100 keV, while energies from the charged particle reactions of the neutrons have energies or the order to 10 keV. Thus, the neutron reaction product energies tend to deposit more energy in the film than their gamma produced counterparts. It is the poor energy deposition by electrons generated from photon events that allow for films to be much thicker than the thickness predicted based on the interaction rate. A 150 µm thick film absorbs over 90% of the energy deposition of the neutron reaction products, thus there is little reason to fabricate films thicker than 150 µm because it allows for a greater percentage of energy to be deposited from gammas, resulting in a higher MLLD setting and a lower amount of neutron counts that can be considered.

5.2 Film Placement

A single film does not have an adequate neutron count rate to satisfy the neutron detector requirements of 2.5 cps per nanogram ^{252}Cf in a source that is 2 m from the detector midpoint, shielded by 0.5 cm of lead and moderated by 2.5 cm of high density polyethylene. Layering the detectors, however, has been shown to improve the neutron count rate while maintaing the necessary gamma intrinsic detection efficiency. A simple repeated layer design was first proposed, but due to the changing neutron flux through the detector, it was quickly discarded as a poor utilization of the ^{6}Li. Genetic algorithms were employed to optimize a binary model of the detector for the optimal geometry that had the highest count rate while using the least amount of absorber and still meeting the detection efficiency criteria. This model consisted of using a binary representation of the layered detector geometry (where each layer is either a detector slice or moderator slice). The model was then evaluated using MCNPX and XSDRN to simulate the expected neutron interaction rate performance.

The position of the slices necessary for having the best usage of the absorber material while still maintaining the neutron count rate necessary for the criteria are then determined by the genetic algorithm. These layered detector designs consist of 100 µm, ^{6}Li fluoride loaded polymers that are encased in four millimeters of a wavelength shifter. Three such layers (30 percent loaded with enriched LiF) can achieve an interaction rate of 3.82 interactions per second per nanogram of Cf-252 (using 12.6 grams of ^{6}Li), while five layers can achieve an interaction rate of 5.31 interactions per second per nanogram of Cf-252 (using 21.0 grams of ^{6}Li) and ten layers can achieve an interaction rate of 7.56 interactions per second per nanogram of Cf-252 (using 41.2 grams of ^{6}Li). Annotated MCNPX renderings of these geometries are shown in Figure 4.11, Figure 4.12, and Figure 4.13.

A physical basis of the optimal solution found by the genetic algorithm can be found by observing the form of the optimal solutions. These solutions involve an initial moderator layer in order to ensure neutron thermalization. After this moderator layer a film layer is placed to capture the thermal neutron spectra; however, not all of the thermal neutrons are captured (as the mean free path of a neutron in polyethylene is about 0.37 cm and thus some pass through the material). A second absorber layer is needed to capture those neutrons. The neutron flux is then moderated again, and additional layers of detectors are needed to capture this neutron cross section. However, it is desirable to have a large neutron reflector in the portal monitor to reflect neutrons back into the detector slices. Theoretically, this reflector should be as thick as possible, but the limited space of the RPM provides a constraint.

A wrapped detector design in which the detector layers are wrapped around a cylinder in concentric circles was also simulated for a variety of absorber loadings in polystyrene and polyethylene naphthalene. It is observed that the neuronic performance does not depend greatly on the polymer in which the absorber in placed, although the PEN films contain a slightly lower mass fraction of ^{6}Li for the same mass fraction of ^{6}LiF as polystyrene due to PEN having a higher atomic weight than polystyrene. Four cylinders (each 2 cm in outer diameter) placed equidistant in the

RPM8 loaded with 30% ^{6}LiF would have an interaction rate above 3.2 interactions per second per nanogram ^{252}Cf, thus meeting the neutron count rate criteria. These assemblies use 28 g of ^{6}Li, compared to the 12.6 g of ^{6}Li used in a layered design of a similar count rate. This is a poor utilization of the absorber mass, but, it is attractive due to the ease of collecting the photons with a single PMT on the top and bottom of each cylinder. The ^{6}Li utilization of the four cylinder design can be improved by adding a fifth cylindrical detector assembly and increasing the spacing between the detector, which is leading to an approximation of planar sheet geometry.

5.3 Light Collection

Light transport modeling provides a method to calculate the performance of a detector design while providing improvement insights. GEANT4 was used to simulate the neutron interactions, energy deposition, scintillation (with quenching) and the light transport to a PMT for a radiation portal monitor design (shown in Figure 4.19). This design has the 100 µm, 10% loaded ^{6}LiF films sandwiched between wavelength shifting (each 5 mm thick) with a single PMT at the top and bottom. This design collects 8% of the optical photons emitted; for a polystyrene film with an average light yield of 2,000 photons per neutron 160 would then hit the photocathode. If a 5 in PMT is used instead of a2 in PMT it is estimated that the light output increases by a factor of 2.7 [Jordan et al., 2003].

5.4 Design Improvements

It is known that the scintillation events that occur near the center of the detector have a low probability of their photons reaching the PMT. Thus, the light collection efficiency could be improved by eliminating that material or by dedicating another PMT to cover the detector mid region. Different light collection strategies could also be employed in which more PMT's (or larger PMTs) are added at different locations to

improve the light collection, or using different wavelength shifters, coupling materials, and light guides. Another improvement in the light collection could be to fabricate films that have less internal optical photon absorption. In addition, the large mass of ^{6}Li required could be reduced by examining methods in which an alternative to pulse height discrimination is employed, thus allowing for more of the neutron spectra to be utilized. There still exists the need to couple the optimization of the light transport with the material usage. For instance, it might be beneficial to have smaller subunits of (each optically independent) detector materials rather than monolithic slabs. Another design might exploit the trade-off in the neutron fraction above the discrimination criteria by employing different film thickness in different locations within the radiation portal monitor.

Bibliography

[Agostinelli et al., 2003] Agostinelli, S., Allison, J., Amako, K., and et al. (2003). Geant4—a simulation toolkit. *Nuclear Instruments and Methods in Physics Research Section A: Accelerators, Spectrometers, Detectors and Associated Equipment*, 506(3):250–303. 38, 39

[Berger et al., 2005] Berger, M., Coursey, J., Zucker, M., and Chang, J. (2005). ESTAR, PSTAR and ASTAR: computer programs for calculating stopping-power and range tables for electrons, protons, and helium ions. 13, 16

[Birks, 1951] Birks, J. B. (1951). Scintillations from organic crystals: Specific fluorescence and relative response to different radiations. *Proceedings of the Physical Society. Section A*, 64(10):874–877. 23

[Carel W.E, 2001] Carel W.E, v. E. (2001). Inorganic-scintillator development. *Nuclear Instruments and Methods in Physics Research Section A: Accelerators, Spectrometers, Detectors and Associated Equipment*, 460(1):1–14. 4, 132

[Ely et al., 2013] Ely, J., Siciliano, E., Swinhoe, M., and Lintereur, A. (2013). Modeling and simulation optimization and feasibility studies for the neutron detection without helium-3 project. *PNNL 22228*. 5

[ENDF/B-VII, 2013] ENDF/B-VII (2013). Cross section evaluation working group (ENDF/B-VII). *National Nuclear Data Center*. 12

[Gobain, 2008] Gobain, S. (2008). Premium plastic scintillators. 30

[Gobain, 2012] Gobain, S. (2012). Detector assembly materials. 30

[Greene et al., 2011a] Greene, N., Petrie, L., and Westfall, R. (2011a). *NITAWL: Scale System Module for Performing Resonance Sheilding and Working Library Production*. Reactor and Nuclear Systems Division, ORNL, Oak Ridge, TN. 56

[Greene et al., 2011b] Greene, N., Petrie, L., and Williams, M. (2011b). *XSDRNPM: A One-Dimensional Discrete-Ordinates Code for Transprot Analysis*. Reactor and Nuclear Systems Division, ORNL, Oak Ridge, TN. 34

[Hull et al., 2009] Hull, G., Zaitseva, N., Cherepy, N., Newby, J., Stoeffl, W., and Payne, S. (2009). New organic crystals for pulse shape discrimination. *Nuclear Science, IEEE Transactions on*, 56(3):899–903. 25

[Janecek and Moses, 2010] Janecek, M. and Moses, W. W. (2010). Simulating scintillator light collection using measured optical reflectance. *Nuclear Science, IEEE Transactions on*, 57(3):964–970. 46

[Jordan et al., 2003] Jordan, D., Geelhood, B., Reader, P., Stephens Jr, D., Craig, R., and McIntyre, J. (2003). Progress report on the advanced large-area plastic scinttillators (alps) project. *PNNL 14283*. ix, 90, 94, 99

[Knoll, 2009] Knoll, G. F. (2009). *Radiation Detection and Measurement*. Wiley, New York. 29, 30, 132, 133

[Kouzes and Ely, 2010] Kouzes, R. and Ely, J. (2010). Lithium and zinc sulfide coated plastic neutron detector test. *PNNL 19566*. 4

[Kouzes et al., 2012] Kouzes, R., Ely, J., and Stromswold, D. (2012). Boron-lined straw-tube neutron detector test. *PNNL 19600*. 4

[Kouzes et al., 2010] Kouzes, R. T., Ely, J. H., Erikson, L. E., Kernan, W. J., Lintereur, A. T., Siciliano, E. R., Stephens, D. L., Stromswold, D. C., Van Ginhoven, R. M., and Woodring, M. L. (2010). Neutron detection alternatives to 3He for national security applications. *Nuclear Instruments and Methods in Physics Research Section A:*

Accelerators, Spectrometers, Detectors and Associated Equipment, 623(3):1035–1045. 1, 2

[Mabe et al., 2013] Mabe, A. N., II, J. D. A., Urffer, M. J., Penumadu, D., Schweitzer, G. K., and Miller, L. F. (2013). Transparent lithiated polymer films for thermal neutron detection. *Nuclear Instruments and Methods in Physics Research Section A: Accelerators, Spectrometers, Detectors and Associated Equipment*, 722(0):29 – 33. 6

[Pelowitz, 2006] Pelowitz, D. (2006). MCNPX user's manual 2.6.0. *Los Alamos National Laboratory.*, LA-CP-07-1473. 54, 113

[Riggi et al., 2011] Riggi, S., La Rocca, P., and Riggi, F. (2011). Introducing third-year undergraduates to GEANT4 simulations of light transport and collection in scintillation materials. *European Journal of Physics*, 32(2):329–341. 31

[RT et al., 1999] RT, K., Ely, J., Lintereur, A., and Stephens, D. (1999). Neutron detector gamma insenstivity criteria. *PNNL 18903*. 2, 3

[Sen et al., 2012] Sen, I., Urffer, M., Penumadu, D., Young, S., Miller, L., and Mabe, A. (2012). Polyester composite thermal neutron scintillation films. *Nuclear Science, IEEE Transactions on*, 59(4):1781–1786. 6

[Stacey, 2001] Stacey, W. (2001). *Nuclear Reactor Physics*. Wiley. 10

[Turner, 2008] Turner, J. E. (2008). *Atoms, Radiation, and Radiation Protection*. Wiley-VCH, Hoboken, NJ, USA. 16

[Turner et al., 1982] Turner, J. E., Paretzke, H. G., Hamm, R. N., Wright, H. A., and Ritchie, R. H. (1982). Comparative study of electron energy deposition and yields in water in the liquid and vapor phases. *Radiation Research*, 92(1):47–60. ArticleType: research-article / Full publication date: Oct., 1982 / Copyright © 1982 Radiation Research Society. 39, 41

[Van Ginhoven et al., 1999] Van Ginhoven, R., Kouzes, R., and Stephens, D. (1999). Alternative neutron detector technologies for homeland security. *PNNL 18471*. 1, 3

[Verbinski et al., 1968] Verbinski, V., Burrus, W., Love, T., Zobel, W., Hill, N., and Textor, R. (1968). Calibration of an organic scintillator for neutron spectrometry. *Nuclear Instruments and Methods*, 65(1):8 – 25. 24, 25

Appendix

Appendix A

Compton Scattering

Compton scattering is the inelastic scattering of a photon off a free charged particle, usually an electron. The incident photon undergoes a decrease in energy, transferring the energy to the kinetic energy of the electron while also having a scattered photon. Figure A.1 is a representation of the phenomena, in which the incident photon has a wavelength λ which after scattering angle θ has a final energy of λ'.

$$\frac{1}{E'} - \frac{1}{E} = \frac{1}{m_e c^2}(1 - \cos\theta) \tag{A.1}$$

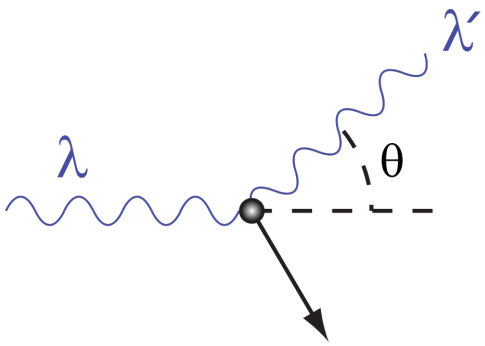

Figure A.1: Compton Scattering of a Photon off an Electron

Using the conservation of energy, the energy given to the electron, E_e must be equal to the difference in the initial and final photon energies (A.2)

$$\begin{aligned} E_e &= E - E' \\ &= E - \frac{E m_e c^2}{m_e c^2 + E(1 - \cos\theta)} \end{aligned} \tag{A.2}$$

A.1 Differential Scattering Cross Section

The probability of scattering and imparting energy is provided by the Klein-Nishina formula (A.3).

$$d\sigma = \frac{1}{2} r_0^2 \left(\frac{E'}{E}\right)^2 \left(\frac{E'}{E} + \frac{E}{E'} - \sin^2\theta\right) d\Omega \tag{A.3}$$

If $f(\theta)$ is defined as $f(\theta) = \frac{1}{2}\left(\frac{E'}{E}\right)^2 \left(\frac{E'}{E} + \frac{E}{E'} - \sin^2\theta\right)$ and assuming the scattering is isotropic leading to $d\Omega = \sin\theta d\theta d\phi$ it is then possible to express (A.3) as (A.4).

$$d\sigma = r_0^2 f(\theta) \sin\theta d\theta d\phi \tag{A.4}$$

It is then possible to integrate over ϕ, and then divide by the differential scattering angle to arrive at (A.5).

$$d\sigma = \int_{\phi=0}^{2\pi} r_0^2 f(\theta) \sin\theta d\theta d\phi \tag{A.5}$$

$$\frac{d\sigma}{d\theta} = 2\pi r_0^2 f(\theta) \sin\theta \tag{A.6}$$

However the probability of scattering at a given kinetic energy of the electron is desired, $d\sigma/dE_e$. With the chain rule and a few algebraic manipulations it is possible to arrive at (A.7), and if the derivative of (A.2) is taken with respect to θ the differential energy

scattering can be expressed as (A.9).

$$\frac{d\sigma}{dE_e} = \frac{d\sigma}{d\theta}\frac{d\theta}{dE_e} \tag{A.7}$$

$$= \frac{d\sigma}{d\theta}\left[\frac{dE_e}{d\theta}\right]^{-1} \tag{A.8}$$

$$\frac{d\sigma}{dE_e} = 2\pi r_e^2 \sin\theta f(\theta)\left[\frac{1+\frac{E}{m_e c^2}(1-\cos\theta)^2}{E^2\sin\theta}\right] \tag{A.9}$$

A.2 Computational Spectra

The probability of a Compton scattered electron having an energy E was calculated by sampling (using a rejection method) for the scattering distribution derived in Equation A.9. This probability was then normalized into a probability density function and the cumulative density function was then calculated to yield the probability that an electron would be born at an energy.

Appendix B

MCNPX Simulations

The performance of films is simulated in MCNPX, a Monte Carlo transport code[Pelowitz, 2006].

The interaction rate is calculated using the a cell flux tally in MCNPX and a tally multiplier card. The tally multiplier card (FMn) is used to calculated any quantity of the form (B.1) [Pelowitz, 2006]

$$I = C \int \phi(E) \Re_m(E) dE \tag{B.1}$$

where I is the Interaction rate, $\phi(E)$ is the Energy dependent fluence , $\Re_m(E)$ is the Response function operator and C is an arbitrary scalar for normalization. An general example of the use of the FM card is shown in Listing B.1, which is taken from the MCNPX manual [Pelowitz, 2006].

Listing B.1: Example usage of the FM card to calculate the number of reactions per cm^3 of type R in cell 8 of material M. The normalization is by atomic density, signified by the -1

```
1 F104: N 8
  FM104 -1 M R
```

The reaction rate $^6\mathrm{Li}\,(\mathrm{n},\mathrm{t})\,\alpha$ can be calculated by then applying the appropriate input for the FMn card and using an F4 card to calculate $\phi(E)$. It should be noted

that depending on the form of the cell flux card it may be necessary to normalize by the volume of the cell, $\forall$.

This is shown in Listing B.2, where the reaction number is 105 and the material number of the detector is 3. The interaction rate in a simulated RPM8 replacement detector is calculated in a similar manner as the simulation of the measured detectors; the interaction rate as computed by the `FMn` is multiplied by the source strength and volume if necessary. An example of the MCNPX input cards is shown in Listing B.2. Given that there the thermal response is not desired, there is no need to subtract out the differences between the spectra, and the interaction rate is simply (B.2). Note that in this calculation the source strength is set to be 1 ng ^{252}Cf, which has a neutron emission rate of 2.3×10^3 neutron/s. This is in accordance with the direct evaluation of the PNNL criteria, which require a absolute neutron count rate of 2.5 count/s/ng^{252}Cf.

Listing B.2: RPM8 $^6\mathrm{Li}\,(\mathrm{n},\mathrm{t})\,\alpha$ Reaction Rate. The detector is all of the layers of cell 500 inside universe 610. This tally is multiplied by an SD card to normalize by the volume.

```
FC4 (n,t) Reactions in Thin Film (Neutron Detector)
F4:n (500<610)
SD4 1
FM4 -1 3 105
```

$$I_{\mathrm{sim}} = S_0 I \tag{B.2}$$

$$= 2.3 \times 10^3\,\mathrm{neutron/s} I \tag{B.3}$$

I_{sim} provides the total number of simulated neutron interactions in the detector.

B.1 Example of Layered Detector Geometry

The following tables provide examples of the positions of the layered geometry used for the genetic algorithm. These geometries correspond to Figure 4.11 and Figure 4.12, and Figure 4.13.

Table B.1: Optimal layered film geometry for an interaction rate of 7.5 interactions per second per nano-gram ^{252}Cf in a 10% ^{6}Li loaded PS film. The positions shown in the table are the right boundary, where the detector starts at 0.0 cm. The genome representing this geoemtry is `01111101110100001000`.

Position (cm)	Material
0.635	Moderator
0.645	Detector
1.270	LightGuide
1.280	Detector
1.905	LightGuide
1.915	Detector
2.540	LightGuide
2.550	Detector
3.175	LightGuide
3.185	Detector
3.810	LightGuide
4.445	Moderator
4.455	Detector
5.080	LightGuide
5.090	Detector
5.715	LightGuide
5.725	Detector
6.350	LightGuide
6.985	Moderator
6.995	Detector
7.620	LightGuide
8.255	Moderator
8.890	Moderator
9.525	Moderator
10.160	Moderator
10.170	Detector
10.795	LightGuide
11.430	Moderator
12.065	Moderator
12.700	Moderator

Table B.2: Optimal layered film geometry for an interaction rate of 5.0 interactions per second per nano-gram ^{252}Cf in a 10% ^{6}Li loaded PS film. The positions shown in the table are the right boundary, where the detector starts at 0.0 cm. The genome representing this geoemtry is `011101001000000`.

Position (cm)	Material
0.847	Moderator
0.857	Detector
1.693	LightGuide
1.703	Detector
2.540	LightGuide
2.550	Detector
3.387	LightGuide
4.233	Moderator
4.243	Detector
5.080	LightGuide
5.927	Moderator
6.773	Moderator
6.783	Detector
7.620	LightGuide
8.467	Moderator
9.313	Moderator
10.160	Moderator
11.007	Moderator
11.853	Moderator
12.700	Moderator

Table B.3: Optimal layered film geometry for an interaction rate of 2.5 interactions per second per nano-gram ^{252}Cf in a 10% ^{6}Li loaded PS film. The positions shown in the table are the right boundary, where the detector starts at 0.0 cm. The genome representing this geoemtry is `0011010000`.

Position (cm)	Material
1.270	Moderator
2.540	Moderator
2.550	Detector
3.810	LightGuide
3.820	Detector
5.080	LightGuide
6.350	Moderator
6.360	Detector
7.620	LightGuide
8.890	Moderator
10.160	Moderator
11.430	Moderator
12.700	Moderator

Appendix C

Introduction to GEANT4

GEANT4 is a free toolkit for the simulation of particles as they travel through matter. While nothing can replace the User's Manual, this is intended as a short guide to introduce a reader to the GEANT4 toolkit, and provide background on how the simulations were implemented.

C.1 Toolkit Fundamentals

A simulation in the GEANT4 toolkit requires a detector geometry (including materials), particles and interactions, and primary events. Once the geometry and physics has been described, GEANT4 then tracks the primary particle (and generated secondaries) until the particle leaves the world volume, slows down to zero kinetic energy, or disappears by an interaction or decay. Particles can also be killed by implementing a range a cut, in which the particle is killed once its energy is less than the range. The GEANT4 toolkit employs the following notation to describe a simulation. A *track* contains information about the a particles steps through a material, and acts like a snapshot of the particle. *Processes* contain implementations of models of the physics interactions. Processes are used by *tracking*, which can be thought of a linked list of tracks, where the links between the tracks are the processes. A collection of tracking objects then makes up an *event*. A *run* is then events that share a common beam

and detector implementation. A description of a run in GEANT4 is as follows. At the beginning of a run the geometry is optimized and cross-sections are computed for the materials involved in the run. Primary particles are then generated, and the corresponding tracks are then pushed into an event stack. Each track in the stack is then processed until the event stack is empty. Tracks that are above the cutoff value and inside the world geometry are processed by the use of a *step* (a change in the track) and then pushed back onto the track.

C.2 Optional User Classes

Access to the simulation results is then provided by UserAction classes. These classes are employed to hook into the GEANT4 simulation internals. The user classes used in these simulations are described below.

- `G4UserRunAction` - which has methods that are called before the beginning of each run and at the end of each run. Typical usage is to initialize histograms and book them at then end of the run.
- `G4UserEventAction` - has methods that are called before and after each event. Typically it is used for summarizing an event, such as calculating the total energy deposition or track length.
- `G4UserStackingAction` - this class is called before each track is pushed onto the event stack, and provides an opportunity for the user to kill tracks.

It should be noted that if a track is killed in the stacking or tracking action that GEANT4 does account for the lost energy in the track, thus the user is responsible for recording it if it is desired.

C.3 Physics List

The physics list in GEANT4 describe how the particle interact with matter. There are seven major categories of physics that are considered in GEANT4; electromagnetic, hadronic, transportation, decay, optical, photolepton & hadron, and parameterisation. A physics process is applied to particle in GEANT4 after polling all of the processes attached to a particle to find the limiting process. Only after the limiting process is found is it applied to the particle, changing the position, energy, time, and other parameters. The physics list also serves to apply cuts to the particles based on the range of the particle.

C.3.1 Hadronic Physics

The hadronic physics list employed in GEANT4 construct hadrons (of which neutrons are a part of) and assign physics processes to those particles. The physics list used in this work is `HadronPhysicsQGSP_BERT_HP` which is a Quark Gluon String model for very high energies that the transported down to 20 MeV with the Bertini cascade model. Once the hadrons are in the 20 MeV range data driven cross section models are applied if such a cross section has been measured.

C.3.2 Electromagnetic Physics

The electromagnetic physics in GEANT4 is handled in this work by creating a modular physics list which builds the photons and electrons (among other particles) and assigns processes to them. In the `G4EmStandardPhysics_option4` physics list these processes include ionization, delta ray production, multiple scattering, and annihilation for electrons and pair production, photoelectric effect, and Rayleigh scattering for gammas. This list also build processes for X-rays, including scintillations. However, the photons produced with scintillations are not tracked unless optical physics are implemented.

Table C.1: Optical Parameters Available in the GEANT4 model

Category	Parameter
General	RINDEX, ABSLENGTH
Scintillation	SCINTILLATION, FASTCOMPONENT, SLOWCOMPONENT, SCINTILLATIONYIELD, RESOLUTIONSCALE, FASTTIMECONSTANT, SLOWTIMECONSTANT, YIELDRATIO
WLS	WLSABSLENGTH, WLSCOMPONENT, WLSTIME
Boundary	Finish, Model, Type, RINDEX, SPECULARLOBECONSTANT, BACKSCATTERCONSTANT, REFLECTIVITY, EFFICIENCY, POLISH

The `G4EmStandardPhysics_option4` is not the lowest energy model, the GEANT4-DNA extension provides models for energies down to a few eV but only for liquid water.

C.3.3 Optical Physics

The light transport in GEANT4 can be thought of in two components; the generation of the optical photon, and the subsequent transport of that photon. Scintillating materials have a characteristic light yield defined by `SCINTILLATIONYIELD`, and an intrinsic resolution, `RESOLUTIONSCALE`. The number of photons generated during a step by an energy deposition is then a distribution characterized by `RESOLUTIONSCALE`. A prompt and slow component of the scintillator emission spectra may be simulated as `SLOWCOMPONENT` for the slow time component and the fast as `FASTCOMPONENT`, and the ratio between the fast and slow components, `YIELDRATIO`. In the case of wavelength shifters, it is necessary to specify the absorption length, `WLSABSLENGTH`, the emission spectra, `WLSCOMPONENT`, and the time constant between them, `WLSTIMECONSTANT`. The tracking of optical photons may be completed in the material by specifying the bulk absorption is defined by the key `ABSLENGTH`, which is set from empirical absorption length. Table C.1 provides a summary of the different optical parameters available in the GEANT4 model.

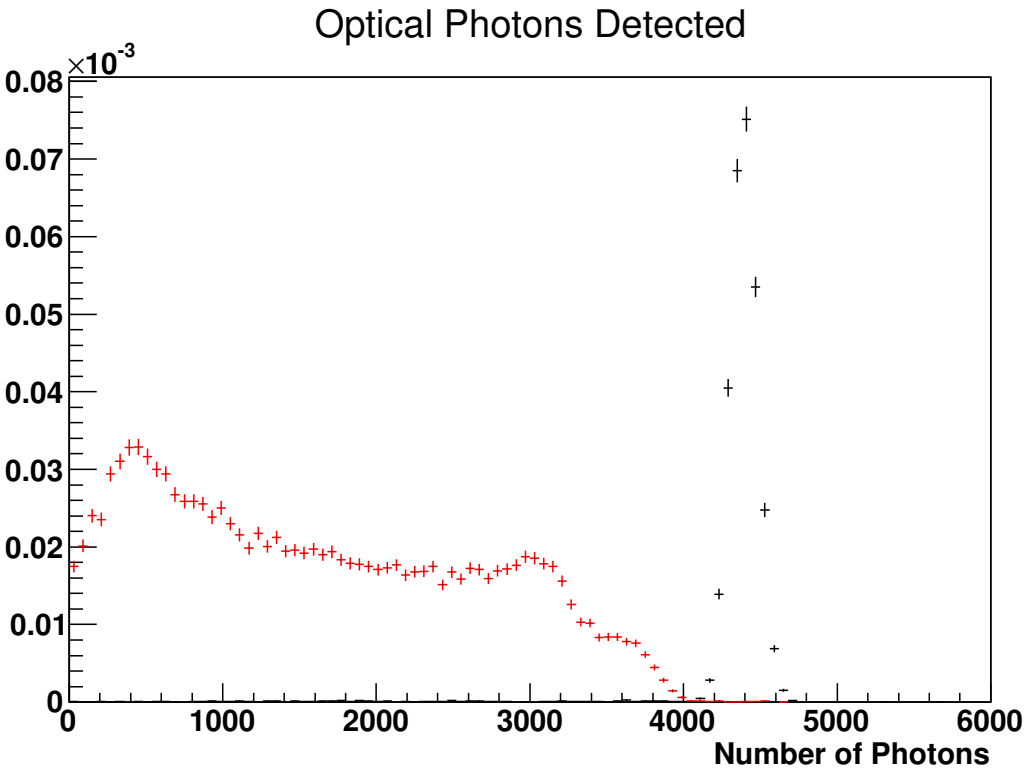

Figure C.1: Simulated Gamma and Neutron Optical Photon Spectra for a Birks constant of $0.02\,\mathrm{mm\,MeV^{-1}}$. The gamma is shown as red, while neutrons are black.

It should be noted that the Birks constant greatly impacts the number of optical photons generated and subsequently detected. For GS20 a Birks constant of $0.1\,\mathrm{mm\,MeV^{-1}}$ produced 1,300 photons per neutron, while a Birks constant of $0.01\,\mathrm{mm\,MeV^{-1}}$ produces 6,900 optical photons per neutron. Birks constants greater than $0.01\,\mathrm{mm\,MeV^{-1}}$ produce marginal increases in the number of optical photons produced; for example 8,600 photons per neutron were produced for a Birks constant of $0.0001\,\mathrm{mm\,MeV^{-1}}$. An example of the effects of the Birks constant is shown in the following figures, Figure C.1,Figure C.2, and Figure C.3. As the Birks constant increases the separation between the neutron and gamma pulses decreases. The Birks constant was then determined semi - empirically for the different material by simulated the light out of the material with different Birks values and using the value that agreed closest to the measured light yield and separation between the neutron

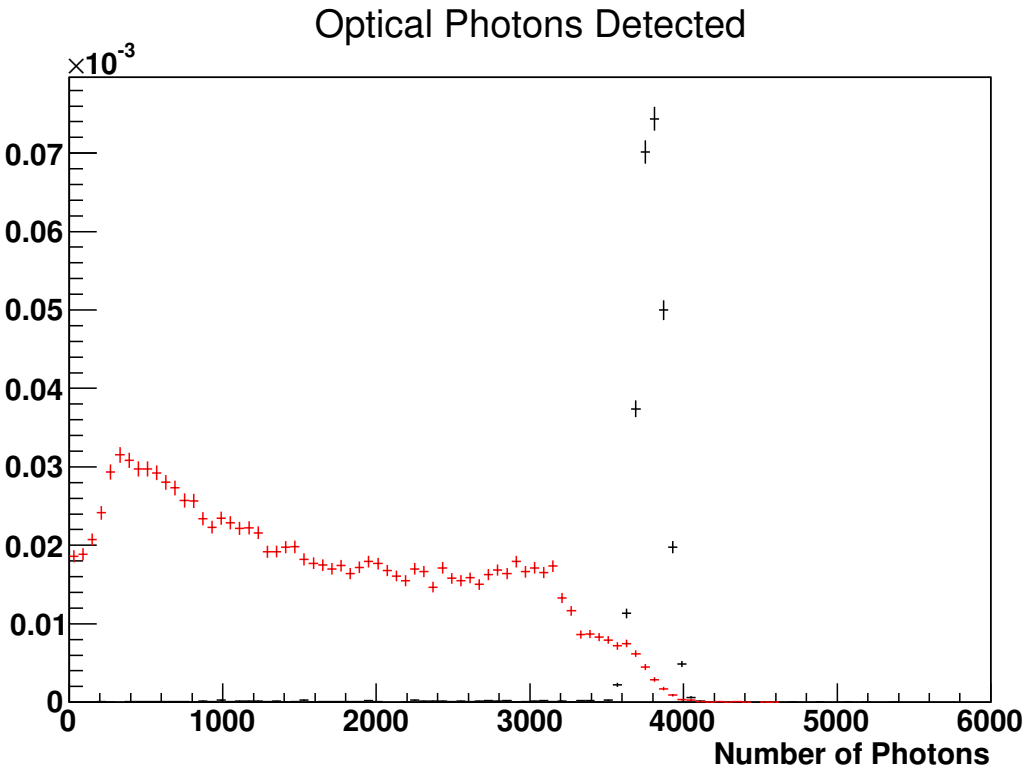

Figure C.2: Simulated Gamma and Neutron Optical Photon Spectra for a Birks constant of $0.025\,\mathrm{mm\,MeV^{-1}}$.

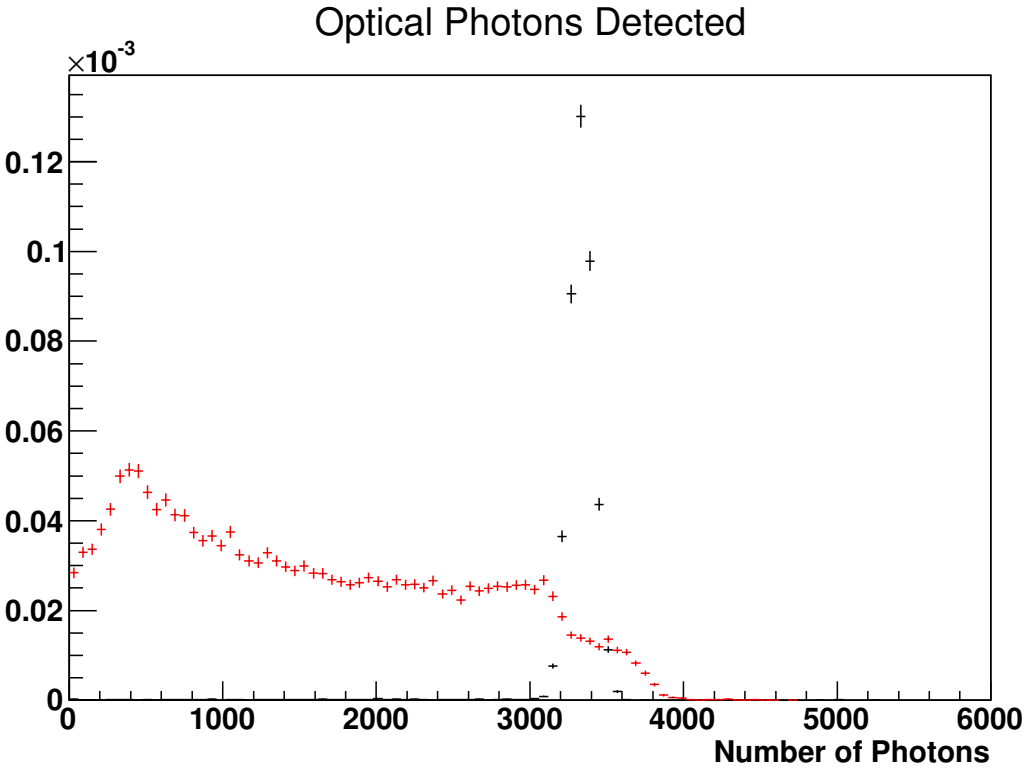

Figure C.3: Simulated Gamma and Neutron Optical Photon Spectra for a Birks constant of $0.03\,\mathrm{mm\,MeV^{-1}}$.

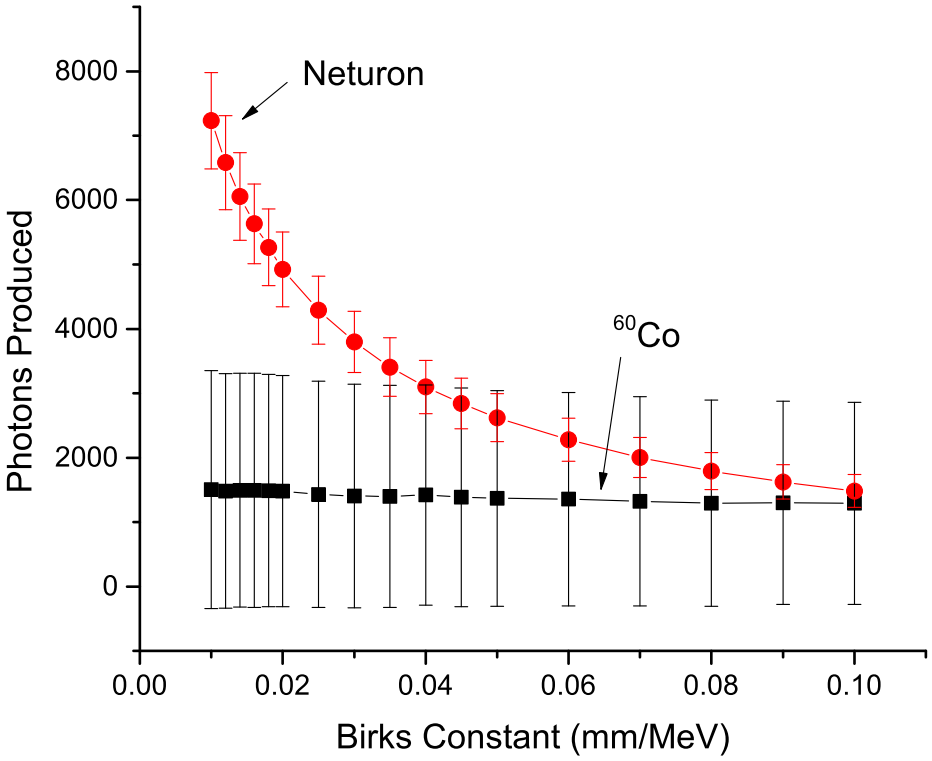

Figure C.4: Simulated Gamma and Neutron Optical Photon production in GS20 for various Birks Constants.

and gamma pulses. This is shown in Figure C.4 for GS20 and in Figure C.5 for a polystyrene based film.

The resolution of the a detector can be set with the `RESOLUTION` parameter in the material property table. The relationship between the `RESOLUTION` parameter and the FWMH can be described as (C.1)

$$\text{RESOLUTION} = \frac{R}{2.35}\sqrt{E \times \text{SCINTILLATIONYIELD}} \tag{C.1}$$

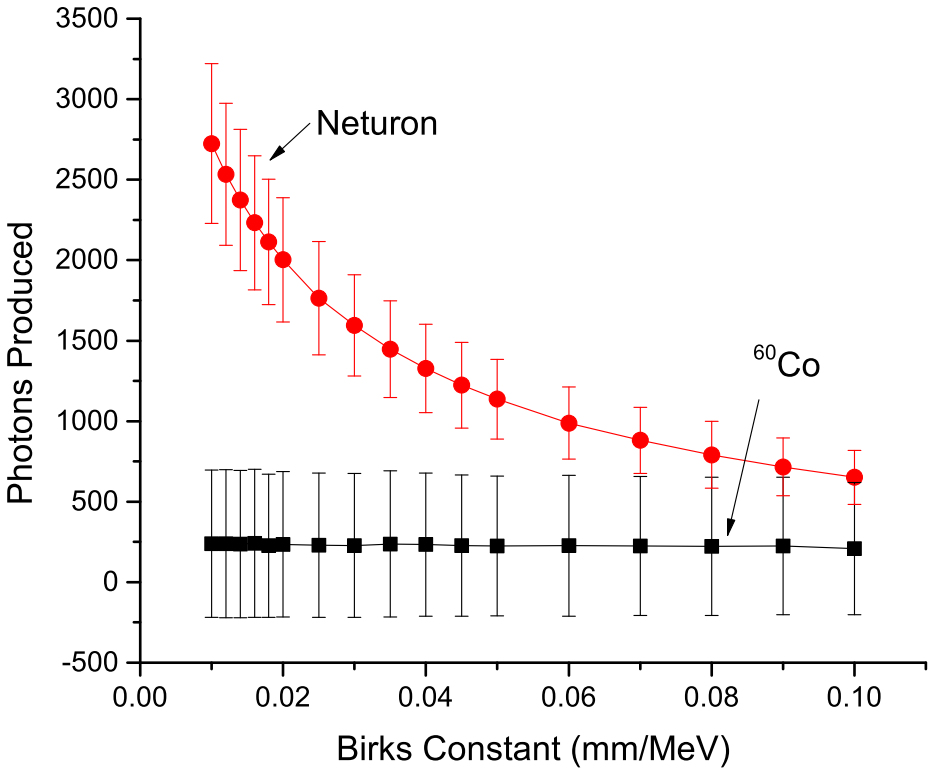

Figure C.5: Simulated gamma and neutron optical photon production in polystyrene for various Birks Constants. A lower Birks constant indicates that a lower pulse height deficit.

where R is the precent resolution (FWHM/Peak) measured at the peak energy, E. For GS20, where the precent resolution is around 15%, this yields a `RESOLUTION` of eight.

Appendix D

Detector Characterization

Repeated characterization techniques of the detector materials are necessary to ensure a fair comparison between different detector materials. As the focus of this work was on effective scintillators the characterizations were designed to measure scintillation properties; namely the light yield of the detector and the count rate when exposed to different radiation sources.

- Total Neutron Counts – provides a measure of how responsive the detector is to neutrons
- Total Neutron Count Rate Per mg Absorber – provides a measure of how well the fabricated detector utilizes the neutron absorber in it. Indirectly this can be a measure of the amount of absorber in the detector
- Gamma LLD – The position (in channel number) of where an LLD would have to be set in order to meet the criteria of 1E−6
- Fraction of Total Neutron Count Rate Above the Gamma LLD – this is a measure of how effective the film would be with an LLD set in order to meet the This is calculated by summing the counts above the gamma LLD and dividing by the total counts.

- Alpha Peak – provides a clear indication of the light yield of the film from an alpha particle, which is one of the reaction products of the 6Li neutron interaction. The alpha peak is visible in thin films when other features may be lost (due to the range of the secondary electrons exceeding the thickness of the detector) because the range of the alpha is on the order of 30 microns.

- Beta Average – characterizes the response of the film to electrons, account for the possibility that a film may not have a clearly defined feature due to energy escaping. Electrons are generated in the film from scattering events of photon interactions.

- Alpha / Beta – characterizes the relative light yield of the detector from heavy charged particles to electrons.

- Pulse Height Deficit – a measure the apparent energy loss (as seen from the pulse height) of a heavy charged ion compared to an electron. This is measured as the difference between the energy of the heavy ion and its apparent energy from the pulse height. It should be noted that this term closely resembles the phenomena described by pulse height defect as seen in semiconductors.

- Photons per Neutron – a measure of the light yield of the film, or how many photons are produced per energy absorbed.

D.0.4 Characterization Electronics and Sources

Solid samples are characterized by mounting them with a thin layer of silicone optical grease (BC-630, index of refraction 2.465) onto a Philips XP2202B 10 Stage PMT most sensitive in the 350 nm to 500 nm region. The PMT is then connected to a Canberra 2007P base, which also functions as a preamplifier. The Canberra 2007P feeds into an Ortec 572A amplifier, and the amplified signal is inputted to an Ortec 926 MCB-ADC. MAESTRO-32 is the used to read the signals from the MCB. Figure D.1 provides an overview of this setup. A general protocol has been developed in order to ensure that

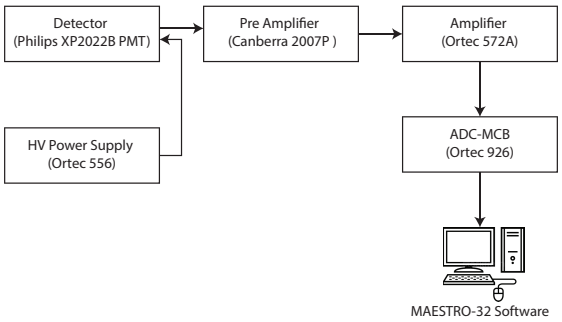

Figure D.1: Electronic figure for measuring the spectra of materials in response to various radiation sources.

the measurements are made in a repeatable manner and verified with a reference.

1. Verify that the instrumentation gains are stable by confirming that the reference neutron peak is in the same channel as for previous measurements. This is completed by setting the voltage and coarse gain to previously determined values, and then adjusting the fine gain until the peak of the lead spectra measurement occurs in the specified location,

2. obtain a spectrum from an Am-241 alpha source,

3. obtain a spectrum from a Cl-36 beta source,

4. obtain a neutron spectrum from the Pb-shielded tube neutron irradiator,

5. obtain a neutron spectrum from the Cd-shielded tube in the neutron irradiator,

6. obtain a gamma spectrum in the gamma irradiator.

Neutron and Gamma Irridiators

The neutron irradiator is a custom built 0.59 µg ^{252}Cf source encased in 2" blocks of high density polyethylene (HDPE). The HDPE box is approximately 20" long, 12" wide, and 14" tall (Figure D.2). There are two detector 1/16" thick acrylic detectors wells, one surrounded by a 1/16" cadmium to shield out thermal neutrons, and the

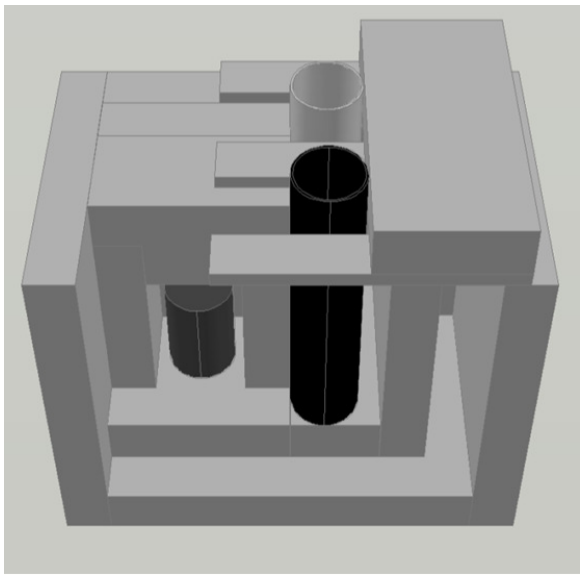

Figure D.2: Schematic of the neturon irridiator.

other surrounded by 1/16" of lead to shield out a similar amount of gammas as the cadmium well. The ^{252}Cf source is surrounded by stainless steel, which in turn is contained within a 2" diameter, 1/2" thick, 5 and 1/4" tall lead vessel. The gamma sources consist of button sources (^{137}Cs up to 10 Či and ^{60}CO up to 1 Či) as well as a gamma irradiator that produces a 10 mR/hr gamma field across the detector face. The irradiator consist of four 4"x8"x 2" lead bricks on the bottom with and additional four 4"x4"x2" lead bricks encased in an 1/8" metal box. The top four inches is HDPE. The overall dimensions of the detector are 14" by 12" by 12".

D.1 Light Yeild

The light yield of a spectrum describes how many photons are generated (and subsequently detected on a PMT) for a given material for a scintillation event from a radiation source. In general, a feature, such as the Compton edge or neutron peak, provides a unambiguous measure of light yield of a film. However, the thinner films do not always have such a clearly defined feature, and thus an alternative measure needs to be formulated. The spectral average is then defined as (D.1) where $p(x)$ is

the measured spectrum as a function of channel number x which describes the count rate average channel number, normalized by the total count rate.

$$< \mu >= \frac{\int_0^\infty xp(x)dx}{\int_0^\infty p(x)dx} \tag{D.1}$$

The limits of integration in (D.1) are from the lowest to the highest channel number. While the spectral average does provide a clear representation of a spectra, it fails to capture the shape of the spectra and tends to underestimate the spectra, as most spectra a skewed having the majority of their counts in the low channel region.

The light yield of fabricated samples that were characterized was completed by comparing the spectrum average of a sample to that a sample of a known light yield. This is shown for neutrons in (D.3), and for gammas in (D.5). GS20 is normally used as the reference sample, having a reported light yield of 3.800 photons /MeV and 6.200 photons /neutron [Carel W.E, 2001, Knoll, 2009].

$$LY_{n,\text{sample}} = LY_{n,\text{ref}} \left(\frac{< n >_{\text{sample}}}{< n >_{\text{ref}}} \right) \tag{D.2}$$

$$= 6.200\,\text{photons/neutron} \left(\frac{< n >_{\text{sample}}}{< n >_{\text{ref}}} \right) \tag{D.3}$$

$$LY_{\gamma,\text{sample}} = LY_{\gamma,\text{ref}} \left(\frac{< \gamma >_{\text{sample}}}{< \gamma >_{\text{ref}}} \right) \tag{D.4}$$

$$= 3.800\,\text{photons/MeV} \left(\frac{< \gamma >_{\text{sample}}}{< \gamma >_{\text{ref}}} \right) \tag{D.5}$$

D.2 Intrisinic Efficiency

Often times it is necessary to relate the performance of a detector to number of particles that cross the detector, this is completed using the intrinsic efficiency. Thus the intrinsic efficiency it is a measure at how efficient the detector is at detecting radiation, normalized to the amount of radiation that crosses the detector. The

intrinsic efficiency is defined as the ratio between the counts recorded in the detector and the number of impingement radiation on the detector[Knoll, 2009], expressed as (D.6),

$$\epsilon_{int} = \frac{N_c}{N_i} \tag{D.6}$$

where:

ϵ_{int} is the intrinsic efficiency,

N_c is the number of counts recorded by the detector, and

N_i is the quanta of radiation incident upon the detector.

In order to determine the intrinsic efficiency of a detector it is then necessary to determine the performance of the detector (easily completed by measuring the detector) and the number of radiation impingement upon the detector (usually accomplished through calculation on simulation).

The quanta of radiation incident upon the detector can be expressed as the product of two components: the source strength and the solid angle, (D.7),

$$N_i = \Omega S_0 \tag{D.7}$$

where:

S is the source strength, and

Ω is the fraction of solid angle detector subtends.

Radiation sources generally decay from their initial source strength according to the half-life of the source. The time dependent source strength, $S(t)$ can then be expressed as (D.8), where S_0 is the initial source strength, $t_{1/2}$ is the half life and t is the age of

source.

$$S(t) = S_0 e^{-\frac{\ln 2}{t_{1/2}} t} \tag{D.8}$$

The fraction of the source solid angle the detector subtends, Ω, is computed using MCNPX. A F1 tally, defined in (D.9), is employed over the detector surface with two cosine bins, $-1 < \cos\theta < 0$ and $0 < \cos\theta < 1$, which divide the tally into particles that enter the surface and particles that leave the surface, respectively.

$$F1 = \int_A dA \int_E dE \int_{4\pi} d\Omega;; \vec{n} \cdot \vec{J}(\vec{r}, E, \vec{\Omega}) \tag{D.9}$$

$$\tag{D.10}$$

In (D.9) the position $\vec{r}\vec{r}$ position, direction $\vec{\Omega}\vec{\Omega}$ direction and energy E E energy dependent particle current $\vec{J}$ $\vec{J}$ particle current is integrated over the entire area, energy and direction normal to the surface of the area. As macro-bodies are used for the surfaces of the detector, $-1 < \cos\theta < 0$ represents the particles that cross into the surface and $0 < \cos\theta < 1$ the particles that leave the surface. In the case where macrobodies are not used to create the cell, the reader is referred to the MCNPX manual for more details.

The count rate of a detector is found by integrating the measured spectra, $p(x)$, over some bounds of integration. It is then possible to express the intrinsic efficiency as a function of a mathematical lower level discriminator (MLLD) of the measured spectra * in order to determine at what MLLD the intrinsic efficiency is less then a value. Equation (D.11) shows such a formulation of the intrinsic efficiency as a function of a MLLD, where the upper bond is assumed to be the end of the spectra or

*The MLLD behaves essentially as a physical lower level discriminator in that all counts below this value are discarded.

highest recorded channel of the analog to digital converter.

$$\epsilon_{int}(MLLD) = \frac{\int_{MLLD}^{\infty} p(x)dx}{N_i} \tag{D.11}$$

D.2.1 Neutron Intrinsic Efficiency

The number of counts upon a detector is measured by irradiating the detector in a lead and cadmium well of the neutron irridiator to determine N_i, and then simulating that geometry in bench-marked MCNPX in order to determine the number of neutrons incident on the detector[†]. The determination of N_i consists of two parts: 1) determining the number of neutrons crossing the detector surface in the lead and cadmium wells and, 2) determining the source strength. The ^{252}Cf source was 0.59 µg on July 2, 2009. Given that the half-life of ^{252}Cf is 2.64 years and ^{252}Cf has a spontaneous neutron emission rate of 2.3×10^6 neutron/s/µg the time dependent source strength can be calculated as (D.12).

$$\begin{aligned} S(t) &= S_0 e^{-\frac{\ln 2}{t_{1/2}}t} \\ &= 0.59\,\mu g\,^{252}\mathrm{Cf}\ \frac{2.3 \times 10^6\,\mathrm{neutron/s}}{\mu g\,^{252}\mathrm{Cf}}\ e^{-\frac{\ln 2}{2.64\,\mathrm{year}}t} \\ &= 1.357 \times 10^6\,\mathrm{neutron/s}\ e^{-\frac{\ln 2}{2.64\,\mathrm{year}}t} \end{aligned} \tag{D.12}$$

Table D.1 summarizes the incident flux for a number of different detector sizes and heights. The fraction of solid angle subtended by other geometries can be computed by interpolation on the values of this table, as shown in the examples calculations. It should be noted that there is considerable variation in the neutron flux in the detector wells, as shown in Figure D.3. Thus, even though the calculations are accurate to less than a percent, the physical error on the intrinsic efficiency will be much higher due to uncertainty in where the detector was placed in the well.

[†]MCNPX simulations were benched-marked against GS20 and against polymer films, having 4% and 15% agreement to measured count rate, respectively.

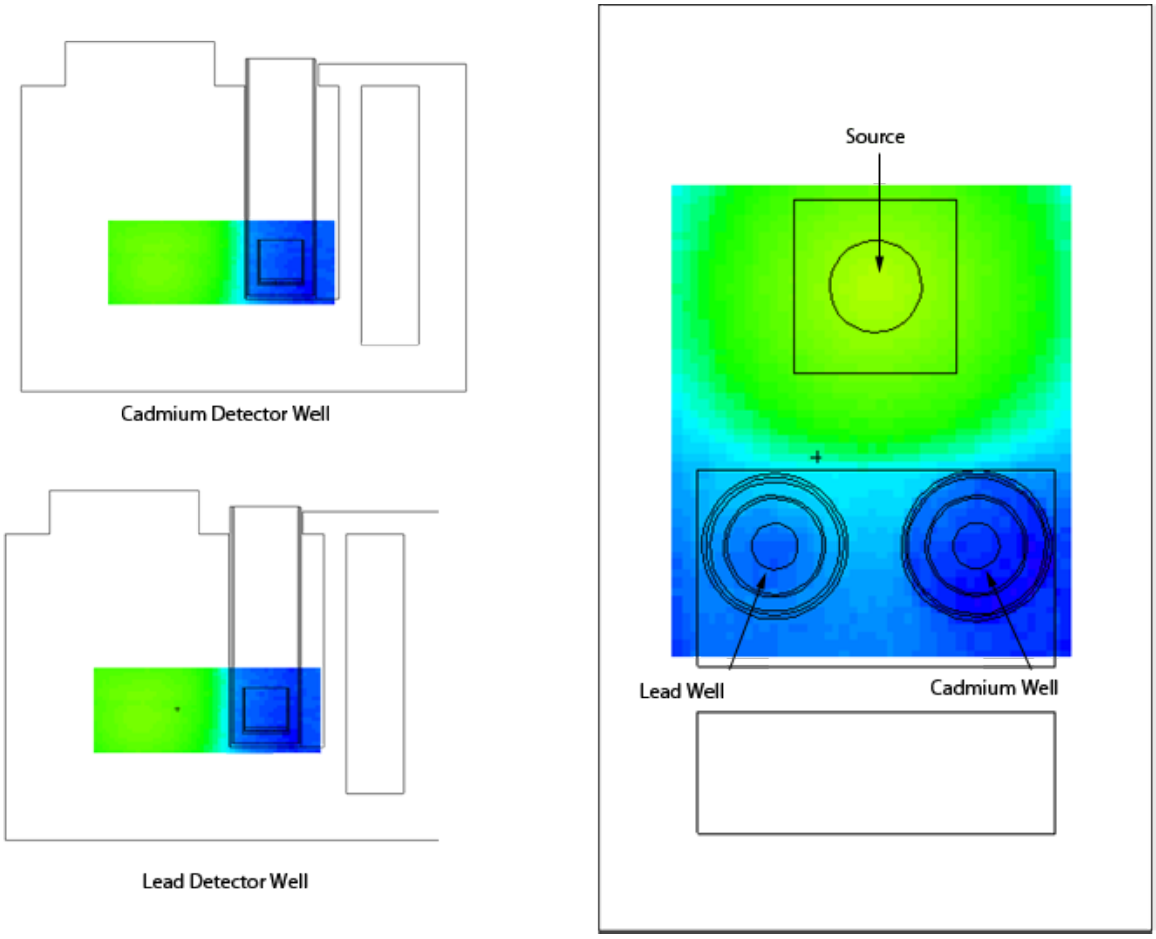

Figure D.3: Neutron Flux Profiles of the Lead and Cadmium Wells. Lighter colors correspond to a higher neutron population. The effect of the cadmium shielding is observed in the depression of the flux in the lower right by the cadmium well.

Table D.1: Simulated Neutron Solid Angle for Various Film Radii in the net spectra. The film radii are shown in seperate columns, with the thickness in rows. The thermal spectra (shown) is the subtraction of the lead and cadmium wells.

Thickness (cm)	1 cm	1.27 cm	1.905 cm	2 cm	2.5 cm	2.54 cm
0.0025	0.00055	0.00089	0.00204	0.00225	0.00351	0.00362
0.005	0.00055	0.00090	0.00204	0.00224	0.00350	0.00361
0.01	0.00055	0.00089	0.00204	0.00223	0.00348	0.00359
0.015	0.00055	0.00089	0.00202	0.00222	0.00346	0.00357
0.03	0.00056	0.00090	0.00201	0.00221	0.00341	0.00353
0.1	0.00058	0.00093	0.00202	0.00220	0.00334	0.00347
0.2	0.00063	0.00099	0.00208	0.00225	0.00338	0.00349
0.5	0.00080	0.00119	0.00234	0.00251	0.00365	0.00375
1	0.00109	0.00159	0.00286	0.00306	0.00427	0.00437
2	0.00170	0.00233	0.00389	0.00412	0.00544	0.00555

D.2.2 Gamma Intrinsic Efficiency

The gamma irridiator consists of a 97 µCi ^{60}Co (January 1st, 2012) inside of a steel pipe encased in lead bricks. The gamma intrinsic efficiency is calculated by simulating the fraction of solid angle the detector subtends and then using radioactive decay to model the ^{60}Co source. The ^{60}Co source strength is calculated according to (D.13). As there are two photons emitted from each $^{60}60$ decay, in order to normalize the MCNPX source strength it is necessary to multiply the single photon activity by two. Tabulated solid angle fractions are in Table D.2, and once again interpolation can be used for geometries not enumerated. These values were extracted from an MCNPX simulation using an F1 tally as described above.

$$\begin{aligned} S &= S_0 e^{-\frac{\ln 2}{t_{1/2}} t} \\ &= 97\,\mu\text{Ci}^{60}\text{Co}\ \frac{3.7\times10^{10}\,\text{decay/s}}{\text{Ci}}\ \frac{2\text{photon}}{decay}\ e^{-\frac{\ln 2}{5.27\,\text{year}} t} \\ &= 7.178\times10^{6}\,\text{photon/s}\ e^{-\frac{\ln 2}{5.27\,\text{year}} t} \end{aligned} \tag{D.13}$$

It should be noted that the gamma irradiator detector well is encased in a 1/2 inch steel pipe which is surrounded by lead, providing a beam like geometry while also

Table D.2: Simulated Gamma Solid Angle for Various Film Radii

Thickness (cm)	1 cm	1.27 cm	1.905 cm	2 cm	2.5 cm	2.54 cm
0.0025	0.0060	0.0095	0.0206	0.0226	0.0347	0.0357
0.005	0.0060	0.0095	0.0206	0.0226	0.0347	0.0357
0.01	0.0060	0.0095	0.0206	0.0226	0.0347	0.0357
0.015	0.0060	0.0095	0.0206	0.0226	0.0347	0.0357
0.03	0.0060	0.0095	0.0206	0.0227	0.0347	0.0357
0.1	0.0060	0.0096	0.0207	0.0227	0.0348	0.0358
0.2	0.0061	0.0097	0.0209	0.0229	0.0349	0.0360
0.5	0.0063	0.0099	0.0212	0.0232	0.0353	0.0364
1	0.0066	0.0103	0.0217	0.0237	0.0359	0.0379
2	0.0071	0.0109	0.0225	0.0247	0.0371	0.0382
3	0.0075	0.0114	0.0233	0.0255	0.0381	0.0392
4	0.0079	0.0119	0.0240	0.0262	0.0390	0.0401

introducing lower energy photons. The contribution of these lower energy photons is shown in Figure D.4, and it is evident that these contributions are a magnitude less than the contributions from the primary photons of the ^{60}Co decay. Table D.2 considers the contributions from all sides, but it is evident that the contributions from the side scattering is not large as 100 times increase in the thickness (50 µm to 5 mm) results in only a 4% increase in the number of particles crossing the detector.

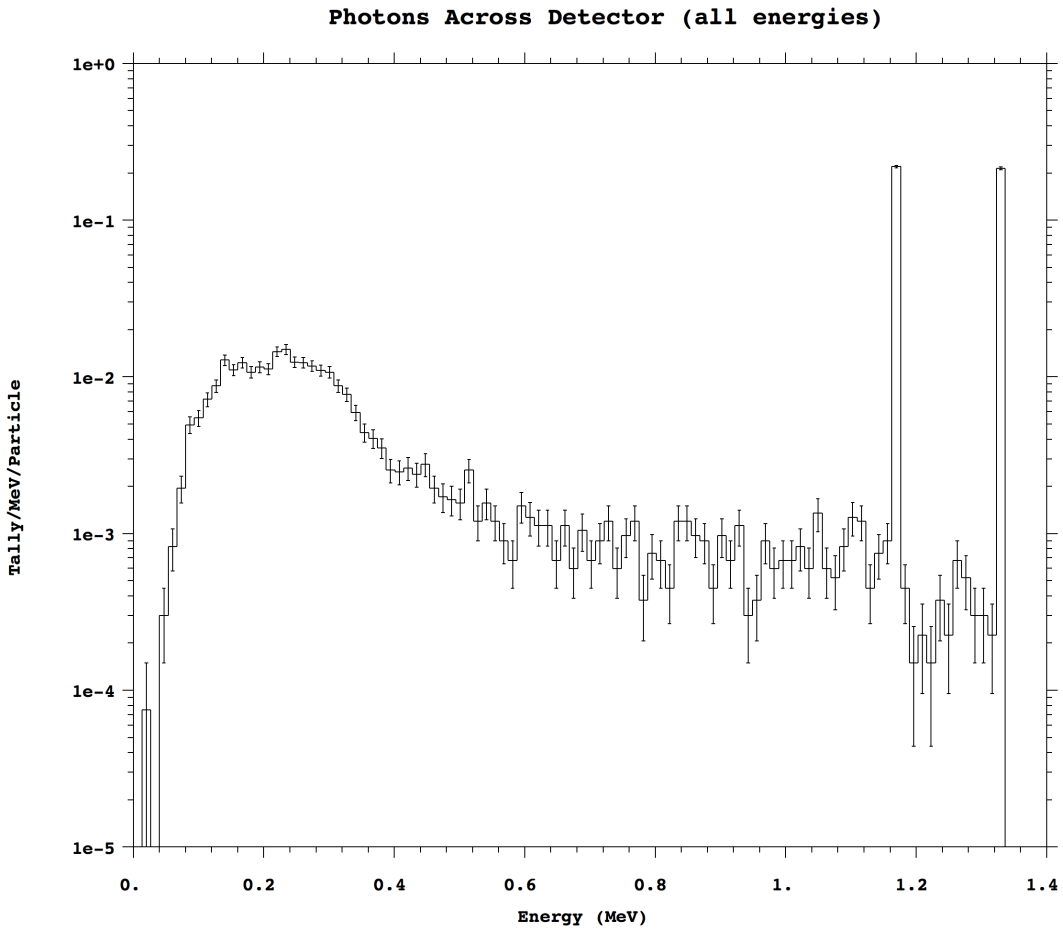

Figure D.4: Photons incident upon a detector from an ^{60}Co source. The two ^{60}Co photons (1.17 MeV and 1.33 MeV) make up the majority of the incident photons.

Appendix E

Measured Polymeric Film Detectors

E.1 Introduction

The potential application of a material for use in a Radiation Portal Monitor (RPM) can be evaluated by measurements of the detector's sensitivity to gammas and the detector's response to neutrons. A detector material might be a possible replacement if the there exists a neutron response that can be differentiated from photons for given sensitivity of gammas, namely 1×10^{-6}. A simple way to discriminate between gammas and neutrons is to use a pulse height discriminator, above which the detector detector will only record one photon out a million as a neutron. Under this framework it is then possible to develop a mathematical lower level discriminator (MLLD) of the pulse height spectrum to function as this pulse height discriminator, and to then formulate the sensitivity requirement as the gamma intrinsic efficiency as a function of MLLD. Six detectors (three boron loaded plastic scintillators, one LiF:ZnS(Ag) doped screen, GS20, a post processed composite PEN film, and a polystyrene) were then evaluated for their ability to perform in a RPM. The thickness of these detectors and mass of the absorber are shown in Table E.1.

Table E.1: Physical characteristics of the detector.

	Absorber	Thickness	Mass Absorber (mg)
EJ 254 2.5%	^{10}B	1/4"	59.5
EJ 254 1%	^{10}B	1/4"	23.8
EJ 254 5%	^{10}B	3/4	356.1
EJ 425 HD2-PE	^{6}Li	0.1 mm	17.5
GS20	^{6}LI	2 mm	155
Annealed PEN	^{6}Li	$\approx$ 212 µm	42.42
PS Film	^{6}Li	50 µm	2.71

E.2 Methods

The neutron performance was determined by the ^{252}Cf irridiator previously described, and the gamma source was the ^{60}Co irridiator. Due to the wide range of light output of these films it was necessary to use a two voltages (1000 V and 1180 V) in order to capture the entire spectra on an ADC with a zero to 10 V range with repeatable resolution. However, a measurement of the GS20 peak in the lead well was always recorded which then allowed the spectra to be tied together based on this feature, as shown in Equation E.1.

$$\text{Feature at Setting A} = \frac{\text{GS20 Peak at Setting A}}{\text{GS20 Peak at Setting B}} \text{ (Feature at Setting B)} \quad \text{(E.1)}$$

The count rates are not scaled for gain and voltage settings as they should remain constant as long as counts are not pushed below the lower level discriminator or cause roll-off.

E.2.1 Neutron Performance above Gamma Discriminator

An accurate measure of the neutron performance above the pulse height discriminator is essential for the comparison between detector materials. In Figure E.1 it is shown that the location of the MLLD is a pretty stable measurement for PS films of a different thickness. However, in previous work which focused on using the fraction of

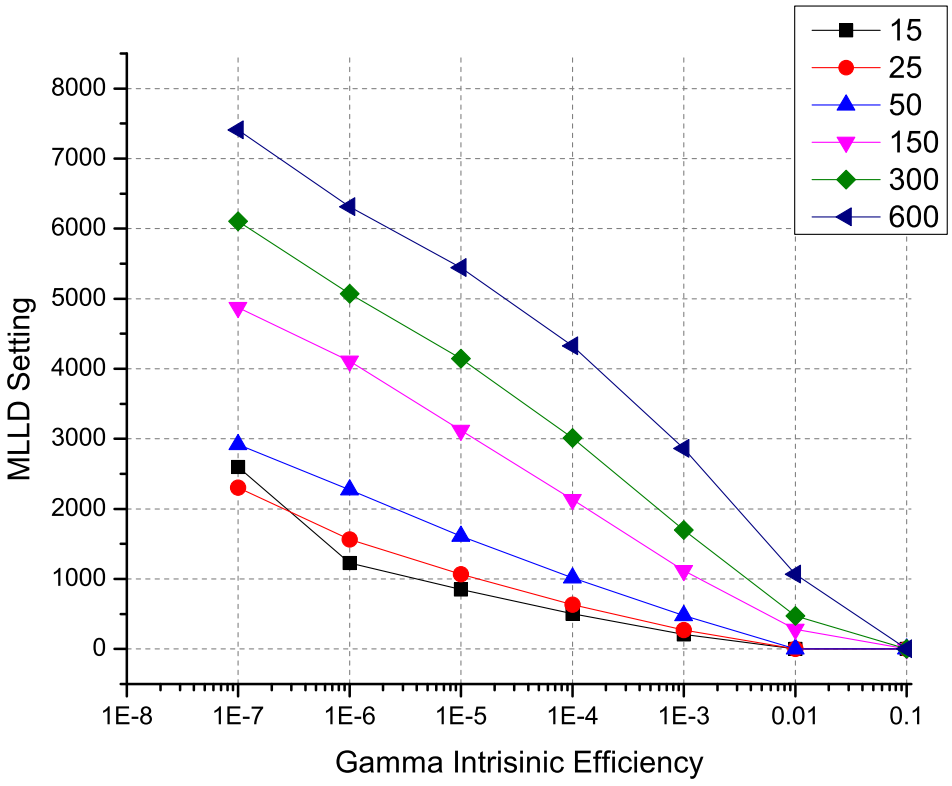

Figure E.1: The mathematical lower level discriminator (MLLD) as a function of intrinsic effigies for 10% PS films of various thickness. The linear nature suggest that the determination of the MLLD is repeatable.

neutron counts above the MLLD it was observed that the fraction (as it is normalized by the entire count rate) is very susceptible to sample to sample variations in the low energy channels. Therefore, after extensive studies using the polystyrene matrix a more stable measure was found by simply integrating the counts in the neutron spectra above the MLLD and then normalizing by the mass of neutron absorber in the samples (Equation E.2). While this method does not have the errors associated with summing over the low channels, it does require an accurate measure of the mass of ^{6}Li in the sample. Alternative methods would also probably be stable, but they are not discussed here.

$$\eta = \frac{\int_{\text{MLLD}}^{\infty} p(x)dx}{\text{Neutron Absorber Mass}} \tag{E.2}$$

E.3 Results

The following figures, Figure E.2 and Figure E.3, show the measured spectra of the detectors for neutrons and gammas. It is clear that the EJ-254 (boron loaded plastic) detectors will have poor performance because of their large gamma response. The EJ-426 (LiF:ZnS(Ag)) has the lowest response, and it is not clear if the tail of the spectra is due to actual counts or background. In the neutron spectra it was decided to only plot the performance of the best EJ-254 (though Figure E.9 display the performance of all EJ-254 films). It is observed that the LiF:ZnS(Ag) is much brighter than the other films, and it is noted that the post processed composite PEN has a higher light output than the commercial EJ-254 (based on the peak location). The average channel number of the neutron and gamma spectra of each detector was calculated and are presented in Table E.2. The average was computed for the neutrons in the thermal well to avoid the low energy channels from shifting the spectra away from any peak location. It should be noted that for EJ-254 the low channel number average is correct; this feature was identified as the neutron peak. Eljen publishes the light yield for the 1% boron as 9,200 photons per MeVee, 8,600 photons per MeVee

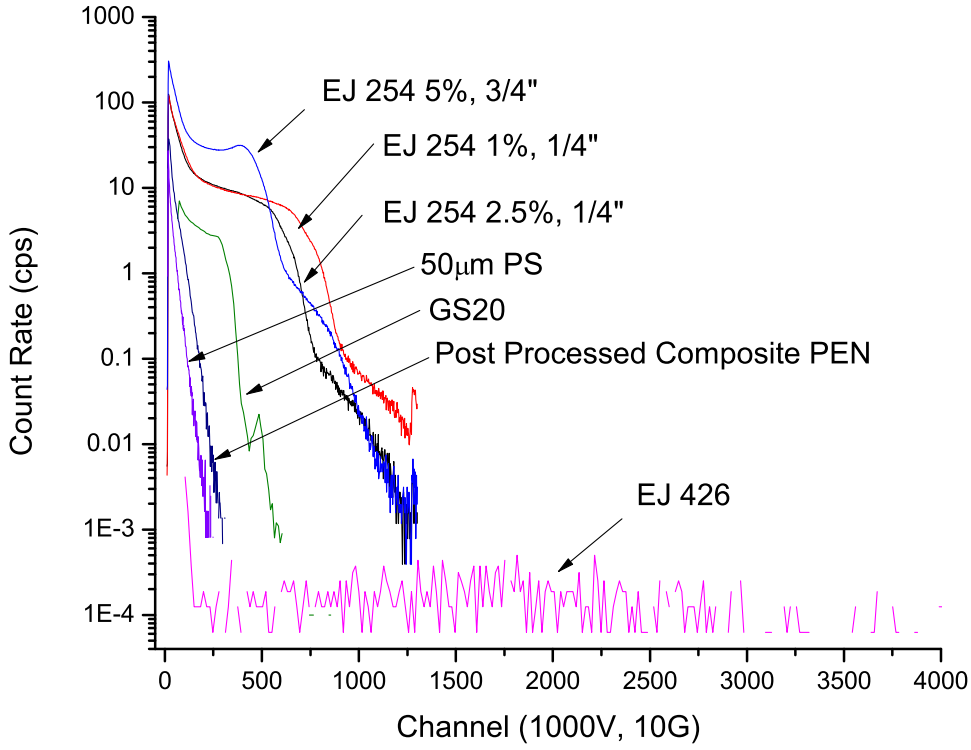

Figure E.2: Gamma Response from ^{60}Co source of measured detectors.

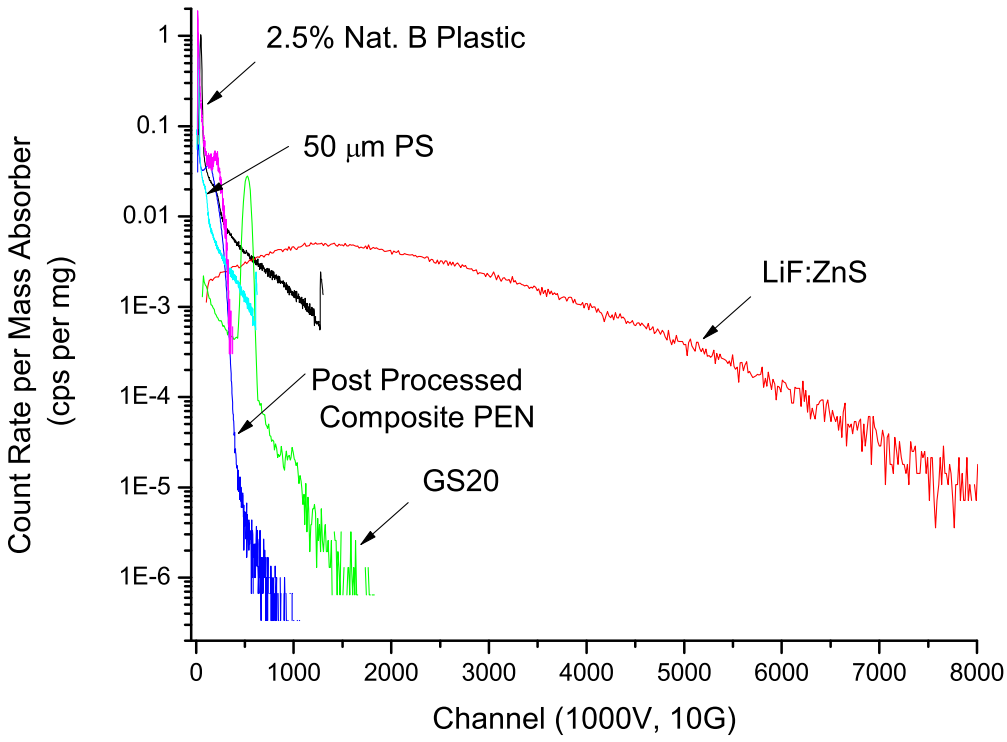

Figure E.3: Neutron Response (lead well) of the measured detectors. The count rate has been normalized by the mass of neutron absorber in the detector.

Table E.2: Average channel number of gamma and the thermal neutron spectra. The channel averages are scaled to 1,000V, 10G. The light yields are scaled to GS20 having 3,800 photons per MeV, and 6,250 photons per Neutron.

	Gamma		Neutron	
	Average Channel	Photons per MeVee	Average Channel	Photons per Neutron
EJ 254 2.5%, 1/4"	183.41	8,100	54.06	640
EJ 254 1%, 1/4"	216.25	9,500	65.04	780
EJ 254 5%, 3/4"	176.49	7,800	39.56	479
EJ 426 HD2	1636.53	72,000	2018.	24,000
GS20	172.76	3,800	524.10	6,250
Annealed PEN	41.11	1,800	142.01	1,700
PS Film	32.18	1,400	169.34	2,000

for the 2.5% boron, and 7,500 photons per MeVee for the 5% boron, and Table E.2 shows agreement to these values. C.W.E van Eijk has published the light yield of LiF:ZnS as 75,000 photons per MeVee, which is close to our measured value of 72,000 photons per MeVee. The count rates of the detectors are presented in Table E.3 for both the thermal component as well as only in the lead well spectra. Table E.4 shows the discrimination performance of the tested detectors, while Figure E.4 plots the intrinsic efficiency (sensitivity) along with the neutron count rate, normalized by the absorber mass. Figure E.5 demonstrates the performance of two detectors fabricated at UT (the PEN by Rohit Uppal and the PS by Andrew Mabe).

E.3.1 Individual Detector Performance

The performance of the individual detectors are shown in the separate figures to clearly illustrate important features. It is apparent that the EJ-254 is not a suitable candidate for replacement detector material in an RPM using a pulse height discriminator. The reasons for this are twofold: 1) the detector is very thick which increases the probability of a gamma interaction as well as the probability that the interaction will deposit a majority of its energy and 2) ^{10}B has a much lower Q-value (2.78 MeV compared to 4.78 MeV) and a large pulse height deficit. However, the

Table E.3: Count rate of the detectors in the thermal spectra as well as the lead well spectra. The final two columns are normalize by the mass of the absorber in the material. Significant self-shielding may exists in the the 5% boron, 3/4" EJ-254.

	Count Rate (cps)		Count Rate per Mass Absorber (cps per mg)	
	Thermal Neutrons	Lead Well	Thermal Neutrons	Lead Well
EJ 254 2.5%, 1/4"	1104	1869	18.5	31.4
EJ 254 1%, 1/4"	447	1130	18.8	47.5
EJ 254 5%, 3/4"	1417	3415	3.98	9.59
EJ 42 6 HD2 0.1 mm	224	234	12.8	13.4
GS20 2 mm	328	412	2.12	2.66
Annealed PEN	322	227	5.35	7.60
PS, 50 µm, 10% LiF	90.6	20.7	7.63	33.4

Table E.4: Discriminator setting and count rate above the gamma intrinsic efficiency of 1×10^{-6} for various detectors.

	MLLD Location	Count Rate above the intrinsic discriminator setting of 1×10^{-6} per Absorber Mass (cps per mg)
EJ 254, 2.5% B, 1/4"	1280	0.20
EJ 254, 1% B, 1/4"	1300	0.05
EJ 254, 5% B, 3/4"	1290	0.03
EJ 426 HD2, 0.1 mm	3308	1.97
GS20, 2 mm	557	0.56
Annealed PEN,212 µm, 25% LiF	284	0.73
PS, 50 µm, 10% LiF	223	2.15

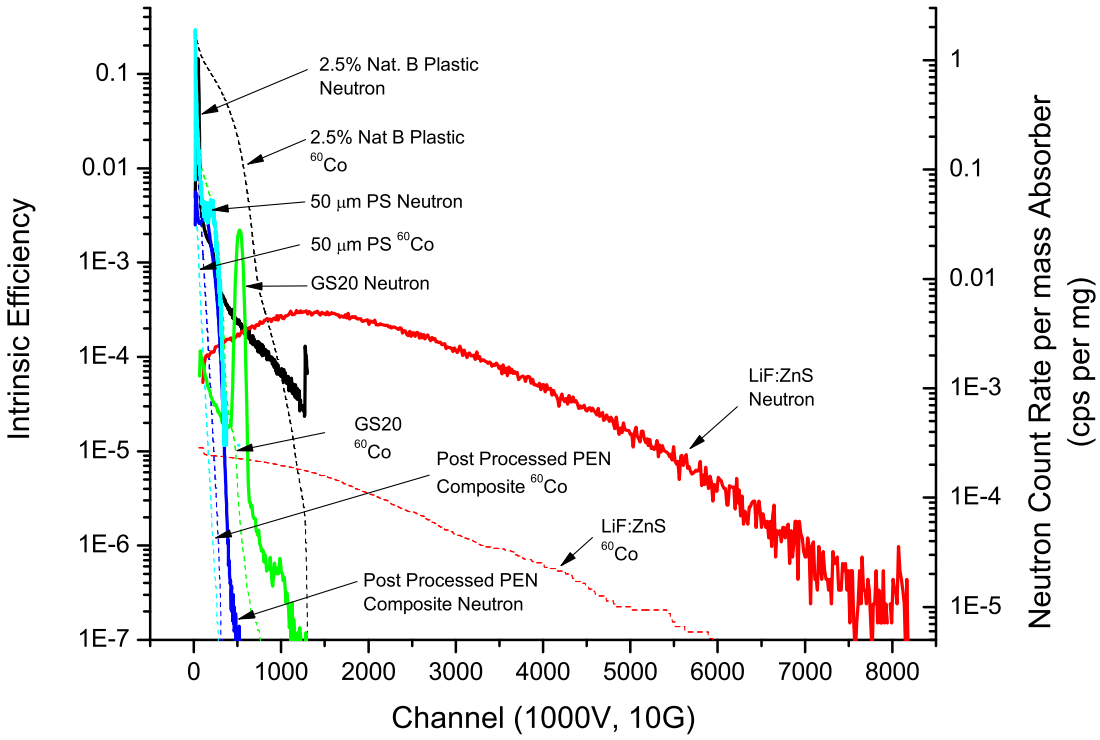

Figure E.4: Gamma sensitivity (left axis, dashed lines) and neutron performance (right axis, solid lines) of measured detectors. The neutron count rate above the gamma pulse height discriminator may be found by noting where the intrinsic efficiency crosses 1×10^{-6} and then integrating the neutron spectra above it. The neutron spectra are from the lead well, and are normalized by the mass of absorber.

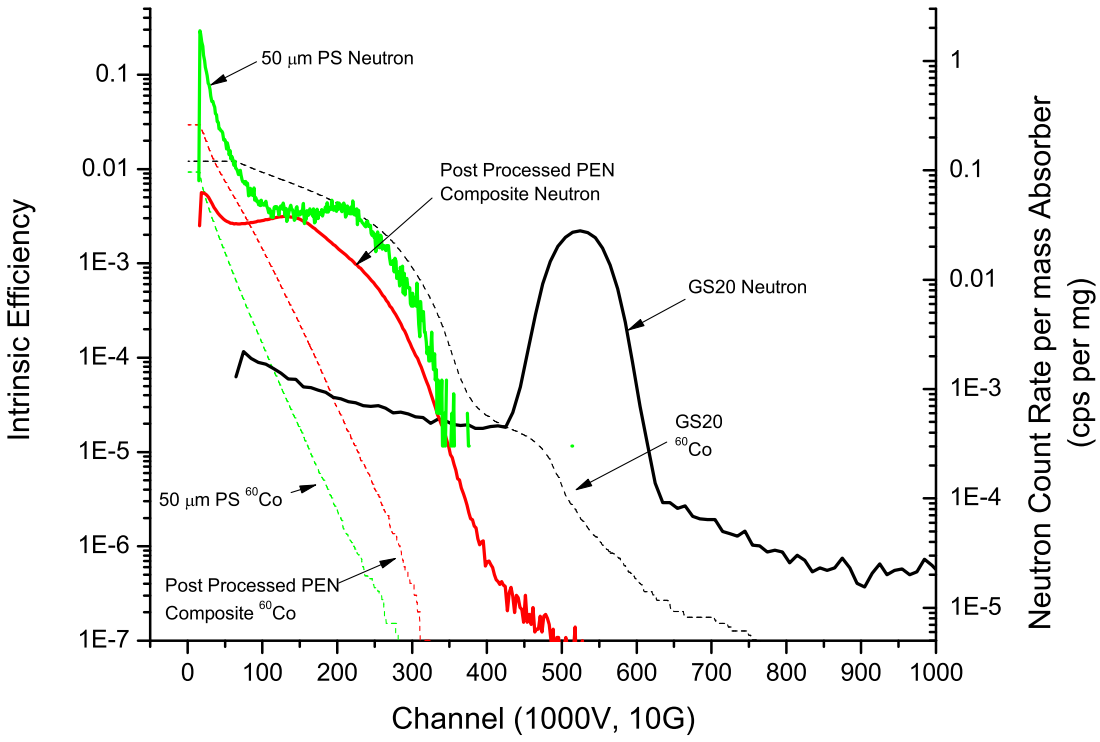

Figure E.5: Performance of a polystyrene and PEN film fabricated at UT compared to GS20.

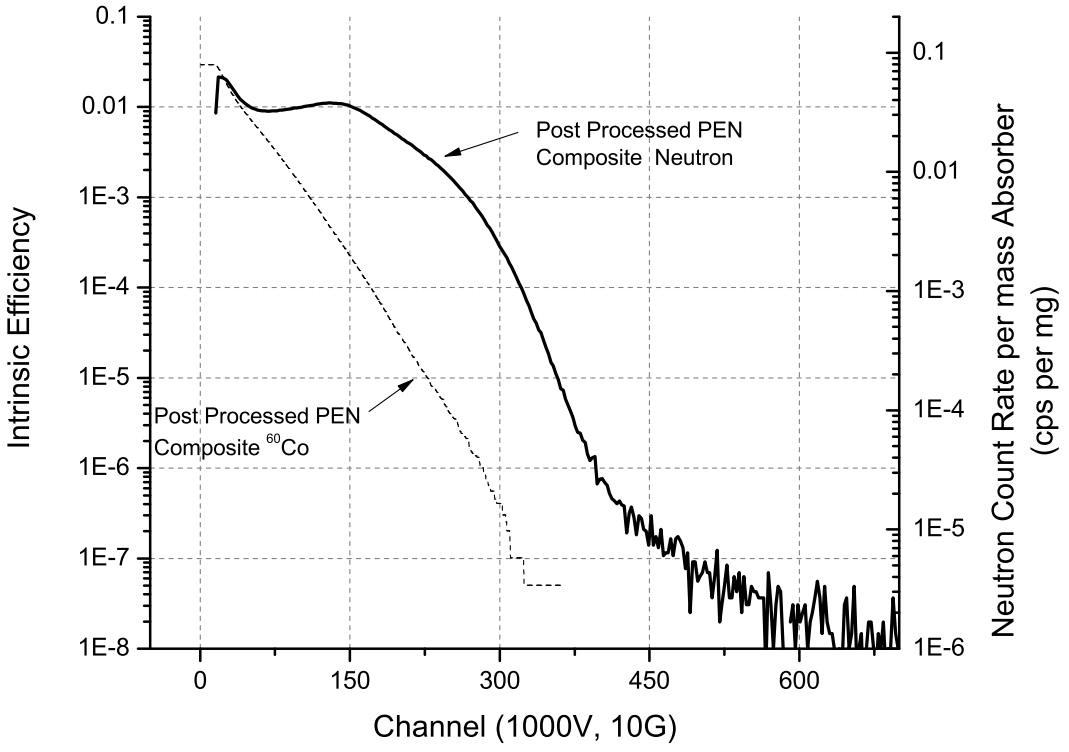

Figure E.6: Performance of an Post processed Composite PEN Film (22 March Sample).

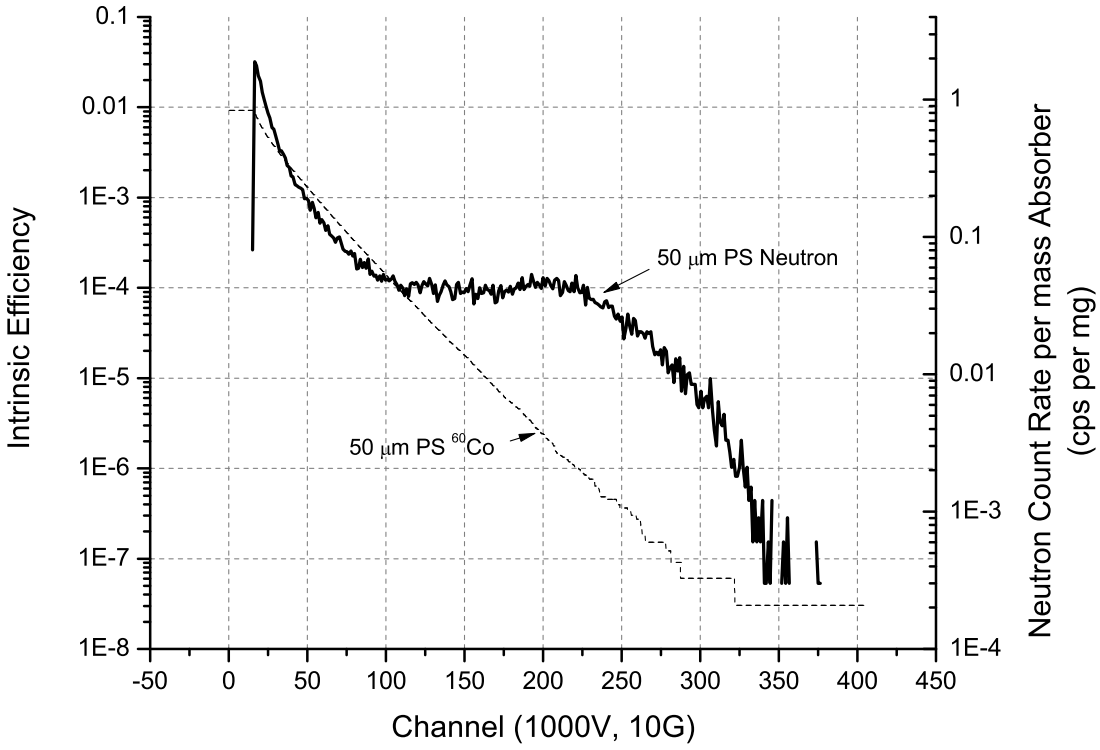

Figure E.7: Performance of an 50 µm, 10% ^{6}LiF PS Film (24 Jan 2012 Sample).

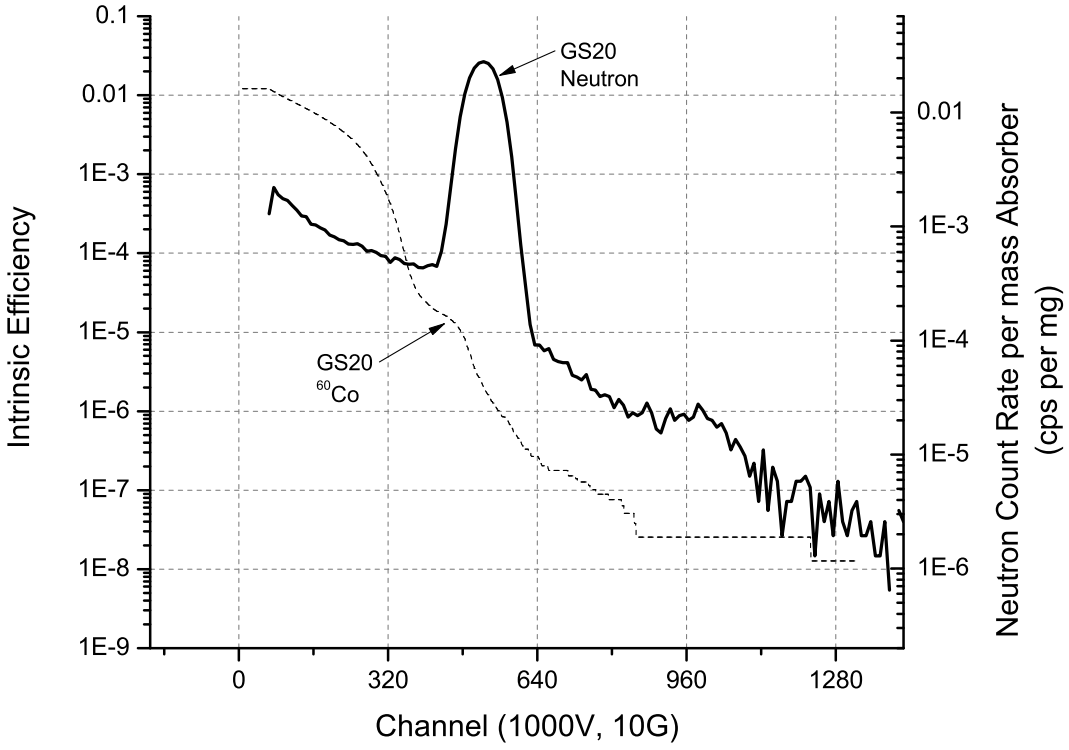

Figure E.8: Performance of 2 mm GS20. It should be noted that there is significant self shielding in GS20, and that due to the gamma sensitivity catching the tail of the neutron peak the count rate above the gamma pulse height discriminator has the most variation of the samples measured.

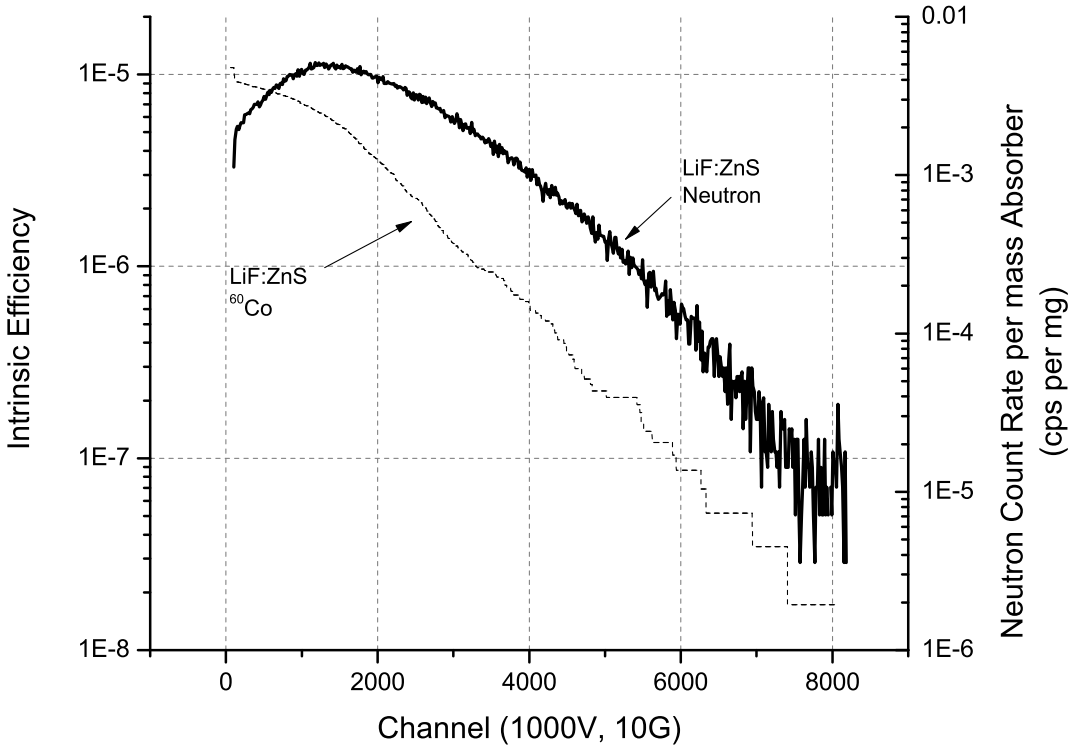

Figure E.9: Performance of EJ-426 HD2 (LiF:ZnS(Ag)) sheet. This is the brightest scintillator tested, with the lowest gamma sensitivity.

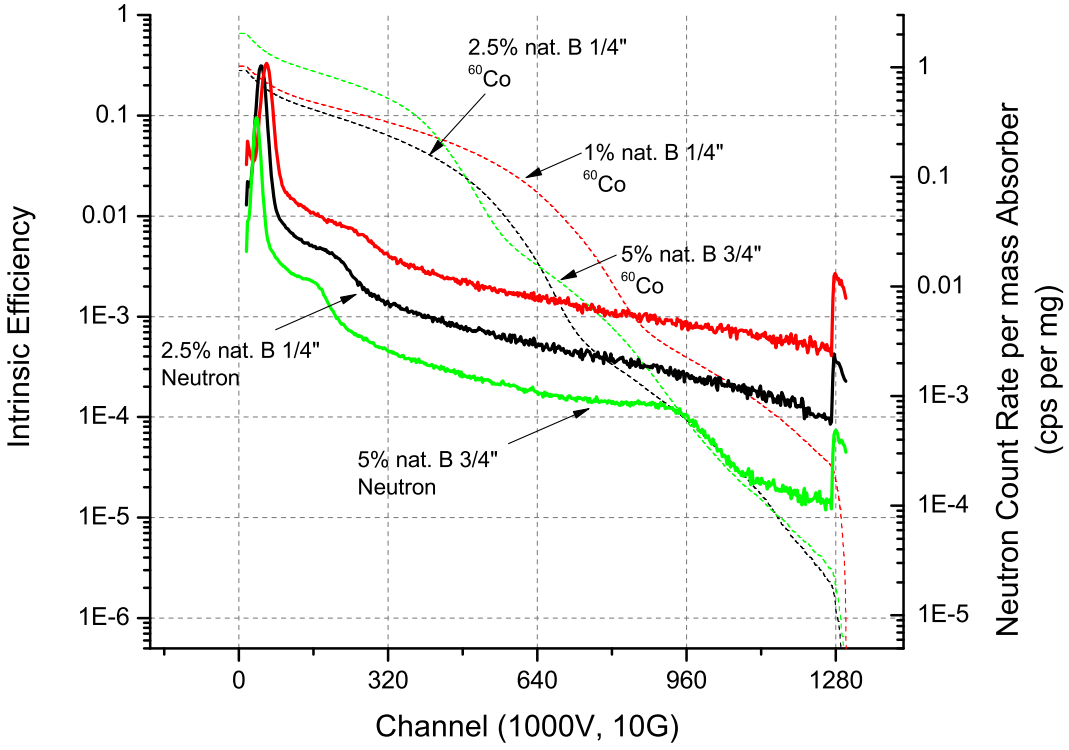

Figure E.10: Performance of EJ-254

material is optically transparent and due to ^{10}B's large thermal perhaps a thin sheet of EJ-254 might make a suitable detector material.

Appendix F

Simulation Code Base

The simulations used in this thesis available on Github. The GEANT4 Detector Simulations are separated from the Genetic Algorithm Simulations. To obtain a copy of the code base simply clone the repositories with `git clone git://github.com/murffer/DetectorSim.git LocalProjectName`. What follows is a compilation of the README's for each project.

F.1 Birks Constant Simulation

Simulation of gammas and neutrons and the subsquent energy deposition, focusing on the effect that the Birks Constant has on the optical photon yield in EJ426, GS20 and PSLiF.

The variation of the Birks constant is not completed by setting the material property parameters, but rather by using a script to replace the value in the source code and then recompiling and running. While this is definately not the elegant solution to this problem, setting the Birks parameter through the use of a DetectorMessenger did not seem to change the value used in the simulation.

F.1.1 Geometry

The detector is a simple box, into which the reaction products are shot. Once an optical photon is generated it's tracked is tallied and the particle is killed.

Histograms and Analysis The analysis is completed through the GEANT4 analysis manager class, and set to use the ROOT output. There is a single histogram created:

- Number of optical photons created in detector

The number of optical photons created is found by counting the number of optical photons in the stacking action, and once counted the track is killed.

F.1.2 Build Instructions

Options exists to build this a single core application or for multiple processes with the GEANT4 MPI library. To build for a single core application:

```
cd BirksConstant/
mkdir build; cd build;
cmake ..
make
```

To build for a multicore application one needs to turn on the `USE_MPI` preprocessor defination as follows:

```
cd BirksConstant/
mkdir build; cd build
cmake .. -DUSE_MPI=ON
make
```

F.1.3 Run Instructions

If the user elected to build for the MPI libary then it is suggested to submit the job to the cluster through TOURQE/MAUI. However, it is suggested that if they are running the paramater checks to use a single node. A BASH script has been provided, `birksConstnat.sh` that can be run to vary the Birks constnat for the materials considered in the simulation. A python analysis script has also been provided, `analysis.py` to summerize the run output, saving the results to `results.csv`.

F.2 Layered Detector Calibration

Simulation of gammas and neutrons and the subsquent energy depsotion and optical photons of three layered detectors.

F.2.1 Geometry

The detector assembly is two thin films sandwhiched between three PMMA slices, mounted with optical grease. The entire assembly was wrapped with teflon and black tape. A fish tail light guide was used to collect the light. The detector assembly is constructed by placing a number of volumes inside of each other. The largest volume for the detector is the teflon cladding. Inside the telfon cladding volume is slightly smaller PMMA volume to represent the arcylic. Placed inside the PMMA volume are the detector slices. The detector slices are actually slices of optical grease, which have the neutron absorbing detector inside of them.

F.2.2 Histograms and Analysis

The analysis is completed through the GEANT4 analysis manager class, and set to use the ROOT output. There are two histograms created: + Number of optical photons created in detector + Number of optical photons detected at PMT

The number of optical photons detected in the PMT is found using a sensitive detector in the PMT, and the number of optical photons created is found by counting the number of optical photons in the stacking action.

If the user elected to build for the MPI library the following command may be used for combining the seperate ROOT files `hadd GS20_Neutron.root GS20_Neutron_*.root`

F.2.3 Build Instructions

Options exists to build this a single core application or for multiple processes with the GEANT4 MPI library. To build for a single core application:

```
cd LayeredDetectorCalibration/
mkdir build; cd build;
cmake ..
make
```

To build for a multicore application one needs to turn on the `USE_MPI` preprocessor defination as follows:

```
cd LayeredDetectorCalibration/
mkdir build; cd build
cmake .. -DUSE_MPI=ON
make
```

F.2.4 Run Instructions

If the user elected to build for the MPI libary then it is suggested to submit the job to the cluster through TOURQE/MAUI.

F.3 Light Validation

Validation of the light transport simulations and the quantities that are used in the models.

Projects:

- BirksConstantEffect - Examining the effects of the Birks coefficient on materials and the light yields
- GS20Calibration - A simulation of GS20 as measured (except using a neutron and gamma gun sources) and the number of optical photons detected and measured
- PSCalibration - A simulation of PS as measured (except using a neutron and gamma gun sources) and the number of optical photons detected and measured
- LayeredDetectorCalibration - A simulation of a 4" by 6" slab detector that was fabricated and measured at UTK. This simulation validates the number of optical photons detected and measured.

F.4 Scintillation Slab With WLS and Cladding

Simulation of optical photon collection in a scintillation bar that is wrapped in a wavelength shifting plastic and encased in an optical cladding.

F.4.1 GEOMETRY:

The geometry is a thin 100 um slab that is 30 cm wide by 200 cm long. There are two rectangular PMT's attached to either end of the bar. The bar is encased in a plastic that can be set to a wavelength shifter. The entire assembly is wrapped in an optical covering (tape, mylar, air).

F.5 EnergyDeposition

Simulation of the energy deposition in a thin film.

F.5.1 Geometry

The geometry of this simulation is a cylindrical detector mounted on a thin PMMA base. The source is a beam of particles shot perpendicular into the detector. Various materials are available for use for the simulation, including polystyrene and methyltyrene of various loadings. It should be notated that the loadings of the films could be improved to use a method that takes in the percent loading and either the chemical formula or compound name and calculates the materials from there.

F.5.2 Run Macros

Two run macros are included in this for the simulation of neutrons and gammas. They are: + macros/nRun.mac + macros/gRun.mac The other two macros (`macros/neutronSource.mac` and `macros/gammaSource.mac`) are utility scripts that setup the Co-60 source or a 0.025 eV neutron beam source.

F.5.3 Compile and building

This project is setup to use the CMAKE tools as described previously. In addition, `subJobs.sh` can be used to submit jobs to the cluster. These jobs are not paralleled.

F.5.4 Analysis and Histograms

The output of this simulation is a ROOT file that contains two histograms (when the histograms are activated). The first, `eDep`, is the total energy deposited in the event. The second, `posEDep`, is a 2D histogram of the position of first interaction and the corresponding total energy deposition. An analysis script, `analysis.py` has been

written in python to assist in the summarizing and plotting of this histograms. It may be desirable to pipe the output of the python script directly into a file an allow the ROOT messages to print to the screen; this can be accomplished with `python analysis.py > output.csv`

F.6 Light Yield and Energy Deposition

Simulates the effect of the film thickness (energy deposition) on the light yield.

There are two macros provided, one for neutrons and the other for gammas. Both can be run with the script `subJobs.sh`.

In general it is observed that the light yield increases proportionally to the energy deposition. The script `analysis.py` grabs the mean of both the energy deposition and light yield histograms for each film thickness, while the root script `ExportHistos.C` exports selected histograms of interest to a CSV.

F.7 GS20 Calibration

Simulation of gammas and neutrons and the subsquent energy depsotion and optical photons in GS20.

Naming Conventions: Abosrber - the GS20 Scintillator PMT - the pmt

The seperate histograms can be combined with the following command. `hadd GS20_Neutron.root GS20_Neutron_*.root`

F.8 Range Simulation

Simulation of ranges of alpha, tritons, electrons and photons.

F.8.1 Geometry

The geometry is a box representing a 'semi infinite' homogeneous medium. The default geometry is constructed in DetectorConstruction class, but all of the above parameters can be changed interactively via the commands defined in the DetectorMessenger class.

F.8.2 Physics List

The physics lists are from the the G4 kernel, with specialized cuts. The options of the physics list are: - "emstandard_opt0" recommended standard EM physics for LHC - "emstandard_opt1" best CPU performance standard physics for LHC - "emstandard_opt2"

- "emstandard_opt3" best current advanced EM options.

PhysicsList contains also G4Decay and G4RadioactiveDecay processes

Physics lists and options can be (re)set with UI commands. A few commands have been added to PhysicsList, in order to set the production threshold for secondaries for gamma and e-/e+.

F.8.3 Run / Compiling

The code is setup to use the CMakeEnviroment distributed with GEANT4. Execution of `rangeSim` in 'batch' mode from macro files with the following command:

```
rangeSim   runs.mac
```

The interactive mode of `rangeSim` with with visualization can be run with:

```
% rangeSim
...
Idle> type your commands
....
Idle> exit
```

Five run macros have been provided to simulate the ranges of various particles of interest. They are: + eRangeDist.mac - the distribution of an electron in polystyrene + erange.mac - the range of different energy electrons in polystyrene + gammaRange.mac - the range of gammas in polystyrene + rxnProductRange.mac - the range of the reaction products of pertinent neutron interactions

F.8.4 Histograms and Analysis

rangeSim produces several histograms which are saved as rangeSim.root by default. Content of these histograms:

- track length of primary particle
- number of steps primary particle
- step size of primary particle
- total energy deposit
- energy of charged secondaries at creation
- energy of neutral secondaries at creation

The histograms are managed by G4AnalysisManager class and its Messenger. The histograms can be individually activated with the command:

`/analysis/h1/set id nbBins valMin valMax unit`

where unit is the desired unit for the histograms (MeV or keV, deg or mrad, etc..)

One can control the name of the histograms file with the command:

`/analysis/setFileName name` (default rangeSim)

It is also possible to print selected histograms on an ascii file:

`/analysis/h1/setAscii id`

All selected histograms will be written on a file name.ascii (default rangeSim)

A utility file, `Range.C` has been written to plot the charged particle creation energies for the alpha, triton, and Co60 runs. This can be loaded into the root enviroment with:

```
root[#] .L Range.C
root[#] main()
```

F.9 Light Quenching

Simulates the light quenching of scintillators using the GEANT4 toolkit. The geometry is currently a simple box volume, using a polystyrene based scintillator. The physic of the simulation include Optical Physics for the simulation of the light yield. The plastic scintillator proprieties are taken from the G4 simulation example in `examples/extended/optical/wls`. A PVT based scintillator is also provided, but without setting the `birks parameter` the quenching is not observable.

Several runs are provided for the user. They are:

- alphaRun.mac - Alpha from 10 keV to 2.15 MeV
- eRun.mac - Electrons from 10 keV to 2.15 MeV
- tritonRun.mac - Tritons from 10 keV to 2.15 MeV
- demoRun.mac - A representation of a gamma and neutron

In addition, for convince a script has been written, `jobSub.sh`, which allows for the submission of all of the runs to the cluster system.

The analysis is completed without the use of the Singleton analysis class. This might be recovered by using a previous commit. A root script is provided, `LightQuench.C` which may be invoked by root that compares distribution of number of photons created for the particles in demoRun.mac. This script also generates .csv files which can then be plotted in ones favorite package.

F.10 Electron Energy Deposition Simulation

Simulation of energy deposition of electrons in materials. The material is divided into logarithmic bins, and the energy deposited in a step is accumulated for an event, and all of the events in a run are accumulated for an average value and variance.

F.10.1 Geometry

The geometry is a box representing a 'semi infinite' homogeneous medium. The default geometry is constructed in DetectorConstruction class, but all of the above parameters can be changed interactively via the commands defined in the DetectorMessenger class.

F.10.2 Run / Compiling

The code is setup to use the CMakeEnviroment distributed with GEANT4.

- execute electronEDep in 'batch' mode from macro files % electronEDep eDep.mac
- execute electronEDep in 'interactive mode' with visualization % electronEDep .... Idle> type your commands .... Idle> exit

F.10.3 Histograms and Analysis

No histograms are produced in this simulation. Instead, the analysis of the simulation can be summarized into a csv with the provided python script, `analysis.py`.

F.11 GS20 Calibration

Simulation of gammas and neutrons and the subsquent energy depsotion and optical photons in GS20.

The Briks constant was set to be 0.025 mm/MeV. Naming Conventions: Abosrber - the GS20 Scintillator PMT - the pmt

The seperate histograms can be combined using the clean up script provided with the simulation `hadd GS20_Neutron.root GS20_Neutron_*.root`

F.12 DetectorSim

Simulation of Radiation Detectors with GEANT4 and MCNPX

F.12.1 Simulated Physics and Detectors

These simulations are intended to highlight basic physics of scintillators

- ParticleTracks - A demonstration of the track structure from different charged particles
- RangeSim - Simulates the range of various charged particles
- ElectronEnergyDeposition - Simulates the cumulative energy deposition for electrons in a material.
- EnergyDeposition - Simulates the energy deposition in a material. This was used primary to determine the fraction of energy deposited by the Co-60 and the thermal neutrons.

The following simulations are intended to explore more complex interactions of a detector.

- LightQuenching - Studies the light quenching in a simple scintillator
- LightYieldEDep - The light yield as a function of energy deposition and film thickness

F.12.2 Light Background

- ScintillationSlab - A single scintillation bar. The optical photons are collected on a single PMT
- WLSScintBar - A single scintillating bar sandwiched between two WLS shifting bars

F.12.3 Light Validation

Simulations for the light validation of different detector designs. The simulations included are:

- GS20Calibration
- PSCalibration
- LayeredDetectorValidation

F.12.4 MCNPX Models

The MCNPX models are a layered detector model in which planes of detector material are stacked atop each other and a wrapped cylinder model in which concentric cylinders of material are simulated. The layered detector models is primary intended for plotting the results of the optimal geometries found by the genetic algorithm simulations.

F.13 Tracking

Provides tracking of primary particle. Currently the defaults are an alpha (2.05 MeV), triton (2.78 MeV) and two electrons (10 keV and 100 keV). Currently this is only intended to demonstrate the different particle track structures, and thus no analysis is provided.

F.13.1 Compile Instructions

This program was built with CMAKE. It is assumed that the environment is setup such that the variable `G4INSTALL_CMAKE` is set to the installation files for GEANT4 for cmake. The code can be built by the following commands:

```
mkdir build; cd build; cmake .. make
```

The executable and run scripts will now be in the build directory. The compiled code can be run with:

```
./tracking ./tracking run1.mac
```

The first will bring up an interactive session, while the second will run the four charged particles in the run script.

F.14 PS Calibration

Simulation of gammas and neutrons and the subsquent energy depsotion and optical photons in PS.

The Briks constant was set to be 0.025 mm/MeV.

F.15 Simulation of RPM8 with MCNPX

Simulation of the RPM8 geometries with MCNPX. Two differnet types of models are considered, a layered detector design and a wrapped cylinder design. The layered detector design consits of planar layers of detector material. The wrapped cylinders is a central cylinder that has detector layers wrapped around it.

A utility file, `MCNPMaterial.py` is included to assit in the creation of various mixtures of LiF loaded PEN and PS. It is expected to be used primary for the `GetPSLiF` method and the `GetPENLiF` methods.

The TwoTubeData.txt is the results of the runs with two tubes of material, positioned at `cylinderPositions = ((4.23,10.16),(4.23,-10.16))`

In this simulation the dictionary for the geometry was:

```
geoParam={'RPM8Size':12.7,'DetectorThickness':0.01,'DetectorSpacing':0.4,
          'CylinderLightGuideRadius':0.5,'CylinderRadius':2.5}
```

The ThreeTubeData.txt is the results fo the runs having three tubes of material in the detector. The cylinders were placed at one-thrid of the way into the detector in the x cordinate (4.23 cm), and at the center of the y-axis with the other two tubes being placed equidistant in the moderator at 7.625 and -7.625 cm, as shown below.

`cylinderPositions = ((4.23,7.625),(4.23,0),(4.23,-7.625))`

The FourTubeData.csv is the results for having four tubes spaced equally in the RPM8 footprint, spaced equally. The cylinder positions are shown below.

`cylinderPositions = ((4.23,9.15),(4.23,3.05),(4.23,-3.05),(4.23,-9.15))`

F.15.1 Layered Detector

A brief script was written to analyaze create input decks for the plotting of the optinal goemetries, and for writing out the geometires. The geometries can be made into a form suitable for latex by the following comamnds:

```
cat TableOutput.txt | cut -d':' -f1 --complement | tr '[:blank:]' ' & ' > o
cat o | sed 's/$/\\\\/g'
```

F.16 GARPM8Opt

Optimization of an RPM utilizing Genetic Algorithms. The `master` branch is intended to contain the final, mostly completed files of this project. The `CrossSection` branch was an attempt to use MCNPX to generate the macroscopic cross sections which will then be composed with the flux to get an interaction rate. The `NEWT` branch was

following a suggestion to use NEWT to preform the deterministic transport and the cross section collapsing. `XSDRN` is a branch based on the SAS1 module of SCALE. This is the branch of development that seems most promising as of September 18th, 2013. The `GAProgressVis` branch was created to investigate differnet methods of visualizing the progress and output of the genatic algrothim.

F.16.1 Summerizing

The results of a simulation can be viewed with the python script `Summerize.py`. This script aggrogates all of the runs of a particular genome length and model (specified as input options) and ranks the geometeries according to their activity per mass or interaction rate per mass. It then outputs the ranked geometeries acitivies or interaction rate. Thre example usages of this script are provided below.

```
> python Summerize.py -o -x -g 10 -n 10 -m 3
> python Summerize.py -o -g 10 -n 10
> python Summerize.py -c -g 10 -n 10 -m 3
```

The first command summerizes a genome of length 10 simulated by the XSDRN model, returning the top 10 results with a minimium of 3 layers being detector slices. The second command summerizes a gonome of length 10 simulated with MCNPX, returning the top 10 count rates, ranked by the count rate per mass. The final command checks the XSDRN activity for the top 10 genomes of length 10 (with a miniumn number of 3 slices) using MCNPX.

F.16.2 Pertubations

Pertubations on a detector design were implemented in `MCNPXPertubations.py`.

F.16.3 GA Progress Visualizaiton

This branch of development, `GAProgressVis`, was created to investigate differnet methods of visualizing the progress and output of the genatic algrothim.

F.16.4 1D Deterministic Transport

1D deterministic transport provides a fast way to simulate many different geometries accurately. Currently, the SAS1 module in SCALE is being utilized to preform these calculations. The source spectra of the SCALE input deck was determined by running a MCNPX simulation of the Cf-252 source with an F1 current tally having the same energy bin structure as the neutron group used. The bound conditions are then the source on the left and the vacuum boundary condition on the right.

The intention of the bare calculation, `bare.mcnp`, is to provide a simulation without any neutron absorber (but with moderator) in order to determine the extents of the problem. Another simulation could be completed of the flux / current when the RPM is filled with the detector material.

XSDRNPM

XSDRN has the capability (using the activity calculation options) to calculate interaction rates. It is intended to greatly simplify the geometry by only including the moderator and detector materials. The material compositions will be simplified to only include H,Li-6,C,O and F.

NITAWL Input Options + `0$` All defaults + `1$` Integer parameters - I used all of the defaults, but set the number of materials I needed as 4. + `3*` Resonance self-shielding calculations are not desired, so this is not used. + `4*` No thermal kernel temperatures are desired + `6$` No MT's for Incoherent Matrices

Data Block 1

- `0$` Logical Assignments (left as defaults)

- `1$` General Problem Description. I think IZM and IM are the same, and MX = 2 (the detector and moderator are the only materials). I don't know what the correct value for MS is (maybe the number of isotopes in all of the materials). For the ISN I used 16 (order of the quadrature), and for the ISCT (order of scattering) I used 1, as these were both of the examples from the xsdrn.input deck.
- `2$` Editing and Special Options. Only setting the IFSN option to be greater than 0 because I am using a source
- `3$` Various Options. I am using IPM (for the boundary source) but I am not using cross-section weighting / collapsing
- `4$` Cross Section Weighting option - not using any cross sections
- `5$` Convergence Criteria - the width and thickness of the slab were entered

Data Block 2

- Mixing tables - `13$, 14$ 15*` The material compositions are entered in atomic densities, for which a calculation is shown on page 13 of the third lab notebook. For the detector a pseudo molecule is created which is designed to have a mass fraction equal to the specified composition.

Data Block 3

- Source Spectra (Data Block 3) - The source spectra number (IM)

Data Block 4

- Data Block 4 - this is for starting guesses for fluxes and fission densities

Data Block 5

- `35*` Interval boundaries (IM is the number of zones)
- `36$` Zone Number for each interval (the bit string geo, yo!)

- `39$` Mixture number by zone
- `49$` Material number for activities
- `50$` Process number for activities

Array	Keyword	Value	Explanation
1$	IZM	9	Number of zones (separate material regions)
1$	IM	9	Number of spatial intervals in problem
1$	MXX	2	Number of compositions in problem
1$	MS	6	Number of entries in mixing table
1$	IEVT	0	Fixed source calculation
2$	IFSN	1	No fission source, since IEVT = 0
3$	IPM	1	A singe boundary source entry in `32**`
3$	IAZ	1	The reaction rates by material zone for 1 zone
3$	IAI	1	Calculate reaction rate in each interval
5$	DY	200	Height of the slab
5$	DZ	30	Width of the slab
	IM		Number of zones?
	IGM	44	Number of energy groups (44)

Surface Source The surface source branch `XSDRNSurSrc` is trying to use a surface source. So far the idea is to use an isotropic surface source, in which the entries are simply a constant normalized by the cosine of the direction (F3.2.7)

A file short `xsdrn` input deck was written, `src.in`, to ascertain the correctness of the source spectra. This simulation used air as it primary medium, and was run

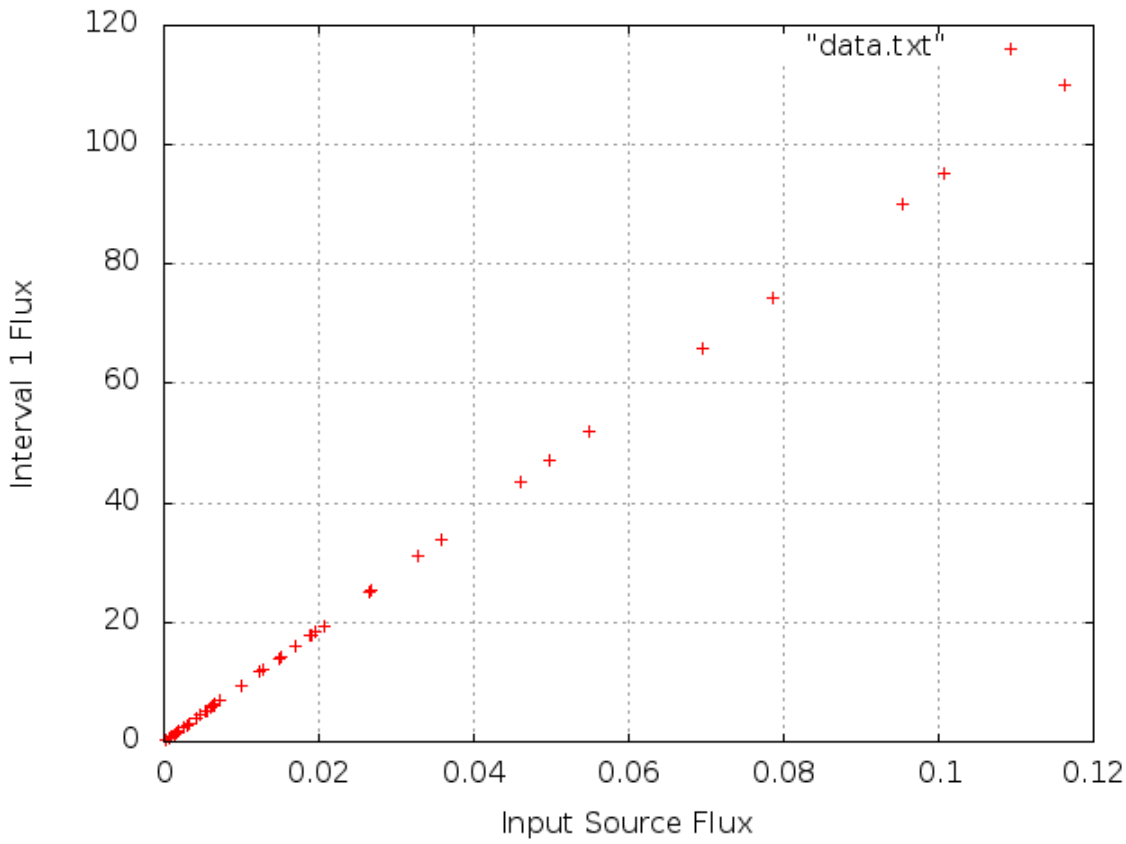

(in conjunction with `createSpectra.py`) for a quadrature of 4. The results of the simulation, shown below in which the input source flux is plotted against the calculated flux in the first interval shows a very linear trend, indicating that the data is source spectra is only off by a scaling factor.

The output of the XSDRN run was parsed by hand to have only contain the flux in the first group, this data was contained in `flux.dat`. The matrix of data in `flux.dat` was translated into a column vector, which was then pasted together with the initial source spectra. An outline of the commands used is below.

```
cat flux.dat | tr ' ' '\n' | grep -xv '' > dat
cut -d ' ' -f 3 SourceOut > col
paste col dat > data.txt
gnuplot
```

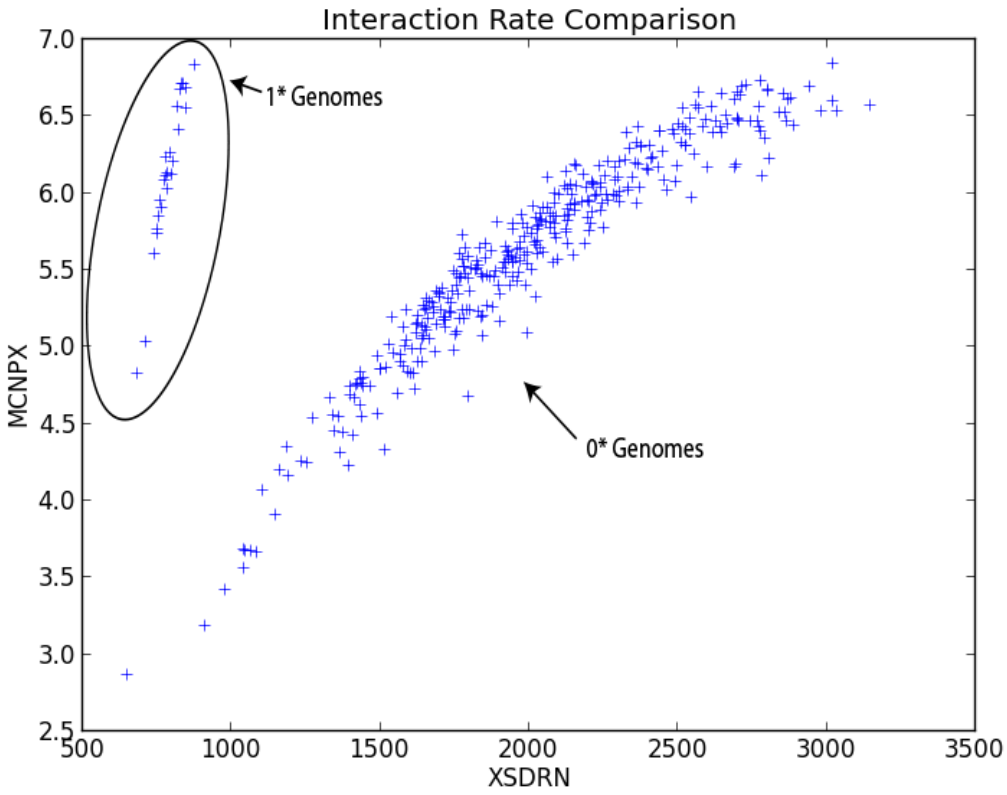

As this is probably due

XSDRMVal

Validation of the SAS1 based XSDRN transport calculations of the RPM8. The validation of the calculation will be preformed by simulating the same geometry in MCNPX, and comparing the results. A preliminary study on the data showed a distinct two group structure (pg. 16 of lab notebook). Upon further investigation it was observed that the two cluster could be roughly explained by the number of detector layers, and thus it was suspected that the calculation wasn't converged. After the convergence criteria was restricted a different two group structure was observed, as shown below. This structure was due to genomes simulated in XSDRN starting with 1 (a detector layer) having a much lower interaction rate than expected.

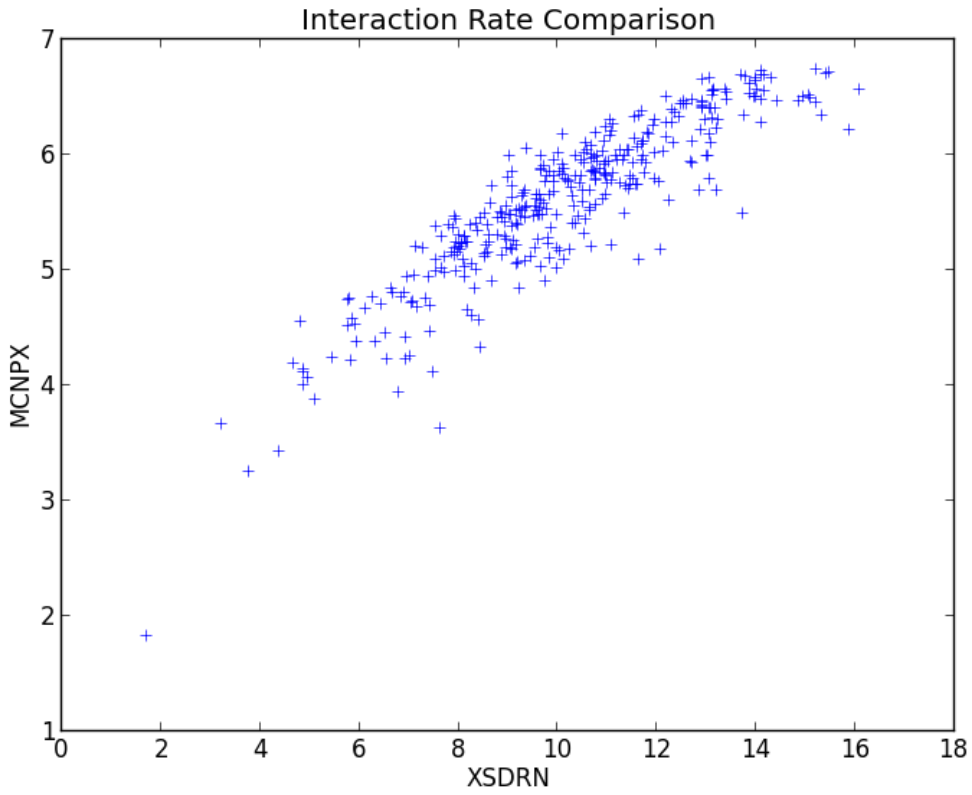

A linear fit was completed in the

to violating the boundary conditions with a strongly absorber layer and it has already been shown that it is sub-optimal to have a detector layer as the first layer this case was avoid.

MATLAB environment. A first order polynomial provided an R^2 value of 0.92, but did not go through the origin and thus wasn't the desired scaling factor. A fit (f(x) = ax) that did go through the origin provided a source strength of 6.1367, which was implemented in the XSDRN calculation.

Vita

Matthew J. Urffer was born January, 29, 1988 on a small turkey farm on Urffer Road in Coopersburg, Pa. He got his B.S. in physics from Carnegie Mellon University in Pittsburgh, PA. Upon graduation Matthew enrolled at the University of Tennessee, Knoxville where he received his Masters in Nuclear Engineering in December, 2012 and his doctorate in nuclear engineering in December, 2013.